



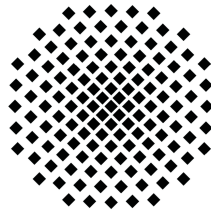
Max-Planck-Institut für Festkörperforschung
Stuttgart

Ultrafast Spectroscopy of Single Quantum Dots

Christian Wolpert

Dissertation an der
Universität Stuttgart

Juni 2012



Ultrafast Spectroscopy of Single Quantum Dots

Von der Fakultät Mathematik und Physik der Universität Stuttgart
zur Erlangung der Würde eines Doktors der
Naturwissenschaften (Dr. rer. nat.) genehmigte Abhandlung

vorgelegt von
Christian Wolpert
aus Würzburg

Hauptberichter: Prof. Dr. M. Lippitz
Mitberichter: Prof. Dr. P. Michler

Tag der Einreichung: 13. April 2012
Tag der mündlichen Prüfung: 25. Juni 2012

Physikalisches Institut der Universität Stuttgart
2012

Zusammenfassung

Die vorliegende Arbeit behandelt die kohärente Wechselwirkung zwischen einzelnen Halbleiterquantenpunkten und ultraschnellen optischen Pulsen. Unter gewissen Umständen können lokalisierte Exzitonübergänge in Quantenpunkten als semi-abgeschlossenes Zwei-Niveau-System angesehen werden. Während diese Beschreibung für das Erklären mancher Beobachtungen in kohärenten Experimenten ausreichend ist, so ist es doch manchmal erforderlich die Kopplung zwischen diskreten Quantenzuständen im Quantenpunkt und seiner Umgebung explizit zu berücksichtigen. Wir beginnen mit einfachen, klassischen Beispielen zur kohärenten Spektroskopie um uns darauf Experimenten zuzuwenden, bei denen die Wechselwirkung mit der Umgebung des Quantenpunktes ein wichtiger Faktor wird.

Zuerst wird eine neuartige Methode zur transienten differentiellen Reflektionsspektroskopie einzelner Quantensysteme eingeführt. Es handelt sich um eine reine Fernfeldtechnik welche keine ausgefallenen Probenbearbeitungsschritte benötigt und somit in einem breiten Bereich einsetzbar ist. Ein Anregepuls regt die Probe an und ein Abfragepuls liest die anregungsinduzierten Veränderungen im System nach einer variablen Verzögerungszeit aus. Im Falle eines einzelnen Dipoles ist das Signal durch das spektrale Interferogramm zwischen der vom Partikel zurückgestreuten Welle und dem Abfragelicht, welches an der Probenoberfläche reflektiert wird, gegeben. Diese Form der homodynen Detektion verstärkt die schwache, vom Partikel gestreute Welle und macht somit diese Art der Spektroskopie einzelner Quantenpunkte erst möglich.

Im weiteren Teil dieser Arbeit wird unsere Spektroskopiemethode entweder zur Charakterisierung der kohärenten Eigenschaften einzelner Quantenpunkte, zum Präparieren und Auslesen eines gewünschten Quantenzustandes oder zur gezielten Manipulation dieser Zustände angewandt. Kohärenzzeiten und Oszillatorstärken von lokalisierten Exzitonübergängen werden bestimmt. Beliebige Besetzungszustände können eingeschrieben werden, indem kohärente Populationsoszillationen mittels resonanter Pulse getrieben werden, während verschränkte Überlagerungen von zwei Exzitonzuständen in einem einzelnen Quantenpunkt mit Hilfe von Quantenschwebungen auf transienten differentiellen Spektren untersucht werden. Wir nutzen schließlich die Wechselwirkung zwischen einem Quantenpunkt und einer absorbierenden Schicht in seiner Nähe aus um das Absorptionsspektrum des Quantenpunktes mittels lichtinduzierter transientser elektrischer Felder auf ultrakurzen Zeitskalen zu schalten.

Abstract

In this thesis, the coherent interaction of single semiconductor quantum dots and ultrafast optical pulses is studied. Under certain conditions, localized exciton transitions in quantum dots can be seen as semi-isolated two-level systems. While this description is sufficient for the explanation of some observations in coherent experiments, it is sometimes necessary to explicitly consider coupling of the discrete quantum states confined to the dot with the environment. We start out from simple, classical examples of coherent spectroscopy and then turn towards experiments where the interaction with the vicinity of the dot becomes an important factor.

First, a novel method for transient differential reflectivity spectroscopy of single quantum systems is introduced. It is a pure far-field optical technique which does not require any sophisticated sample preparation steps which makes it applicable to a broad range of structures. Pump pulses excite the sample structure and probe pulses read out the pump-induced changes in the system after a variable delay time. In the case of a single dipole, the signal is given in the form of the spectral interferogram between the backscattered wave from the particle and the probe light which is reflected at the sample surface. This form of homodyne detection amplifies the weak scattered wave from the particle and thus makes this kind of spectroscopy for single quantum dots feasible.

In the remainder of this thesis our spectroscopic method is applied to either characterize the coherent properties of single quantum dots, to prepare and read-out a desired quantum state or to deliberately manipulate them. Coherence times and oscillator strengths are determined for localized exciton transitions. Arbitrary population states can be written by driving coherent population oscillations using resonant pulses, while entangled superpositions of two exciton states in a single dot are investigated by quantum beats on transient differential spectra. We finally exploit the interaction between the dot and a nearby absorbing layer to switch the dot's absorption spectrum on ultrafast timescales via light-induced transient electric fields.

Publications

Parts of this work have already been published:

In scientific journals:

- C. Wolpert, C. Dicken, L. Wang, P. Atkinson, A. Rastelli, O. G. Schmidt, H. Giessen, H. Schweizer, R. Singh, G. Bester, and M. Lippitz, *Ultrafast switching of localized excitons via transient photo-Dember fields*, Phys. Rev. Lett. (in preparation, 2012)
- C. Wolpert, C. Dicken, L. Wang, P. Atkinson, A. Rastelli, O. G. Schmidt, H. Giessen, and M. Lippitz, *Ultrafast coherent spectroscopy of a single self-assembled quantum dot*, Phys. Status Solidi B **249**, (4), 721–730 (2012)
- C. Wolpert, L. Wang, A. Rastelli, O. G. Schmidt, H. Giessen, and M. Lippitz, *Transient absorption spectroscopy of a single lateral InGaAs quantum dot molecule*, Phys. Status Solidi B **249**, (4), 731–736 (2012)
- C. Wolpert, C. Dicken, P. Atkinson, L. Wang, A. Rastelli, O. G. Schmidt, H. Giessen, and M. Lippitz, *Transient Reflection: A versatile technique for Ultrafast Spectroscopy of a Single Quantum Dot in Complex Environments*, Nano Lett. **12**,(1), 453-457 (2012)

At international conferences and workshops:

- C. Wolpert, C. Dicken, P. Atkinson, L. Wang, A. Rastelli, O. G. Schmidt, H. Giessen, and M. Lippitz, *Nonlinear Spectroscopy of Single Quantum Dots*, invited talk, ICOOPMA12, Nara (2012)
- M. Pfeiffer, K. Lindfors, C. Wolpert, C. Dicken, P. Atkinson, M. Beyoucef, A. Rastelli, O. G. Schmidt, H. Giessen, and M. Lippitz, *Ultrafast Spectroscopy of Coupled Quantum Dots*, talk, Fourth international workshop on *Positioning of single nanostructures*, Lake Como (2011)
- C. Wolpert, C. Dicken, L. Wang, P. Atkinson, A. Rastelli, O. G. Schmidt, H.

- Giessen, and M. Lippitz, *Ultrafast spectroscopy of single quantum dots*, poster, Fourth international workshop on *Positioning of single nanostructures*, Lake Como (2011)
- C. Wolpert, L. Wang, P. Atkinson, A. Rastelli, O. G. Schmidt, and M. Lippitz, *Coherent Spectroscopy of Single Semiconductor Quantum Dots*, poster EA.P.8, CLEO/Europe-EQEC, München (2011)
 - C. Wolpert, L. Wang, P. Atkinson, A. Rastelli, O. G. Schmidt, and M. Lippitz, *Transient Differential Reflection Spectroscopy Single Lateral InGaAs Quantum Dot Molecules*, talk HL 71.10, DPG spring meeting, Dresden (2011)
 - C. Wolpert, L. Wang, P. Atkinson, A. Rastelli, O. G. Schmidt, and M. Lippitz, *Rabi oscillations and quantum beats in single GaAs/AlGaAs quantum dots*, poster, Workshop on Nanophotonics meets Quantum Optics, Bad Honnef (2010)
 - C. Wolpert, L. Wang, P. Atkinson, A. Rastelli, O. G. Schmidt, H. Giessen, and M. Lippitz, *Rabi oscillations in single GaAs/AlGaAs quantum dots*, talk Th.2.3, NOEKS10, Paderborn (2010)
 - C. Wolpert, L. Wang, P. Atkinson, A. Rastelli, O. G. Schmidt, H. Giessen, and M. Lippitz, *Coherent Spectroscopy of Single GaAs Quantum Dots*, talk QFD3, CLEO/QUELS, San Jose (2010)
 - C. Wolpert, L. Wang, P. Atkinson, A. Rastelli, O. G. Schmidt, and M. Lippitz, *Coherent spectroscopy of single GaAs/AlGaAs quantum dots*, talk HL 59.4, DPG spring meeting, Regensburg (2010)
 - C. Wolpert, K. Lindfors, M. Pfeiffer, M. Huber, L. Wang, P. Atkinson, A. Rastelli, O. G. Schmidt, and M. Lippitz, *Coherent spectroscopy of single GaAs quantum dots*, talk, Third international workshop on *Positioning of single nanostructures - Single quantum devices*, Freudenstadt-Lauterbad (2009)
 - C. Wolpert, M. Huber, M. Lippitz, L. Wang, A. Rastelli, and O. G. Schmidt, *Two-color pump-probe spectroscopy of self-assembled GaAs/AlGaAs quantum dots*, talk HL 13.4, DPG spring meeting, Dresden (2009)

Additional scientific publications which are not presented in this thesis:

In scientific journals:

- T. Lutz, A. Kabakchiev, T. Dufaux, C. Wolpert, Z. Wang, M. Burghard, K. Kuhnke, and K. Kern, *Scanning Tunneling Luminescence of Individual CdSe Nanowires*, *Small* **7**,(16), 2396-2400 (2011)
- M. Pfeiffer, K. Lindfors, C. Wolpert, P. Atkinson, M. Benyoucef, A. Rastelli, O. G. Schmidt, H. Giessen, and M. Lippitz, *Enhancing the Optical Excitation Efficiency of a Single Self-Assembled Quantum Dot with a Plasmonic Nanoantenna*, *Nano Lett.* **10**,(11), 4555-4558 (2010)

At international conferences and workshops:

- M. Pfeiffer, K. Lindfors, C. Wolpert, P. Atkinson, M. Beyoucef, A. Rastelli, O. G. Schmidt, H. Giessen, and M. Lippitz, *Coupling Plasmons and Excitons in Single Quantum Dots*, poster, Fourth international workshop on *Positioning of single nanostructures*, Lake Como (2011)
- M. Pfeiffer, K. Lindfors, C. Wolpert, P. Atkinson, A. Rastelli, O. G. Schmidt, H. Giessen, and M. Lippitz, *Nano-plasmonics with single epitaxial quantum dots*, talk DS 56.1, DPG spring meeting, Dresden (2011)
- T. Lutz, A. Kabakchiev, T. Dufaux, C. Wolpert, M. Burghard, K. Kuhnke, and K. Kern, *STM induced electroluminescence from individual CdSe nanowires*, talk O 76.4, DPG spring meeting, Regensburg (2010)
- M. Huber, C. Wolpert, and M. Lippitz, *Interferometric measurement of polarization dynamics in QDs*, poster HL 48.52, DPG spring meeting, Dresden (2009)

Contents

Zusammenfassung	1
Abstract	3
Publications	5
1 Introduction	11
2 Semiconductor quantum dots	15
2.1 Introduction to low-dimensional semiconductors	16
2.2 Epitaxial growth of unstrained GaAs/AlGaAs quantum dots	19
2.3 Optical properties of GaAs/AlGaAs quantum dots	21
2.4 Applications of semiconductor quantum dots	26
2.4.1 Coupling of localized excitons and single nanoantennas	26
2.4.2 Quantum gates in single quantum dots	28
3 Transient differential reflectivity spectroscopy of single quantum dots	31
3.1 Overview	32
3.2 Experimental setup	34
3.2.1 Laser system	35
3.2.2 Pulse preparation	37
3.2.3 Laser-scanning confocal microscope	42
3.3 Signal formation	45
3.4 Filming excitons: Free induction decay	52
3.5 Conclusion	55
4 Rabi oscillations in single GaAs quantum dots	57
4.1 Introduction	58
4.2 Quantum mechanics of a two-level system	58
4.2.1 Time dependent Schrödinger equation	59
4.2.2 Optical Bloch equations	62
4.2.3 Relaxation phenomena	64
4.3 Experimental technique	66
4.4 Experimental results	67
4.5 Conclusion	71

5	Ultrafast switching of excitons	73
5.1	Band absorption in bulk GaAs and vertical electric fields	74
5.1.1	The photo-Dember effect and ultrafast screening in GaAs	74
5.1.2	Monitoring the carrier density in the GaAs cap	80
5.2	Experimental technique	82
5.3	Results	86
5.3.1	Pump 180 meV above the bandgap energy of GaAs	87
5.3.2	Pump 7 meV above the bandgap energy of GaAs	90
5.4	Conclusion and outlook	92
6	Coherent beats in a single GaAs quantum dot	95
6.1	Introduction	96
6.2	Entangled two-qubit states	96
6.3	Photoluminescence characterization of the quantum dot	97
6.4	Coherent beats in a single quantum dot	98
6.5	Conclusion	103
7	Spectroscopy of lateral InGaAs quantum dot molecules	105
7.1	Introduction	106
7.2	Fabrication and processing	106
7.3	Linear optical properties	108
7.4	Rabi oscillations of a single exciton transition in a QDM	113
7.5	Comparison of emission and transient absorption spectra	115
7.6	Bias dependent photoluminescence	116
8	Conclusion	123
9	Outlook	127
	List of acronyms	129
	Figures	132
	Tables	135
	References	136
	Lebenslauf	155
	Acknowledgments	157

1 Introduction

Over the last decades so-called *artificial atoms* have attracted much attention in the field of condensed-matter research and the optical sciences. *Artificial atoms* are single quantum systems with discrete states such as nitrogen vacancy centers in diamond [1], colloidal semiconductor nanocrystals [2] and epitaxial semiconductor quantum dots [3]. Their longevity and robustness gives them a clear advantage over single molecules which are subject to photobleaching and chemical instability. *Artificial atoms* are already widely used as markers in bio-medical imaging [4] and as local probes [5]. They also have a high potential for applications as stationary quantum bits (qubits) in quantum information science [6] and in studying fundamental light-matter interaction. In this context, self-assembled semiconductor quantum dots (QDs) are of particular interest. QDs are nanometer-sized inclusions of a guest semiconductor in a host semiconductor crystal [7]. The finite size of these nanostructures leads to a discrete density of electronic states due to quantum confinement effects. As a consequence, their absorption spectrum consists of isolated lines which can be attributed to optical transitions involving confined states. QDs can be fabricated with a high quality using standard thin film deposition techniques such as molecular beam epitaxy (MBE) [8] or metal-organic vapor phase epitaxy (MOVPE) [9,10]. Pure samples of high quantum efficiency can be obtained in this way for different material systems. Optical properties such as the position of transition lines can be controlled to a certain degree by adjusting the material and growth parameters.

On the one hand, self-assembled growth of solid-state single quantum objects has the potential to tailor the properties of the structure to fit specific requirements. On the other hand, a solid-state system brings with it many challenges in fabrication and experiment design. An ideal *artificial atom* would be well isolated from its environment and only relax radiatively by emitting a photon, such as a single atom in a trap. However, in a semiconductor crystal confined electronic states are never actually isolated from their environment [11]. They are, for example, affected by charges in their vicinity [12] and they interact with phonons [13], leading to a nonzero nonradiative relaxation rate, loss of coherence and inhomogeneous broadening due to spectral diffusion [14]. Another challenge arises from the fact that no two QDs are alike. Single atoms and molecules of the same type are identical and only differ in their environment. Two individual QDs, on the other hand, will always differ in size and shape which leads, in turn, to the emission of distinguishable photons. This problem can be overcome by controlling the electronic properties of the QD with external tuning techniques via electric or magnetic fields,

1 Introduction

strain or temperature. In this way, interference of photons emitted from two individual QDs could already be demonstrated [15].

Several spectroscopic techniques are applied in order to characterize or manipulate localized excitons in QDs. Photoluminescence (PL) emission spectroscopy is a powerful tool for the measurement of transition energies and radiative lifetimes. Coherent properties can be extracted by four-wave mixing (FWM) [16] techniques and resonance fluorescence [17]. With excited state lifetimes below 1 ns we have to employ ultrafast optical pulses in order to coherently excite localized bound electron-hole pairs (excitons) in a QD. Coherent light-matter interaction between short light pulses and the exciton system allows for the preparation of a desired exciton state and its manipulation.

The goal of this thesis is the coherent spectroscopy of single QDs including quantum state preparation and subsequent readout of the exciton state. A special focus is put on the coupling between a single QD and its environment, such as an absorbing layer, a nearby QD in a quantum dot molecule (QDM) or future studies on hybrid systems formed by a QD and a plasmonic nanoantenna. Hybrid quantum systems combining a quantum dot with a microcavity [18, 19] or a particle plasmon [20–23] can enhance light-matter interaction. More complex and challenging applications require the controlled interaction of many quantum systems in a network. Recent proposals envision the entanglement of quantum dots by means of plasmonic waveguides [24] or the use of quantum dots as optical transistors [25]. These diverse aims call for a robust and flexible optical technique with minimal requirements on sample preparation. Far-field differential reflection spectroscopy is such a technique, as it essentially only requires optical access to the sample from one side and thus leaves as many degrees of freedom as possible to the sample design. Transmission experiments are not an option for absorbing samples. The use of lithographically defined nearfield apertures is not advisable for the study of hybrid systems as they will in many cases not fit on top of the structure and they also may perturb the quantum system of interest in a profound way. In simple words, when the spectroscopic technique does not rely on specific structural properties of the sample in order to give satisfying results, it is applicable to a broad range of possible complex quantum systems.

This thesis is essentially divided into two major parts. The first part includes chapters 2 and 3 and introduces the QD structures used in this work as well as the experimental setup. It is followed by a second part which is comprised of chapters 4 to 7. In this part our spectroscopic method is used for the preparation of arbitrary population states and entangled superpositions of exciton states. We demonstrate an all-optical ultrafast switch based on a single QD and apply our method to lateral double dot structures. In detail this work is structured as follows:

The first chapter of this thesis starts with a general introduction to low dimensional semiconductor structures. Then, electronic and optical properties of self-assembled GaAs/AlGaAs QDs, which were mainly used in this work, are derived considering their

reduced symmetry and confinement effects. Representative characterization measurements, such as polarization-resolved PL and power-dependent PL, are presented. Two fields of application for QDs from the literature are discussed in greater detail. First, the coupling of single GaAs QDs to plasmonic nanoantennas for enhanced light-matter interaction is discussed. For this purpose the dot layer needs to be very close to the sample surface so that the evanescent electric field of the particle plasmon is still high enough at the location of the QD. Secondly, an example from the field of quantum information and quantum computation is presented. In this case a controlled rotation (CROT) quantum gate was realized in the diamond-level system formed by the biexciton and exciton levels in a single quantum dot.

In chapter 3 the experimental setup in our laboratory is introduced. We use a double-modulated two-color pump-probe technique in order to record transient differential reflectivity spectra from single semiconductor QDs. Pump and probe pulses are derived from a Ti:Sapphire laser by optical pulse-shaping. The shape of recorded differential reflectivity spectra is described as the spectral interferogram of the backscattered field from the QD and the probe field that is reflected at the sample surface. At the end of the chapter perturbed free induction decay (PID) of a localized exciton is discussed as a basic example for a single dot pump-probe experiment. Here, differential reflectivity spectra were recorded as a function of the time delay between pump and probe pulses. In the case where the pump arrives at the QD after the probe pulse it perturbs the coherent polarization that the resonant probe created in the exciton state. Resulting oscillatory features in the spectra can be reproduced by a simple density matrix model involving the crystal ground state and two exciton states arranged in a quantum mechanical V-system. From this simple experiment the dephasing time of the exciton state can be obtained as the decay time of the PID signal for negative delay times.

We discuss Rabi-oscillations on the ground state exciton transition in a single GaAs QD in chapter 4. When the pump pulses interact coherently with the exciton transition they can coherently drive the entire population in the system to the excited state and, with increasing pump power, also back again to the ground state. In this way arbitrary population states can be prepared in the QD. The situation in our QD structures is particularly interesting, as an absorbing GaAs substrate is only separated by 10 nm of AlGaAs from the QD layer. The influence of delocalized free carriers in the GaAs substrate, which are excited as a side product by the pump pulses resonant to the QD exciton, is investigated. A phenomenological model considering the above mentioned background carrier contribution can describe our experimental data very well with a saturating Rabi-frequency at elevated pump powers. Datasets on various individual dots are presented and their transition dipole moments are extracted from the period of their Rabi-oscillations with respect to pump power.

The interaction between an exciton in a single QD and delocalized background carriers in the GaAs substrate is investigated more directly in chapter 5. Now we excite the substrate selectively with pump pulses having a photon energy smaller than the lowest

1 Introduction

confined state in the QD and which, as a consequence, do not excite the dot at all. The absorption by the QD is measured with resonant probe pulses so that the influence of the carrier density in the substrate on the nearby QD can be studied directly. It turns out that the absorption spectrum of the localized exciton is redshifted, decreased in amplitude and broadened with increasing background carrier density. This effect was studied both in the power domain and in the time domain. Our data shows, that a hot charge carrier cloud underneath the QD can switch its absorption spectrum on ultrafast timescales with a recovery time of about 50 ps. We could successfully reproduce our experimental data using a model involving vertical pump-induced electric fields (photo-Dember effect) which influence the QD exciton via the quantum-confined Stark-effect.

The preparation of entangled superposition states of the two orthogonal ground state excitons is presented in chapter 6. By choosing the polarization directions of our pump and probe fields at 45° with respect to the excitonic axes, we excite and probe coherent superpositions of both exciton states. As the frequency of both transitions differ by their fine-structure splitting (FSS), a coherent superposition manifests itself in quantum beats on a series of differential reflectivity spectra recorded as a function of delay time. We can identify the mutual Raman coherence time of the two exciton states with the damping time of their quantum beat signature which is superimposed on the incoherent population decay.

It is known that the PL emission from lateral InGaAs quantum dot molecules (QDMs) can be controlled by an external bias voltage that is applied along the molecular axis. In chapter 7 we investigate this bias tuning behavior in absorption via transient differential reflectivity measurements. First, the QDM on which we perform ultrafast measurements was characterized by power-dependent PL emission spectroscopy for different bias voltage regimes. Then, the optimal pump power is determined by driving one Rabi-cycle on the neutral exciton in one dot. Finally, the absorption by the QDM is monitored as the bias voltage is scanned. With transient absorption measurements it is possible to obtain more information about the system than with standard PL studies. Transient absorption does not rely on the emission of a photon in order to produce a signal. This means that states which relax mostly non-radiatively can also be investigated.

At the end of this thesis a conclusion of the presented work is given. Possible future experiments and next steps are discussed in a brief outlook.

2 Semiconductor quantum dots

Semiconductor quantum dots (QDs) are mesoscopic structures in which the wavefunctions of carriers are confined in all three spatial dimensions. As a result, they exhibit a discrete density of states (DOS) for confined excitonic states and are consequently referred to as artificial atoms. Control of the structure's topology and composition opens the opportunity of tailoring electronic and optical properties. Techniques for deterministic positioning of QDs on a sample make them even more appealing for new applications ranging from laser amplifiers to quantum computation. Dots which are grown in close proximity to the crystal surface have the potential to be coupled to plasmonic nanoantennas. The enhancement of the local density of states near the antenna could lead to a more efficient photon extraction from the high index GaAs structure. In this work we focus on strain-free GaAs QDs which are embedded in AlGaAs barriers. This material system shows neutral exciton transitions around 1.7 eV where Si-based photodetectors have still very high quantum efficiencies. This and the fact that they can be grown with low surface densities makes them very appealing for experiments on single dots. We characterized the optical properties of single QDs by polarization-resolved photoluminescence (PL) spectroscopy in combination with power-dependent measurements in order to prepare for future coherent experiments.

2.1 Introduction to low-dimensional semiconductors

In atoms, electrons can only assume states at discrete, well separated energies [26]. These atomic orbitals hybridize when several atoms form a molecule. When two hydrogen atoms develop a bond and form a hydrogen molecule, for instance, the 1s orbitals hybridize and split into a low-energy bonding and a high-energy antibonding molecular orbital [27]. The density of states (DOS) in big molecules can therefore be quasi-continuous as more molecular orbitals fall into a certain energy interval. Molecular spectra consist of sometimes even overlapping bands which are made up from transitions involving changes in electronic, rotational, and vibrational degrees of freedom [28]. Electronic states in solids are described by continuous bands. The most simple picture is the free electron model where electrons can move freely in a large potential well [29] like in a perfect metal. The potential has the constant value $V_0 = 0$ in the metal of size L and infinity on the outside. The Schrödinger equation then reads

$$-\frac{\hbar^2}{2m}\Delta\psi(\mathbf{r}) + V(\mathbf{r})\psi(\mathbf{r}) = E\psi(\mathbf{r}) \quad , \quad (2.1)$$

where the potential can be written as

$$V(x, y, z) = \begin{cases} 0 & \text{for } 0 \leq x, y, z \leq L \\ \infty & \text{otherwise} \end{cases} \quad . \quad (2.2)$$

We can see that the electron will always stay inside the metal as the potential is infinity on the outside. Solutions to the Schrödinger equation are then of the form

$$\psi(\mathbf{r}) = \left(\frac{2}{L}\right)^{3/2} \sin(k_x x)\sin(k_y y)\sin(k_z z), \quad (2.3)$$

with energy eigenvalues of

$$E = \frac{\hbar^2 k^2}{2m} = \frac{\hbar^2}{2m} (k_x^2 + k_y^2 + k_z^2) \quad . \quad (2.4)$$

These are just the energies of a free electron, however, the finite size of the crystal imposes a constraint for the \mathbf{k} -vector of the wavefunction

$$k_x = \frac{\pi}{L_x} n_x, \quad k_y = \frac{\pi}{L_y} n_y, \quad k_z = \frac{\pi}{L_z} n_z \quad \text{with } n_x, n_y, n_z = 1, 2, 3, \dots \quad . \quad (2.5)$$

When a periodic potential from the crystal is considered the wavefunctions of carriers can be written according to Bloch's theorem as a product of a freely propagating wave and a function which has the same periodicity as the crystal. When \mathbf{R} is a lattice vector of the crystal then the Bloch wave can be written as

$$\phi_{\mathbf{k}}(\mathbf{r}) \propto e^{i\mathbf{k}\mathbf{r}} \mathbf{u}_{\mathbf{k}}(\mathbf{r}), \quad \text{with } \mathbf{u}_{\mathbf{k}}(\mathbf{r}) = \mathbf{u}_{\mathbf{k}}(\mathbf{r} + \mathbf{R}) \quad . \quad (2.6)$$

band	degeneracy	J	m_J	effective mass at Γ -point
conduction (c)	2	1/2	$\pm 1/2$	$m_c^* = 0.063 m_0$
heavy-hole (hh)	2	3/2	$\pm 3/2$	$m_{hh}^* = 0.51 m_0$
light-hole (lh)	2	3/2	$\pm 1/2$	$m_{lh}^* = 0.082 m_0$
spin-orbit split-off (so)	2	1/2	$\pm 1/2$	$m_{so}^* = 0.15 m_0$

Table 2.1: Bandstructure of GaAs around the Γ -point including the total angular momentum quantum numbers J , the magnetic quantum numbers m and the effective masses m^* in terms of the free electron mass m_0 .

In semiconductors there are occupied valence bands and mostly unoccupied conduction bands which are separated by a minimal bandgap energy E_{gap} . GaAs is a direct semiconductor. In this case, the valence band maximum and the conduction band minimum are both at the Γ -point ($\mathbf{k} \cong 0$) in the center of the Brillouin zone. Around this region we can approximate the dispersion of charge carriers very well by parabolic bands [29, 30]. In zinc-blende-type semiconductors, such as in GaAs, the conduction band is formed from atomic s-orbitals, whereas the valence bands have p_x and p_y character [31]. This leads to a twofold degenerate conduction band and three twofold degenerate valence bands at the Γ -point, when we combine the orbital angular momentum of 1 with the the angular momentum of 1/2 from the spin. For an angular momentum quantum number of $J = 3/2$ we get the heavy hole band ($m_J = \pm 3/2$) and the light hole band ($m_J = \pm 1/2$). With $J = 1/2$ we get the so-called 'spin-orbit split-off band' which is reduced in energy with respect to the other two valence bands by the spin-orbit coupling.

Due to the periodic crystal potential, the electrons' response to an electric field is dependent on their k -vector [30, 32]. The electron behaves as if its mass were dependent on its position in reciprocal space. This concept is expressed by the effective mass m^* of electrons in solids. At the center of the Brillouin zone we can assume that the effective mass is constant (*effective mass approximation*) and the bands are described well by parabolae like in Eq. 2.4. The dispersion relation for the conduction band then reads

$$E_e(\mathbf{k}) = E_C + \frac{\hbar^2 k^2}{2m^*} , \quad (2.7)$$

with E_C being the conduction band offset. As one can easily see from the above equation, the effective mass is inversely proportional to the second derivative of the energy with respect to the k -vector, or the curvature of the band. This means, that in the center of the Brillouin zone electrons are quasi-free and have a positive effective mass, whereas, at the boundary of the zone, where the bands are flat and where they can no longer be described by a parabola, the effective mass even becomes negative. Table 2.1 summarizes the band structure of GaAs around the center of the Brillouin zone involving the above mentioned valence and conduction bands.

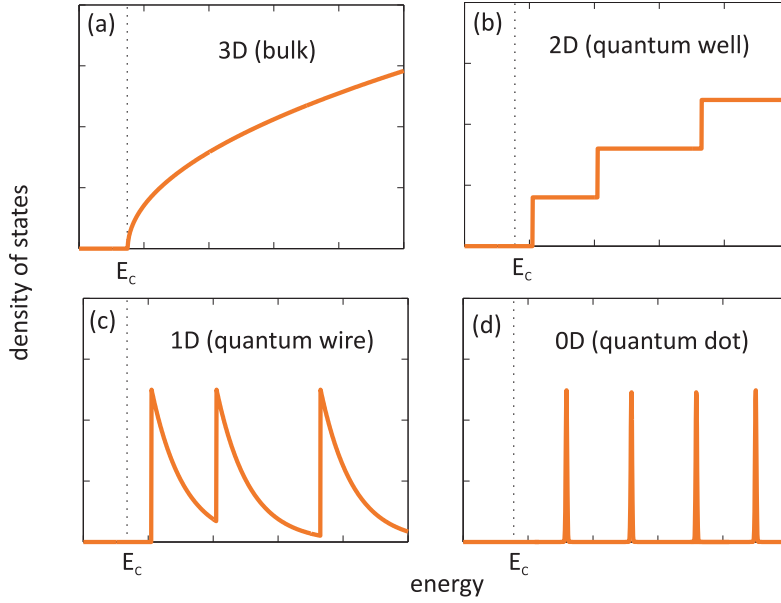


Figure 2.1: Single electron density of states (DOS) in the center of the Brillouin zone. Ideally, the DOS grows like the square root of the distance from the conduction band edge (E_c) in bulk semiconductors (a). Cases for confinement along different dimensions are depicted. For confinement along one dimension the electron can move freely in the plane perpendicular to the confinement direction, resulting in plateaus of constant DOS. In quantum wires the DOS is singular at the subband edges but still a continuum (c), whereas in quantum dots, finally, the DOS becomes completely discrete (d).

When the size of the semiconductor crystal is reduced now along one dimension, we decrease the amount of possible k -vectors that the carriers can assume, according to Eq. 2.5. The confinement of the carriers' wavefunctions is reflected in the DOS of the system when a dimension becomes comparable in size to the de Broglie wavelength of the electron. At a temperature T the de Broglie wavelength is given by

$$\lambda_{dB} = \frac{2\pi\hbar}{\sqrt{3m_{e,h}^*k_B T}} \quad , \quad (2.8)$$

where k_B is the Boltzmann constant. For GaAs at room temperature $\lambda_{dB} \approx 25$ nm. AlGaAs has a higher bandgap energy than GaAs so that a thin film of GaAs between two AlGaAs barriers forms a potential well along the growth-direction. In this case electrons can still move freely in the sample plane, however, they can only populate discrete modes in the growth direction. This quasi-2D hetero-structure is called quantum well (QW). In a QW the in-plane motion becomes decoupled from the carriers' motion in the z -direction [33] and their energy can be written as

$$E_{QW} = E_z + E_{in-plane} \quad , \quad (2.9)$$

where E_z is quantized and $E_{\text{in-plane}}$ is just the energy of a free carrier according to Eq. 2.7. On Fig. 2.1 the DOS is sketched for different confinement cases [34]. Subfigure (a) shows the square-root behavior in a bulk material, whereas subfigure (b) shows the DOS for a QW. We can see that the DOS is still continuous, as the carriers are free in the xy-plane. However, the confinement along the z-direction leads to jumps in the DOS where a new discrete energy level in E_z can be populated. We can understand the confinement as a particle-in-a-box problem, where the z-component of the k-vector can only assume discrete values which can be identified with a step-function shaped subband. The case of a quantum wire with confinement along two dimensions is depicted on Fig. 2.1(c). Here, the DOS is piled up further at the subband edges but stays continuous. Only in quasi-0D quantum dot (QD) structures, where the carriers are confined in all three spatial dimensions, we can expect fully discrete states (c).

2.2 Epitaxial growth of unstrained GaAs/AlGaAs quantum dots

Semiconductor QDs can be categorized from a growth point of view into wet-chemically fabricated colloidal QDs and epitaxially grown self-assembled QDs. Colloidal dots, such as CdSe dots are generally spherical with diameters of 1-100 nm [35]. They suffer from blinking, which means that they switch statistically between a bright 'on-state' and a dark 'off-state' [36] due to fluctuations in their environment. In order to overcome this problem and to improve the optical properties core-shell architectures are understood as a key concept to shield the localized exciton from the environment [37]. They are, however, an ideal non-bleaching tool for labeling of cells [38], nucleic acids and proteins [39] for fluorescence detection. Epitaxial dots can be grown by molecular beam epitaxy (MBE) or by metal-organic vapor-phase epitaxy (MOVPE). In MOVPE, metal-organic precursor gases react on a heated substrate surface depositing thin layers of semiconductor material [40]. The structures which were investigated in this work were grown in an MBE chamber, where adatoms are evaporated from effusion cells and impinge on a heated substrate in an ultra-high vacuum (UHV) chamber. On the surface the adatoms are free to move and organize into thin films or nanoislands. There are three basic growth modes which are schematically depicted on Fig. 2.2. When adatoms A are deposited on a substrate which consists of atoms of the type B and which has a lattice constant different from A, the growth dynamics depend strongly on the surface tensions γ_i and the energies σ_i of the different interfaces [41, 42]. The important parameter is the sum $\Delta\sigma$ of the surface energy contributions from the deposited film σ_A , the substrate σ_B and from the film-substrate interface σ_{AB} :

$$\Delta\sigma = \sigma_A - \sigma_B + \sigma_{AB} . \quad (2.10)$$

When the substrate contribution dominates ($\Delta\sigma < 0$ and $\gamma_B > \gamma_A + \gamma_{AB}$) the adatoms are wetting the substrate surface and a strained film is growing. This scenario is called

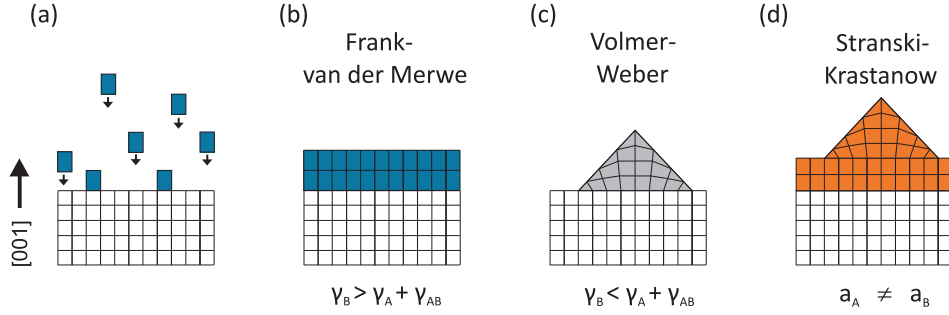


Figure 2.2: In an MBE chamber adatoms A are deposited on a substrate composed of atoms of the type B (a). In the Frank-van der Merwe growth mode the surface tension between atoms B and the vacuum γ_B is higher than between atoms A and the vacuum γ_A and between atoms A and B at the interface γ_{AB} . Volmer-Weber growth is just the opposite case. Stranski-Krastanow growth takes place at an intermediate regime where the nucleation of islands on top of a thin wetting layer is induced by strain due to a lattice mismatch between the crystals of A and B.

Frank-van der Merwe growth and it is depicted on Fig. 2.2(b). Here, the deposited film grows with the same lattice constant as the substrate material (pseudomorphic growth). The other extreme is just the opposite case where the layer term dominates ($\Delta\sigma > 0$ and $\gamma_B < \gamma_A + \gamma_{AB}$) and the adatoms do not wet the surface. This leads to the growth of isolated islands as shown on Fig. 2.2(c) and it is referred to as Volmer-Weber growth. We enter an interesting regime when the situation is just in the middle of the two extremes introduced above. In the so-called Stranski-Krastanow mode the process starts by the growth of a strained layer. During growth a critical thickness is reached, where the sign of $\Delta\sigma$ changes due to increased strain in the deposited layers. At this point quantum dots form on top of a thin quantum well (wetting layer) as sketched on Fig. 2.2(d).

Most quantum emitters used in this thesis are epitaxial GaAs quantum dots in AlGaAs barriers [43]. As the dot material and the barrier material have nearly identical lattice parameters, GaAs quantum dots in an AlGaAs barrier cannot be grown by strain-induced mechanisms like the Stranski-Krastanov growth mode discussed above. This is why our dots were formed by filling GaAs into self-assembled nanoholes that were prepared at low density in the lower AlGaAs layer. For details see reference [44]. Our samples were grown by a solid-source molecular-beam epitaxy (MBE) machine equipped with an *in-situ* AsBr₃ gas etching unit. The subsequent growth steps are depicted on Fig. 2.3. As a first step, a layer of sacrificial self-assembled InAs QDs are grown on the GaAs substrate on a (001)-surface (a). The nominal substrate temperature was 500 °C. Then, a 10 nm GaAs layer was grown on top of the InAs quantum dots resulting in partially capped dots. As a result of the strain-enhanced and material-selective etching rate, bow-tie-shaped nanoholes were created by removing the buried InAs QDs by *in situ* nominal 5-nm-deep AsBr₃ etching (b). The formed nanoholes were overgrown with 10 nm Al_{0.45}Ga_{0.55}As, which serves as the lower barrier of the potential well. For

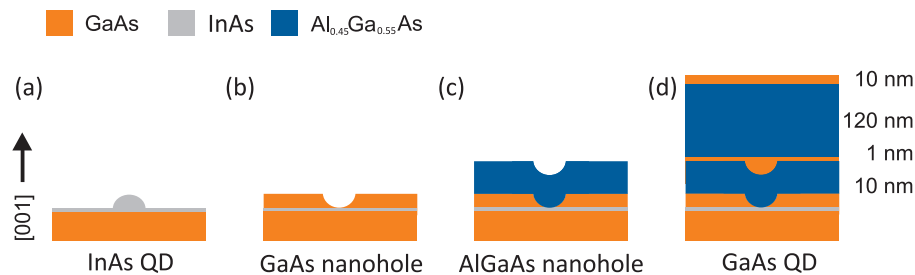


Figure 2.3: Schematic illustration of the growth process of unstrained GaAs/AlGaAs QDs. Sacrificial InAs dots are grown on a GaAs substrate (a). The dots are partially overgrown and removed by a selective AsBr_3 -etching step, resulting in nanoholes on GaAs (b). Nanoholes are transferred into lower AlGaAs barrier (c). Inverted GaAs QDs form when filling the holes in the lower barrier. Upper barrier and cap for chemical stability of the sample are grown (d).

moderate barrier thickness the nanoholes are preserved due to the low mobility of the AlGaAs (c). As the next step, GaAs is deposited as the lower band gap material. To close the holes completely by diffusion, the growth was interrupted for one minute during which the sample was still kept at a temperature of 500 °C. This results in inverted GaAs QDs lying underneath a 1 nm thick wetting layer with a smooth surface. Then the upper barrier layer of $\text{Al}_{0.45}\text{Ga}_{0.55}\text{As}$ is grown completing the confinement potential for electron and hole wavefunctions in the dot. As a last step the GaAs capping layer is deposited in order to avoid oxidation of AlGaAs due to the exposure to air. The finished structure is sketched schematically on Fig. 2.3(d). All single GaAs dots used in experiments presented in this thesis were grown with a lower barrier thickness of 10 nm and a dot layer with a nominal thickness of 1 nm, resulting in dots of nominally about 3 nm in height, 70 nm in length and a width of 50 nm [43].

2.3 Optical properties of GaAs/AlGaAs quantum dots

Until now we have only discussed single particle states for electrons and holes in semiconductor structures. Optical excitation of semiconductors involving inter-band absorption, however, promotes one electron from the valence band to the conduction band. This leaves a hole in the valence band and thus creates always one electron hole pair per absorbed photon. The energy of this system is not given by just the sum of the single-particle electron and hole states, but the Coulomb-interaction between the carriers has also to be accounted for. Due to the electrostatic attraction photocarriers in semiconductors form hydrogen-like quasiparticles, called excitons (X), which are just bound

2 Semiconductor quantum dots

electron-hole pairs. Their energy can be written as

$$E_X = E_e + E_h + E_{Coul} \quad . \quad (2.11)$$

As the Coulomb-energy of the exciton (exciton binding energy) is negative, the exciton state is shifted to smaller energies with respect of the free carrier gas. Just like the Bohr radius a_0 in a hydrogen atom, we can also define the exciton-Bohr radius in the same way:

$$a_{Bohr,X} = \frac{a_0 \epsilon}{\mu_e^*/m_e} \quad , \text{ with } a_0 = \frac{\hbar}{m_e c \alpha} \quad \text{and} \quad \mu^* = \frac{m_e^* m_h^*}{m_e^* + m_h^*} \quad (2.12)$$

Here, μ^* is the reduced effective mass of the electron and the hole and $\alpha = e^2/4\pi\epsilon_0\hbar c \approx 1/137$ is the fine-structure constant. In bulk GaAs an exciton in the Γ -valley has, for example, a binding energy of -4.7 meV and an exciton Bohr radius of 11.5 nm [45].

We can now formulate a criterion for the observation of confinement for excitons in nanostructures. Just like for free electrons, where the de Broglie wavelength is the critical length, we can use the exciton Bohr radius as a criterion for confinement. When the size of the structure is on the order of $a_{Bohr,X}$ we can expect confined states. One also refers to 'strong confinement' when the size of the nanostructure is much smaller than the exciton Bohr radius [46].

The absorption coefficient $\alpha_{0,X}$ of the groundstate to exciton transition is given by Fermi's Golden Rule:

$$\alpha_{0,X} \propto |\langle \psi_X | \hat{\epsilon} \mathbf{p} | \psi_0 \rangle|^2 \delta(\hbar\omega - (E_X - E_0)) \quad (2.13)$$

Here, $|\psi_{X,0}\rangle$ are the exciton state (final) and the crystal ground state (initial), $\hat{\epsilon}$ describes the polarization state of the light wave and \mathbf{p} is the dipole operator. Exciton transitions are only driven by the light field if the above integral is nonzero, i.e., the transition is dipole-allowed. In zinc-blende QDs excitons are formed from conduction band electrons and heavy-holes [31, 47]. The projection of the electron spin on the growth axis is 1/2 or -1/2, whereas the heavy-hole spin projection can be 3/2 or -3/2. From this we can construct exciton states with a total angular momentum along the z-axis of $M=\pm 1$ (antiparallel momenta) and $M=\pm 2$ (parallel momenta). The states with $M=\pm 2$ are called dark excitons, because they do not interact with optical fields due to the selection rules for optical dipole transitions ($\Delta M = \pm 1$, as the photon has an angular momentum of 1). The states $|\pm 1\rangle$ with $M=\pm 1$ are consequently referred to as bright excitons. The energy of dark excitons is lowered with respect to bright excitons by the short-range part of the electron-hole exchange interaction [48]. The two bright states are energetically degenerate in a dot with perfect cylindrical symmetry around an axis perpendicular to the sample plane and through the center of the dot. The polarization selection rules are such, that the two states can be excited by left and right handed circularly polarized photons. Most dots, and especially our GaAs dots, are not symmetric and so the degeneracy is lifted by the long-range part of the exchange interaction. In fact, our GaAs/AlGaAs dots are strongly elliptical resulting in a fine-structure splitting (FSS)

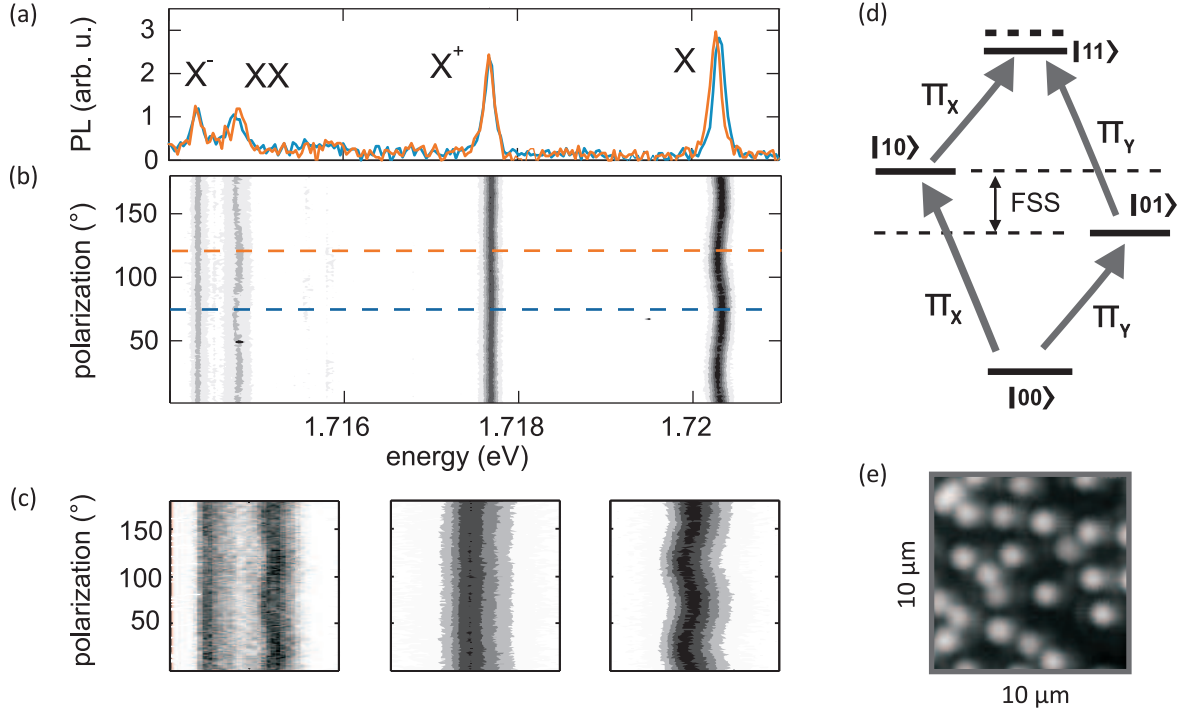


Figure 2.4: Photoluminescence spectra of a single GaAs QD exhibits a neutral exciton transition X , the positive trion X^+ , the biexciton transition XX and the negative trion X^- . Due to Coulomb interaction the biexciton transition is lower in energy than the single exciton transition. The exciton and biexciton emission is polarization dependent due to linear polarization selection rules and the nonzero fine-structure splitting of the exciton (a). Polarization-resolved spectral map of the photoluminescence emission (b). Magnified view of the spectral features shown above (c). Schematic energy level diagram for GaAs QDs (d). 10 by 10 μm PL image recorded by a confocal laser-scanning microscope (e).

between the orthogonal states $1/\sqrt{2}(|+1\rangle \pm |-1\rangle)$. The optical transitions between the crystal ground state and these two hybridized excitons are driven by orthogonal linearly polarized photons.

Polarization-resolved photoluminescence emission spectra of a single GaAs/AlGaAs quantum dot are shown on Fig. 2.4. The fundamental transition of the localized exciton is around 1.7 eV where the quantum efficiency of Si-based photodetectors is high. On Fig. 2.4(a) spectra are shown for two fixed detection polarizations indicated by the dashed lines on the complete spectral map (b). From low to high energy, the four peaks correspond to the negatively charged trion (X^- , two electrons and one hole), the biexciton (XX , two excitons), the positively charged trion (X^+ , two holes and one electron) and the neutral exciton (X). The emission energies of these transitions are differing due to Coulomb-interaction between the charge carriers in the dot. This is why the biexciton transition is redshifted with respect to the single exciton transition, for example. As

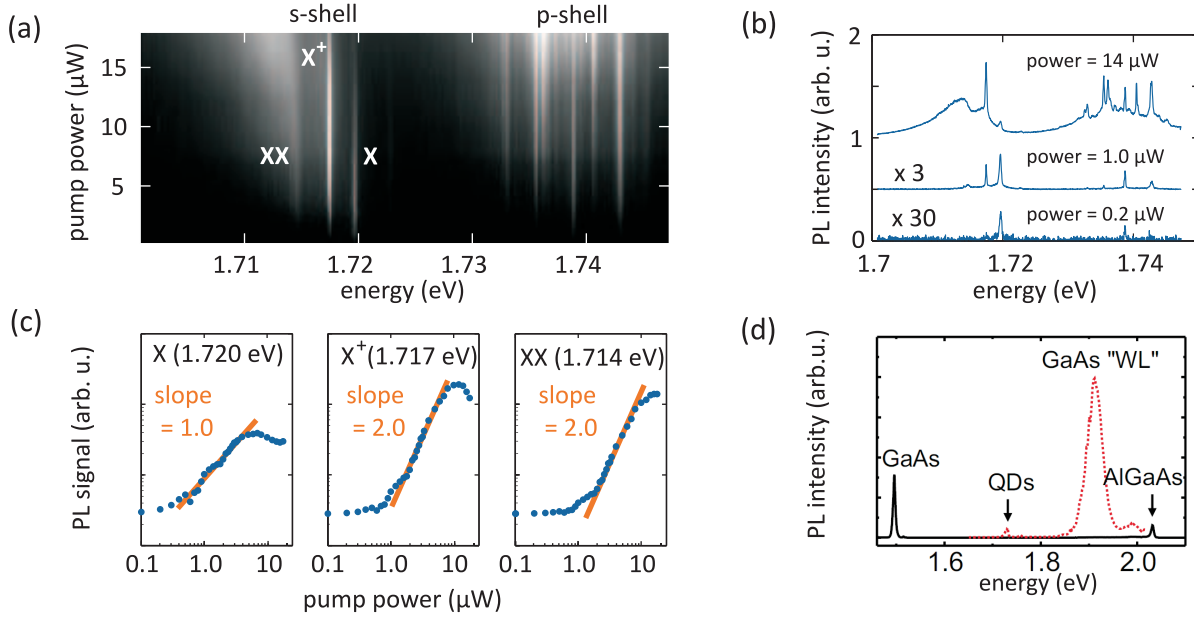


Figure 2.5: Photoluminescence spectra of a single GaAs QD as a function of pump power (a). P-shell becomes visible and the broadening of the emission indicates the formation of an electron-hole plasma at elevated pump powers. PL spectra for three different pump powers (b). Spectra have been shifted and scaled as indicated, for clarity. Integral PL-signal for the exciton (X), the positive trion (X^+) and the biexciton (XX) transition on a double logarithmic plot (c). The exciton signal scales linearly with the pump power, while the trion and the biexciton signals increase quadratically with pump power. PL in a wider spectral range (d) showing the emission from the GaAs substrate, the AlGaAs barriers, the wetting layer (WL) and the QDs. Subfigure (d) is reproduced after reference [50]

can be seen from the polarization-resolved map, the emission energy of the exciton and the biexciton are polarization dependent. This comes as a consequence of the elliptical shape of the quantum dot. The ellipticity of the quantum dot leads to linear polarization selection rules and a FSS in the order of $100 \mu\text{eV}$ between the two fundamental bright exciton states [49, 50]. Although the biexciton emission is polarization dependent, the level is not by itself split. It is a consequence of the FSS of the excitons. The trion lines appear as straight lines as they are not split. The polarization directions, Π_X and Π_Y , are oriented along the crystal axes $[\bar{1}10]$ and $[110]$. These spectral features are a consequence of the quantum-mechanical diamond system realized by the exciton-biexciton cascade which is sketched on Fig. 2.4(d). Subfigure (e) shows a $10\text{-by-}10 \mu\text{m}$ sized PL image recorded by our laser-scanning confocal microscope. It clearly shows, that our samples have a QD surface density which is low enough to perform single-dot spectroscopy using only optical far-field microscopy.

Figure 2.5 shows power-dependent PL measurements of a single dot. Every line in the full spectral map (a) represents a PL spectrum recorded at a certain pump power.

2.3 Optical properties of GaAs/AlGaAs quantum dots

In consequence, every column gives the PL emission at a specific photon energy. Three representative horizontal cuts through the spectral map are depicted on subfigure (b). One can see that for small powers the spectrum is dominated by the neutral exciton line (X). At intermediate powers, the positive trion (X^+) and biexcitons (XX) become stronger. Also emission from the p-shell of the exciton can be clearly identified. The p-shell contains transitions from the first excited exciton state. Finally, at high excitation powers, we see the s and p-shells as continuous spectral features reflecting the presence of an electron-hole plasma which is bound to the dot [51]. Generally, one can note, that at higher powers the emission features from multiexcitonic species and higher states becomes more dominant. Figure 2.5(c) shows the spectrally integrated PL emission for the neutral exciton transition, the positive trion transition and the biexciton transition as a function of the pump power on a double-logarithmic plot. As expected, the slope of the exciton curve is equal to 1.0 indicating a linear power-dependence. The slope for the other two transitions is 2.0 which means that their emission rises quadratic in pump power. Subfigure (d) shows the PL emission from our sample in a wide spectral range. The radiative recombination from the band edges of bulk GaAs substrate and the AlGaAs barriers is detected at around 1.5 and 2.0 eV, respectively. The GaAs wetting layer peaks at 1.9 eV and the QDs emit slightly above 1.7 eV.

In summary, we can fabricate semiconductor nanostructures which exhibit an atom-like density of states as a consequence to quantum confinement. Sharp spectral emission lines can be attributed to transitions between localized exciton states and the crystal groundstate. One might ask the question at this point what we gain when we use nanostructured semiconductors instead of single atoms or molecules as an individual quantum system. One of the most important advantages of solid state emitters is their robustness. In contrast to single molecules, QDs do not bleach or blink. The orientation of the optical dipole is fixed in space along the crystal axes, in contrast to single molecules and colloidal dots, where the dipole axes are oriented randomly in space. The fixed and well-known dipole axis makes self-assembled dots excellent candidates for controlled coupling schemes. A challenge in the design of QDs is the interaction with the solid state environment, such as phonon-induced dephasing of the exciton [52]. It is just this solid-state nature of QDs which also gives them oscillator strengths which can exceed values of 100 [53]. The oscillator strength is a measure of the amount of electrons which are taking part in a transition. That is why its value comes close to unity for transitions in single atoms and molecules. This means that in QDs, as many electrons in the crystal are involved in a transition, we observe comparatively strong light-matter interaction for a single quantum system.

2.4 Applications of semiconductor quantum dots

As already mentioned above, QDs have a high potential for innovation in many fields ranging from memories [54], amplifiers and lasers [55–58] to life science and medicine [59]. In this section two fields of QD research are introduced which are most relevant in the context of this thesis. First, the coupling of QDs to plasmonic nanoantennas for enhanced radiative decay rates and efficient photon extraction from the high refractive index GaAs sample is discussed. Secondly, the concept of quantum information is introduced. As an example, the realization of a quantum gate in a single QD is reviewed.

2.4.1 Coupling of localized excitons and single nanoantennas

QDs are true solid-state single quantum systems and ideal sources of single photons [60–63]. Self-assembled dots, however, are always surrounded by a high-refractive index semiconductor environment. The biggest part of the emission goes into the substrate and can not be extracted from the sample [64]. In order to overcome this challenge various approaches have been investigated. Hybrid quantum systems combining a quantum dot with a microcavity [18, 19, 65] or a particle plasmon [20–23] can enhance light-matter interaction. Particle plasmons are localized collective modes of an electron gas against the ionic cores, such as in a metal. With these coupled systems the quantum emitter can be more efficiently addressed optically and at the same time the spontaneous emission of a photon is enhanced [66–72]. This enhancement of the spontaneous emission rate can be understood with the concept of a local optical density of states (LDOS) [73, 74] or the Purcell effect. In a cavity with a mode volume of V , a refractive index n and a quality factor Q the density of optical modes can vastly exceed the free space value by a so-called Purcell-factor

$$P = \frac{4}{4\pi^2} \left(\frac{\lambda}{n}\right)^3 \frac{Q}{V} . \quad (2.14)$$

Microcavities such as distributed Bragg reflector (DBR) arrangements in vertical pillar structures or whispering-gallery mode resonators generally have a high Q , but also a relatively high mode volume. Plasmonic 'cavities', on the other hand, have rather poor quality factors due to Drude-damping in the electron gas [75]. However, they can have extremely small mode volumes yielding also reasonable Purcell factors, as can be seen from the last kernel in Eq. 2.14. The strength of plasmonic antennas is that optical fields can be concentrated into very small subwavelength volumes. This near-field effect can overcome the problem of light-matter coupling when focusing a resonant laser beam onto a quantum dot which is only 1/10 the size of the diffraction-limited focal spot [76]. Even more fascinating applications require the controlled interaction of many quantum systems in a network. Recent publications envision the entanglement of quantum dots by means of plasmonic waveguides [24] or the use of quantum dots as optical transistors [25].

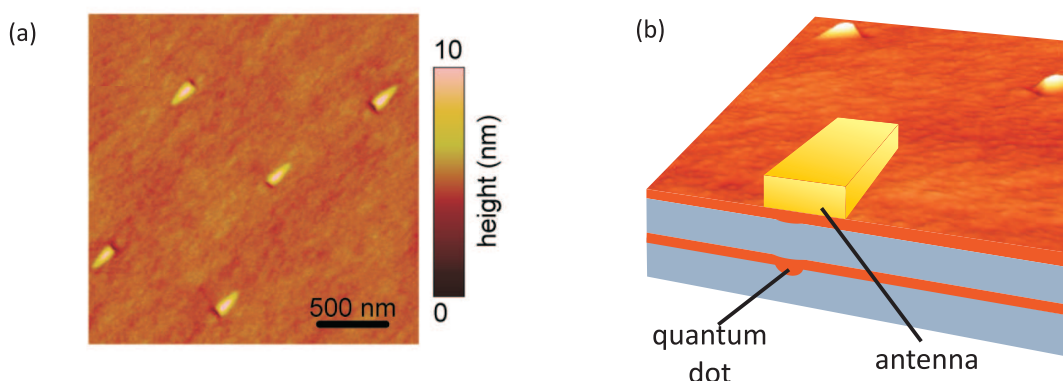


Figure 2.6: AFM image of the sample surface shows characteristic elevations next to elliptical depressions on top of every near-surface QD (a). Au antennas can be fabricated directly on top of QDs using electron-beam lithography (b). Reproduced after reference [22]

When we want to use plasmonic nanoantennas in order to enhance light-matter coupling in our GaAs QDs we have to fabricate a sample in which the dot layer is close to the surface so that they are in range of an evanescent plasmon mode [22]. Figure 2.6(a) shows an atomic force microscopy (AFM) scan of a sample where the QDs sit only 10 nm underneath the surface. For these samples, nanoholes were created by arsenic debt epitaxy [77] and then filled with GaAs as described in the section 2.2. One can identify a characteristic distortion of the crystal surface consisting of an elongated elevation and a depression on top of each QD. As these surface features can be localized by a scanning-electron microscope (SEM) just as well as on this AFM image, we have the possibility to position gold antennas at defined positions with respect to the dot using electron-beam lithography (EBL). A schematic picture of an antenna-emitter pair is given on Fig. 2.6(b).

The accuracy of this method is demonstrated quite impressively on transmission-electron microscopy (TEM) images of vertical cuts through the structure. The sample was cut by focused ion beam (FIB) milling and Fig. 2.7 shows the resulting images in darkfield (a) and brightfield geometry (b). The brightfield image shows the contrast between gold and semiconductor really well, whereas the darkfield brings out the contrast between the QD and the AlGaAs barriers.

Once the coupling between the dot and the antenna is established and the linear properties are understood in this system, ultrafast experiments can shed light on the coherent properties of the combined system. Open questions are the effect of the antenna on dephasing channels and dipolemoments for optical transitions in the dot. Also, limits of selective state-preparation in the hybridized system can be investigated.

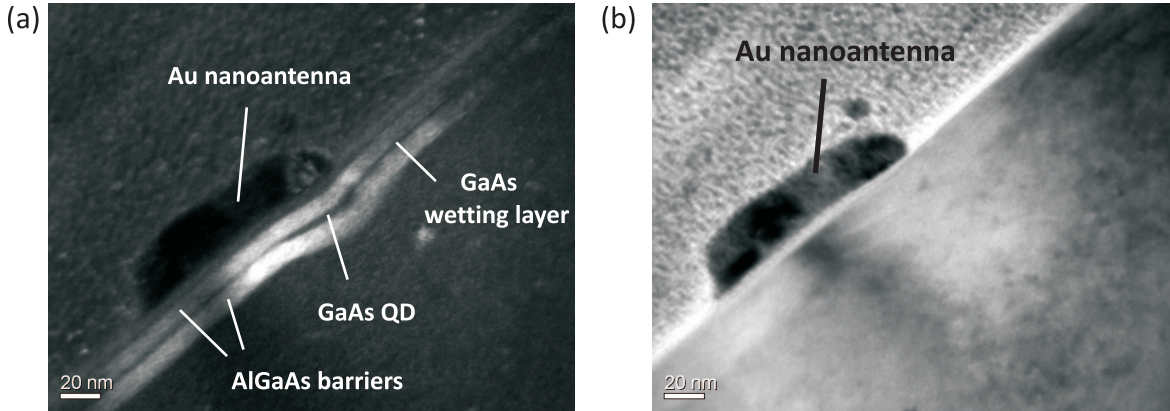


Figure 2.7: Au nanoantennas are precisely positioned on top of surface-near GaAs QDs. The QD and the AlGaAs barrier layers are very well visible on a darkfield TEM image of a vertical FIB-cut through the sample structure (a). The brightfield image of the corresponding region on the sample is shown on (b). Images are a courtesy of Klas Lindfors and Markus Pfeiffer.

2.4.2 Quantum gates in single quantum dots

The basic carrier of quantum information is called quantum-bit or qubit. A classical bit is either 1 or 0, corresponding to two well defined voltage levels. A qubit is a bipartite quantum system like a two-level system (e.g. a spin-1/2 system) with a lower state $|0\rangle$ and an upper state $|1\rangle$. The system can not only assume these pure states but also all possible normalized superposition states $|\psi\rangle = a|0\rangle + b|1\rangle$. $|\psi\rangle$ does not only include states of mixed population, but also the phase between the two states is well defined. A qubit state is therefore a coherent superposition of two quantum mechanical state vectors.

Qubits can be realized in a number of physical systems [78] including charge and magnetic flux qubits in superconducting Josephson junctions [79, 80], neutral atoms [81], spins and charge states in QDs [82, 83]. Here, we want to discuss qubits formed from a coherent superposition of exciton states in self-assembled QDs [84]. Quantum gates [6, 78] can be constructed from several interacting qubits such as in a quantum dot molecule [85]. A pair of qubits has the four boolean states $|00\rangle$, $|01\rangle$, $|10\rangle$ and $|11\rangle$ and it can assume all possible normalized superposition states.

Li et al. could already demonstrate a controlled rotation (CROT) gate in a single QD [86] by an all-optical control scheme. When one only considers up to two electron-hole pairs which are excited in a single dot we can write down a level system such as depicted on Fig. 2.8(a). We can identify the above mentioned two-qubit states in this system as the crystal ground state (empty dot $|00\rangle$), the two fine-structure split orthogonal single excitons ($|10\rangle$, $|01\rangle$) and the biexciton state that is lowered in energy due to

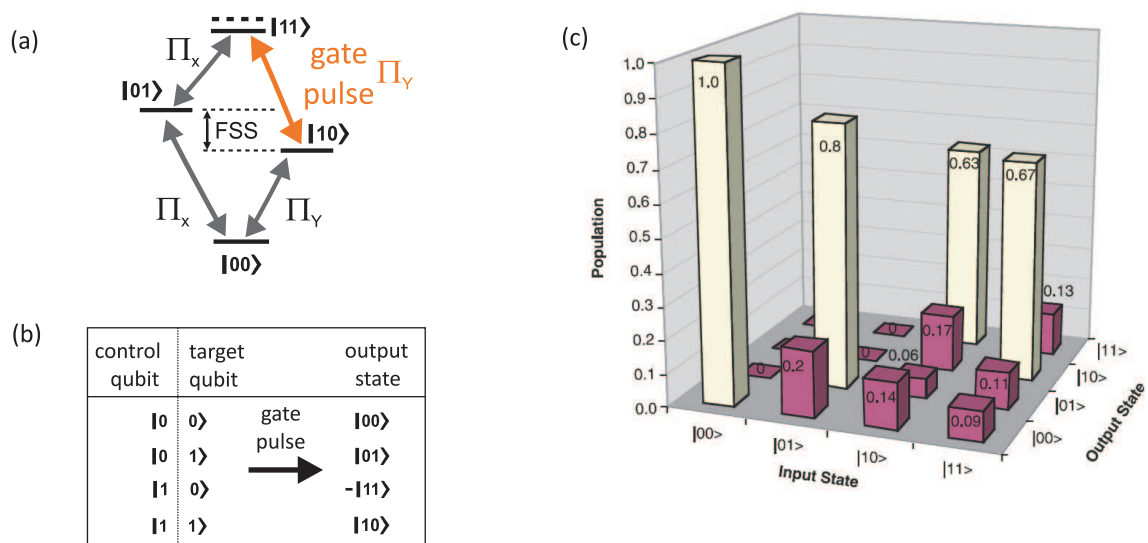


Figure 2.8: Realization of a CROT-gate in a single QD. Coherent manipulations of the quantum mechanical diamond system between the groundstate and the biexciton are used to realize a CROT-gate in a single QD. Transitions can be discriminated by their photon energy and their polarization state (a). When the control qubit is set the gate pulse, which is resonant to the $|10\rangle \rightarrow |11\rangle$ transition, flips the target qubit (b). Experimentally this ideal situation was reached by Li *et al.* with a fidelity of 0.7 (c). Reproduced after reference [86].

Coulomb interaction between the carriers ($|11\rangle$). This means that we have a bipartite system with two states of the exciton which can either be populated (1) or unpopulated (0). The Coulomb-interaction and the resulting redshift for the biexciton transition is exploited as a coupling mechanism between two excitons in the dot. The idea for this conditional quantum gate is, that the biexciton transition is only possible if there is already one single exciton in the dot. In other words, one can only flip the target qubit (second qubit) with a resonant optical gate pulse when the control qubit is set (first qubit). Here, the gate pulse is a π -pulse resonant to the $|10\rangle \rightarrow |11\rangle$ -transition and it only drives this transition if either state $|10\rangle$ or $|11\rangle$ are populated, i.e., when the control qubit is set. When the system is in either the groundstate or the other exciton state ($|01\rangle$) the control qubit is not set and the gate pulse has no effect on the system. The gate operation as discussed above is summarized on Fig. 2.8(b).

The experimental realization of the gate principle was tested by performing the complete quantum state tomography of the system [87]. The outcome of this series of measurements is shown on Fig. 2.8(c). Here, the system is prepared in a certain input state. Then, the gate pulse is applied and the population in all four states is determined by a differential transmission pump-probe experiment. The experimental data indicates, that a CROT-gate can be realized in just one single quantum dot when the properties of the quantum mechanical diamond system are exploited in an optical experiment. All

2 Semiconductor quantum dots

four transitions can be addressed individually as both exciton branches have orthogonal linear polarizations. Ground state to exciton transitions have a different transition frequency from exciton to biexciton transitions due to Coulomb interaction. In other words, by choosing the right frequency and the right polarization for optical pulses interacting with the QD one can achieve full control of the system.

3 Transient differential reflectivity spectroscopy of single quantum dots

We present an ultrafast, reflective pump-probe technique for coherent spectroscopy of single semiconductor quantum dots (QDs). Using far-field microscopic techniques only we are able to address single QDs. Our technique is sensitive to pump induced changes in absorption of the sample. As we record the signal in reflection we can apply this method to heavily absorbing samples and to non-emitting (dark) transitions with no further demands on sample design and preparation except for optical access. Standard photoluminescence measurements are performed in order to locate and characterize single QDs. Ultrafast transients can be recorded with a time resolution that is only limited by the duration of the employed laser pulses (150 fs). The spectral resolution is given by our grating spectrometer with approximately 100 μeV at 720 nm. The signal is the spectral interferogram between the backscattering from the QD and the probe light that is reflected from the sample's surface. In this way we exploit a built-in homodyne detection scheme in order to make the weak backscattering measurable. We detect differential reflectivity signals on the order of 10^{-5} with a signal-to-noise ratio of about 10.

3.1 Overview

Our aim is to investigate the coherent light-matter interaction between ultrafast optical pulses and localized excitons in QDs. Coherent effects such as four-wave mixing (FWM) and Rabi-flopping occur when the duration of the exciting pulses are shorter than the dephasing time of the matter system [88]. The excitation is always given by an ultrafast resonant optical pulse in these experiments. The detection of the change that the excitation has caused in the system can be implemented in numerous ways. Before introducing our experimental approach, we want to discuss several selected techniques from the large body of literature in the field of coherent spectroscopy of QDs.

Coherent experiments have been carried out in single InGaAs QDs by measuring their PL emission [89]. In these experiments the first excited exciton state (p-shell state) is driven resonantly by ultrafast pulses. The excited state rapidly decays non-radiatively into the exciton ground state (s-shell state, ~ 10 ps) which in turn radiatively decays into the exciton ground state (~ 1 ns). The p-shell state population is monitored by counting the photons that are spontaneously emitted when the s-shell exciton decays back to the crystal ground state. The advantage of this technique is that fluorescence can in principle always be measured background free, by means of spectral filtering. On the other hand, one has no access to the complete dynamics of the system, as one basically has to wait for the photons to be naturally emitted by the QD. Streak-cameras and time-correlated single photon counting are methods for extracting transient information about the emission of the PL photons.

A very elegant way of reading out the charge-state of a QD is the photocurrent method which is applied in the group of Artur Zrenner. Here, InGaAs QDs are embedded into an n-i Schottky diode forming a QD photodiode [90]. After resonant excitation of the neutral s-shell exciton the charge carriers tunnel out of the dot due to an applied bias voltage. The tunneling-current is dependent on the charge state of the dot and thus monitors its exciton population. This method is remarkably robust and distinguishes itself by high signal-to-noise ratios [91].

In the group of Christoph Lienau a near-field scanning optical microscope has been used in order to concentrate the field of pump and probe pulses better at the position of naturally occurring interface GaAs QDs. Light has been guided to the QD by an etched optical near-field fiber probe which also collected the reflection from the sample again. Using this method, huge transition dipole moments in large interface QDs [92], the optical Stark-effect [93], perturbed free induction decay [94] and population transfer in quantum dot molecules (QDMs) [95] could be demonstrated.

Another example is a transient transmission experiment to read out the QD state after manipulation with optical or plasmonic pulses [96–98]. In such an experiment, the transmission of a probe pulse is modified by the absorption of the quantum dot. This snap

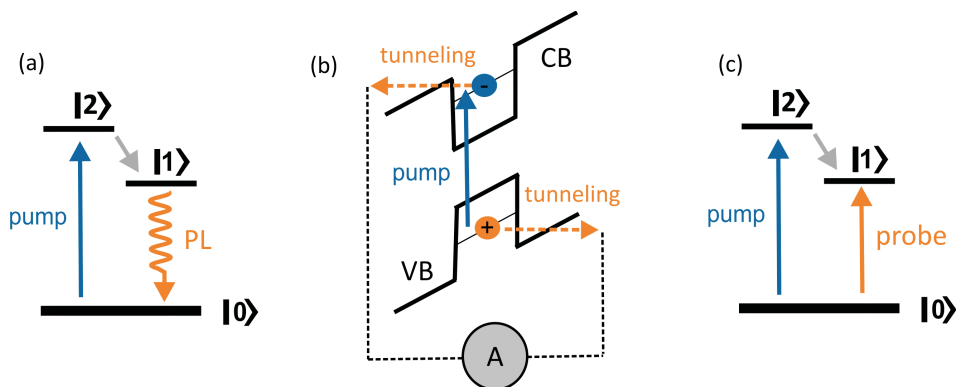


Figure 3.1: (a) Pump pulses populate excited exciton states $|2\rangle$ which relax nonradiatively into the ground state $|1\rangle$. The PL of the exciton is subsequently detected as a measure for the population in state $|2\rangle$ [89]. (b) The exciton can be pumped resonantly when the population is measured via a tunneling current in a single QD photodiode. The excited carriers may tunnel out of the QD due to the tilted potential in the diode [90]. (c) In two-color pump-probe experiments the excitation is realized like in the case (a). The upper state population, however, is detected by differential transmission or reflection of a probe pulse resonant to the ground-state transition $|1\rangle \rightarrow |0\rangle$ [98].

shot of the absorption spectrum gives information on the state in which the dot was left by the previous pump pulse. This experiment requires that the probe pulse is transmitted through the sample, which is not the case if the structure design requires, e.g., a Bragg mirror behind the quantum dot to increase the photon collection efficiency [99]. Another example of excluding design are nanoapertures: in many cases the QD is placed behind a metallic nanoaperture fabricated on the sample surface. The aperture increases the signal-to-noise ratio for the transmission experiment, as the light beam squeezed through the nanohole can be more efficiently blocked by the limited absorption cross section of the quantum dot. On the other hand, these apertures make plasmonic structures on the sample surface impossible.

In this chapter we demonstrate a technique that allows to gain ultrafast spectroscopic information of single QDs without further restrictions to the structure design. We only need far-field optical access to the QD and the reflection of a nearby sample surface. We chose a reflective pump-probe technique as it offers many advantages. First of all, it is fully time-resolved. That means that we are only limited by the duration of our probe pulses in contrast to techniques relying on PL. Secondly, we detect differential reflectivity spectra, which enables us to probe all transitions that fall into the spectral range of the probe pulses, simultaneously. This parallel probing of several transitions was exploited for studying Raman coherence beats between the two fine-structure split neutral exciton transitions in a single GaAs QD (chapter 6) and in investigating the field tuning of lateral InGaAs QDMs (chapter 7). Finally the technique is straight-forward in principle, as it does not require any near-field probes or nanoapertures for signal en-

hancement. This last feature becomes important when we want to apply our method to more complicated structures such as QDs coupled to plasmonic near-field antennas [22] or field-tunable lateral QDMs [100].

Our reflective pump-probe technique is introduced in this chapter and its key features are presented. The formation of the spectral signature of the QDs in the pump-probe spectra will be discussed in great detail. At the end a typical resonant pump-probe experiment will be presented. It shows relative reflectivity spectra as a function of pump-probe delay. This data set captures the decay of a neutral exciton in a single GaAs QD. For negative delay times perturbed free induction decay, a common phenomenon in pump-probe experiments, can be observed.

3.2 Experimental setup

This section gives a description of the experiment in greater detail. The different stages of the experiment will be introduced and their purpose and characteristics will be presented. The setup is divided into three main parts: The laser system (section 3.2.1), the pulse preparation stage (section 3.2.2) and the microscope including detection (section 3.2.3). A simplified diagram of the experimental setup is displayed on Fig. 3.2. Pulses from a commercially available Ti:Sapphire oscillator with a duration of about 150 fs are split up into two beams in order to create pairs of pump- and probe pulses. These two pulse trains undergo spatial filtering in a pulse shaper (PS) and modulation by acousto optic modulators (AOMs). By means of the PS, subspectra can be shaped out of the approximately 8 nm broad laser spectrum. In this way we have the possibility to interrogate the system at an energy that is close to, but different from the excitation energy. The modulation plays a crucial part in our detection scheme which is similar to lock-in detection and which will be described in section 3.3. The pump pulse is delayed by a mechanical stage with respect to the probe pulses, so that delay times can be selected very accurately by a stepper motor. At this point we have two pulses which can be spectrally shaped and delayed with respect to each other in order to excite and probe QD samples. The two beams are now recombined again and coupled into a laser-scanning confocal microscope. The beams are focused down to a spot size which is about the size of its wavelength and positioned onto a single QD. The reflection of the probe pulses is coupled into a grating spectrometer in order to record pump-probe spectra. Differential reflectivity spectra are basically the difference between the probe reflection with the pump switched on (signal spectrum) and spectra where the pump is switched off (reference spectra). We can also couple a cw laser with a wavelength of 532 nm into the microscope in order to record the PL emitted by the QD. This can be done using an avalanche photo diode (APD) for spatial PL maps or using the grating spectrometer for PL spectra. With this experimental setup we are capable to address single QDs, study their emission and probing their ultrafast transient response to an

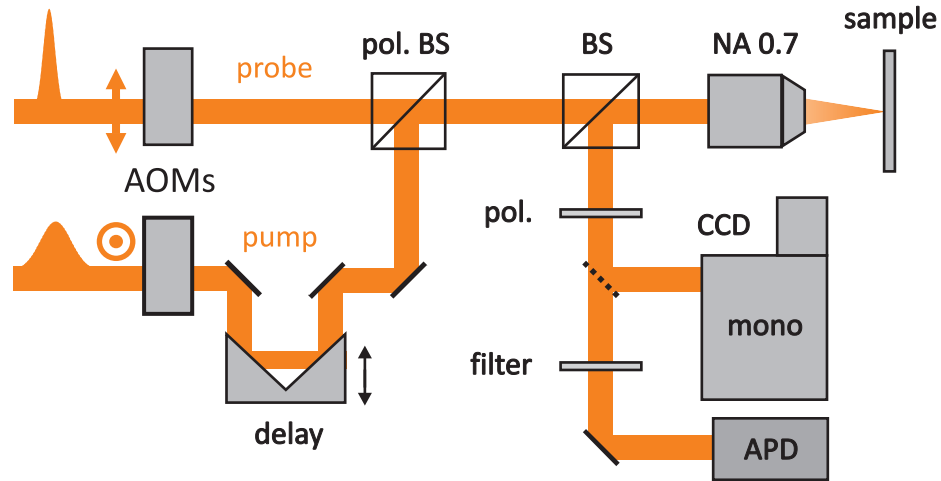


Figure 3.2: A laser-scanning confocal microscope is employed in order to address single QDs in a cryostat. Probe pulses with a duration of 150 fs are reflected off the QD sample with a delay Δt after the orthogonal polarized pump pulses. Spectra of the reflected probe pulses are recorded by a spectrometer with a spectral resolution of $100 \mu\text{eV}$. $\Delta R/R$ spectra are obtained by subtracting reference frames (pump off) from signal frames (pump on).

excitation pulse.

3.2.1 Laser system

The main light source for our pump-probe experiments is a Kerr-lens mode-locked Ti:Sapphire femtosecond laser (*Coherent, Mira*) with a repetition rate of 76 MHz. Due to the broad gain profile of the active medium it is tunable in the range between 700 nm and 1000 nm. The oscillator is optically pumped by a diode pumped, frequency-doubled Nd : YVO₄ cw-laser with 10 W at 532 nm (*Coherent, Verdi V 10*). The output of the oscillator is a pulse train with pulse durations of about 150 fs and 8 nm spectral width. The output power rises from about 0.5 W at the extremes to well above 1 W at the center of the tunable range, values depending on the quality of the cavity alignment. For some experiments presented in chapter 5 an optical parametric oscillator (OPO, *APE, OPO PP Auto*) was used in order to provide probe pulses resonant to the neutral exciton transition in GaAs QDs around 720 nm or 1.74 eV. The idea was to pump the GaAs substrate just slightly above the bandgap of 1.43 eV and probe the QD resonantly. For this experiment the pump and probe energies are too far apart to shape them out of the relatively narrow spectrum of the Ti:Sapphire oscillator. Instead, the *Mira* was tuned to 790 nm and its output split into two beams. One beam was directly used to pump the semiconductor sample and the other beam was used to pump the OPO. The OPO has a ring cavity with two focal spots. In the first one a periodically poled

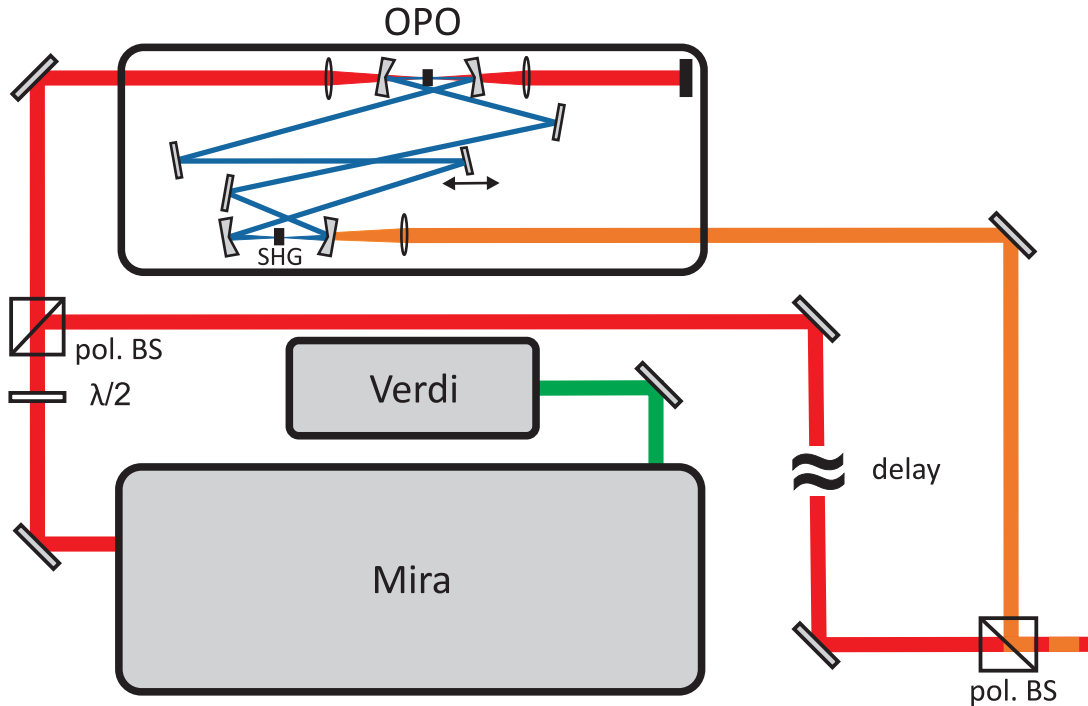


Figure 3.3: All experiments were carried out with a Ti:Sapphire laser producing pulses of 150 fs duration at a repetition rate of 76 MHz in the spectral range from 700 nm to 1000 nm. Additionally, an optical parametric amplifier was used for two-color pump probe spectroscopy (see chapter 5). The OPO has a ring cavity with a periodically poled lithium-niobate crystal for the parametric process and a lithium borate crystal for doubling of the signal wave frequency in its two focal points. The output is tunable from 505 nm until 740 nm using a fixed pump wavelength of 780 nm.

lithium niobate crystal (PPLN, LiNbO_3) is placed and signal and idler waves are created from the pump wave. In the parametric process the sum of energies and momenta must be conserved, which leads to phase matching criteria for signal and idler waves. A lithium triborate crystal (LBO, LiB_3O_5) is positioned in the second focal spot of the OPO cavity. It doubles the frequency of the signal wave by second-harmonic generation (SHG) and so converts the infrared photons into visible light. The periodically poled nonlinear crystal ensures a high conversion efficiency for a broad output spectral region (for details on OPOs see [101, 102]). The resonance criterion for the frequency doubled signal wave is the cavity round trip time in the OPO. One of the cavity mirrors is mounted on a piezo-electric stage so that the OPO round trip time can be matched to the repetition rate of the pump pulses for the desired output wavelength. The output wavelength of the OPO can thus be tuned just changing the cavity length.

Before the two beams were recombined again in order to be coupled into the experiment the *Mira* output had to be delayed in order to compensate for the OPO's cavity

length. This could ensure the coarse temporal overlap of both pulse trains at the site of the QD sample.

3.2.2 Pulse preparation

The middle section of the experiment has the purpose of transforming the ingoing pulse train from the laser source into a pump and a probe train which have a controllable time delay with respect to each other and where the spectra are individually shaped out of the Ti:Sapphire laser spectrum. A sketch of this part of the setup can be seen of Fig. 3.4. A combination of a half wave plate and a polarizing beam splitter cube (PBS 1) is used in order to produce two orthogonal linearly polarized beams with a power ratio that can be selected freely. The probe beam is s-polarized and the pump beam is p-polarized. In each of the two arms the light passes a diffractive amplitude pulse shaper (PS 1 and 2) and an acousto optic modulator (AOM 1 and 2). As the holographic gratings that were used in the pulse shapers (1800 grooves per mm, *Thorlabs, GH25-18V*) have a better diffraction efficiency for p-polarized light ($\sim 65\%$ at 720 nm) the polarization direction was rotated by means of a half wave plate before passing through the pulse shaper and rotated back to s-polarization again before recombining the beams again. The mechanical delay stage is placed into the pump arm so that the probe beam has a constant pointing at all times and does not wander due to a not optimal alignment of the delay stage's retro reflector.

A diagram of our pulseshapers can be seen on Fig. 3.4(a). A collimated beam is split up into its frequency components by a first diffractive grating and the bundle of monochromatic beams originating from the grating is collimated by by a lens placed one focal length, f , away from the grating. The different frequency components travel now parallel to each other to a mirror placed at a distance f from the lens. Right at the mirror (in the Fourier plane) where the beams are focused an aperture can be placed in order to block unwanted frequency components. The original beam is reassembled while traveling back through the lens and over the grating. The spectrum of the outgoing beam is missing exactly those frequencies that were blocked by the aperture in the Fourier plane.

Besides acting as a frequency filter the pulse shaper can also compensate for linear chirp or second order group velocity dispersion (GVD) of the laser pulses. GVD can in simple terms be understood as the respective delay between different frequencies comprising the optical pulse. A pulse where the higher frequencies are leading is called down-chirped, whereas we call the pulse having an up-chirp when the higher frequencies are being at the trailing end of the pulse. When a pulse travels through a dispersive medium it accumulates chirp, as different frequencies travel at different velocities. One can imagine the pulse made up from subpulses that have different group velocities depending on their respective central frequencies. In a normal dispersive medium such as BK7 glass the red subpulses will travel faster than the blue ones leading to an up-chirped pulse that is

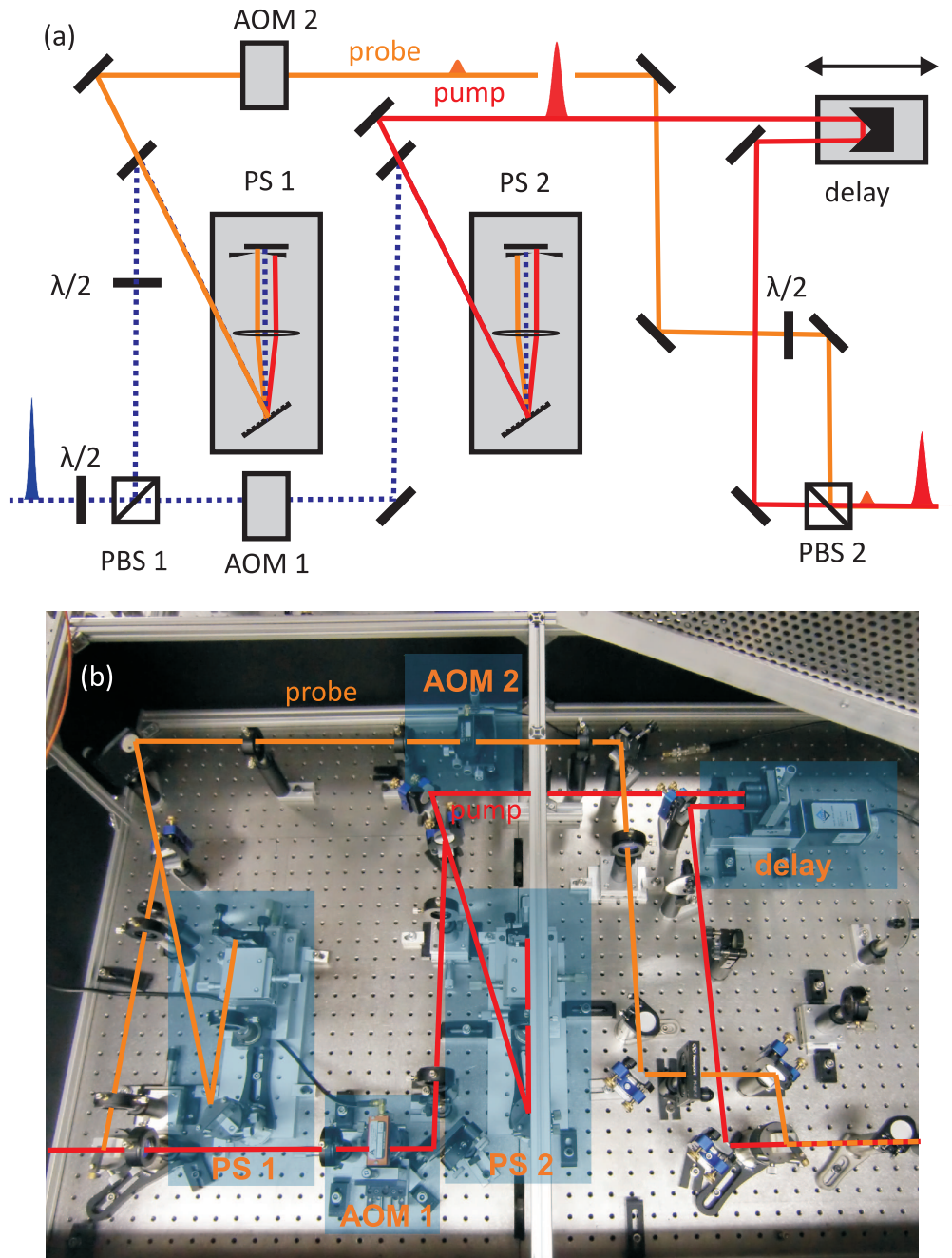


Figure 3.4: Light preparation: (a) Pump and probe pulses are shaped out of one fs-pulse using two pulse shapers (PS). Both pulses are modulated by AOMs for differential detection and the pump pulses are delayed with respect to the probe pulses before they are recombined. (b) Photograph.

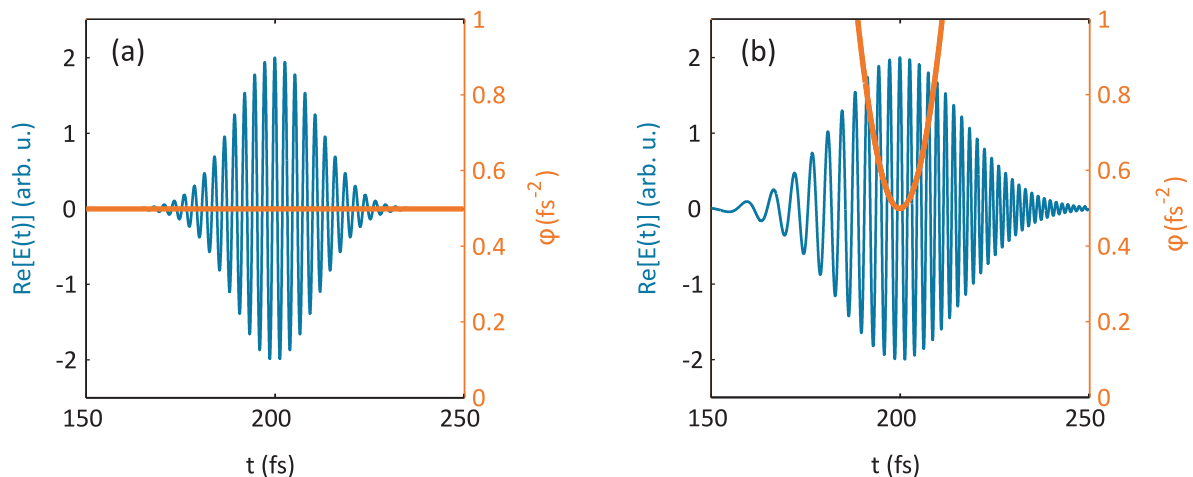


Figure 3.5: (a) Transform limited pulse with a flat phase. (b) Up-chirped pulse with a quadratic phase.

broadened in time while maintaining its power spectrum. In our setup the pulse shaper must be aligned correctly so that it compensates for the GVD that the glass optics are introducing to our pulses. The time-dependent electric field $\mathbf{E}(t)$ of a laser pulse with an amplitude \mathbf{E}_0 and a full width at half maximum (FWHM) duration of the intensity profile, Δ_t , can be described mathematically in the following way:

$$\mathbf{E}(t) = \mathbf{E}_0 \cdot e^{-2\ln(2)\left(\frac{t-t_0}{\Delta_t}\right)^2} \cdot e^{i(\omega_0 t + \phi_0 + \phi(t))} \quad (3.1)$$

Here the phase factor following the Gaussian envelope contains a plane wave oscillating with the carrier frequency ω_0 , the carrier to envelope phase ϕ_0 and a phase $\phi(t) = \phi_1 t + \phi_2 t^2 + \dots$ describing the chirp of the pulse. The linear term is just a shift of the carrier frequency, whereas the quadratic phase term is called group velocity dispersion or GVD. Fig. 3.5 shows an example of a transform limited pulse (a) where all spectral components are perfectly overlapped in time, meaning that the phase is flat in time, compared to an upchirped pulse (b) that was broadened when passing a normal dispersive medium such as glass. In this case the phase is parabolic in time (see Eqn. 3.1). The basic outline of a grating PS is shown on Fig. 3.6. The ingoing beam is collimated and might have some initial GVD. A diffractive grating separates the frequencies contained in the pulse spatially. As the frequency components propagate after the grating they accumulate angular dispersion, meaning that different wavelengths acquire different phases or have different optical path lengths as they go through the PS. The beam bundle is collimated by a lens which focuses each beam at the Fourier plane where a spatial filter can be placed in order to block unwanted frequencies. Then the pulse is recreated by a second combination of a lens and a grating. The distance of the grating to the lens determines the amount and the sign of GVD that is introduced by the PS. The displayed 4f-configuration is GVD neutral. In case of a larger lens-grating-distance than f we are introducing positive GVD and negative GVD for a smaller one. Depending on the chirp of the input pulse the PS can act as a pulse stretcher, a pulse

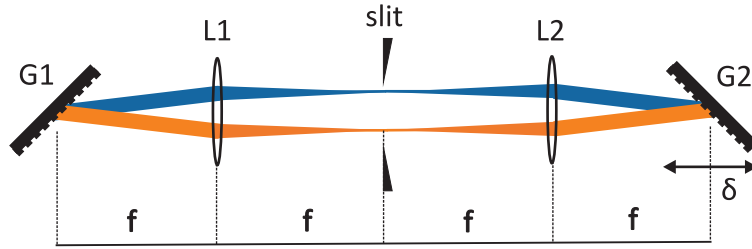


Figure 3.6: Basic setup of a pulse shaper. A diffractive grating separates the frequencies contained in the pulse spatially. As the frequency components propagate after the grating they accumulate angular dispersion. The beam bundle is collimated by a lens which focuses each beam at the Fourier plane where a spatial filter can be placed in order to block unwanted frequencies. Then the pulse is recreated by a second combination a lens and a grating. The distance of the grating to the lens ($f+\delta$) determines the amount and the sign of GVD that is introduced by the PS. The displayed 4f-configuration is GVD neutral.

compressor or being GVD neutral. This very simple optical setup can be combined with more sophisticated spatial light modulators such as LCD arrays in order to realize more complicated pulse forms. It is even possible to have full control over the time-dependent electric field both in frequency and polarization with the latest generation of pulse shapers [103, 104]. The pulse shapers that were used in our experiment are rather simple compared to modern ones using programmable LCD arrays. Fig. 3.7(a) shows a photograph of one of our PSs. We realized a folded geometry where a mirror is placed right in the Fourier plane in order to reduce the footprint of our design, so that there is only one grating and one lens ($f = 100$ mm). Just in front of the mirror surface two razor blades are mounted on linear stages forming a slit of variable position and width. The lens is mounted on a rotation stage in order to compensate for third order dispersion [105]. Fig. 3.7(b) shows the spectrum of the *Mira* pulses on the razor blades in the Fourier plane and Fig. 3.7(c) shows spectra of pump and probe pulses (red) that were shaped out of the *Mira* spectrum (blue). The obtained subspectra have clearly a square shape when only using a slit as spatial filter mask. For proper alignment of the setup each pulse shaper is first optimized independently. Before the pulses are coupled into the microscope they are focused into a BBO (beta-bariumborat) crystal for SHG (see Fig. 3.9). The resulting ultraviolet photons are detected by a PMT after the fundamental frequency is suppressed by a filter (*Schott glass BG7*). Due to the nonlinearity of the SHG process the shortest infrared pulses will create the most ultraviolet light. So each PS is optimized on maximum SHG for the respective pulsetrain by aligning the distance between the lens and the grating and the focusing on the mirror. After the optimum is obtained the delay stage is scanned while monitoring the SHG by the PMT and an intensity autocorrelation function is recorded. Both pulses should ideally be identical. As they are modulated at different carrier frequencies due to the two different AOMs and traveling on different paths passing two separate PSs, we should state, that technically we are measuring a cross-correlation of two different pulses. In this case, however, the

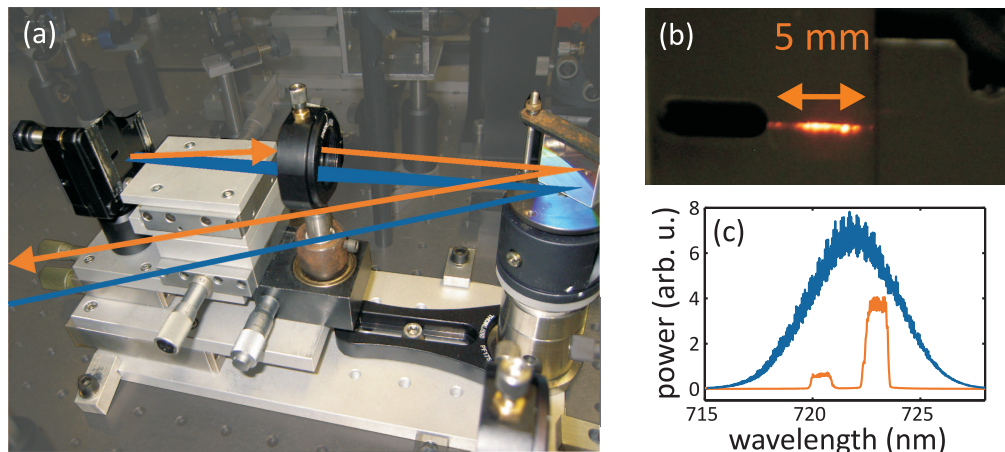


Figure 3.7: (a) Photograph of our PS. The folded geometry only uses one lens and grating. Razor blades serve as spatial filter in order to shape out subspectra in the Fourier plane. (b) *Mira* pulses on the razor blades in the Fourier plane. (c) Spectra of pump and probe pulses (red) that were shaped out of the *Mira* spectrum (blue).

result looks like a nonlinear autocorrelation function (ACF), as the differences between the two pulses are negligible. From the nonlinear ACF the zero path difference position and the duration of the pulses can be obtained and it can be written as

$$I_{ACF}(\tau) \propto \int_{-\infty}^{\infty} |(E(t) + E(t + \tau))|^2 dt \quad . \quad (3.2)$$

For a square spectrum the ACF width corresponds to the width of the temporal intensity profile, whereas for opened slits in the PS, a pulse of Gaussian power spectrum leads to an ACF which is longer than the pulse duration by a factor of $\sqrt{2}$ [106]. It must be noted that we are not able to measure fringe-resolved interferometric autocorrelations with this setup, as the two AOMs run with different carrier frequencies and the mode-combs of both pulse trains are shifted in frequency by these two acoustical frequencies. One AOM is driven at a frequency of 80 MHz (*Intra Action Corp.*, *AOM 80*) and the other one at 110 MHz (*AA opto-electronic*, *MT110 1.5 IR*). So for the (plus) first order of diffraction at the AOM each diffracted photon gains the energy $\hbar f$ when f is the frequency of the standing acoustic wave in the AOM due to photon-phonon interaction. Therefore we are only able to acquire the envelope of the nonlinear ACF traces.

One AOM is gated open (modulation input is a DC signal), whereas the other one is modulated by a function generator (*Agilent Technologies*, *Function Generator 33220 A*) at 80 kHz. The output voltage of the PMT is fed into a Lock-In amplifier (*Stanford Research Systems*, *SR830 DSP*) which is locked on the function generator's synchronization output. Best results were obtained when the modulated beam was much weaker than the unmodulated one. Fig. 3.8(a) shows two examples for autocorrelations that were measured for two different spectral widths. The signals were normalized to each other but the SNR clearly indicates that the full broader spectrum gives the shorter

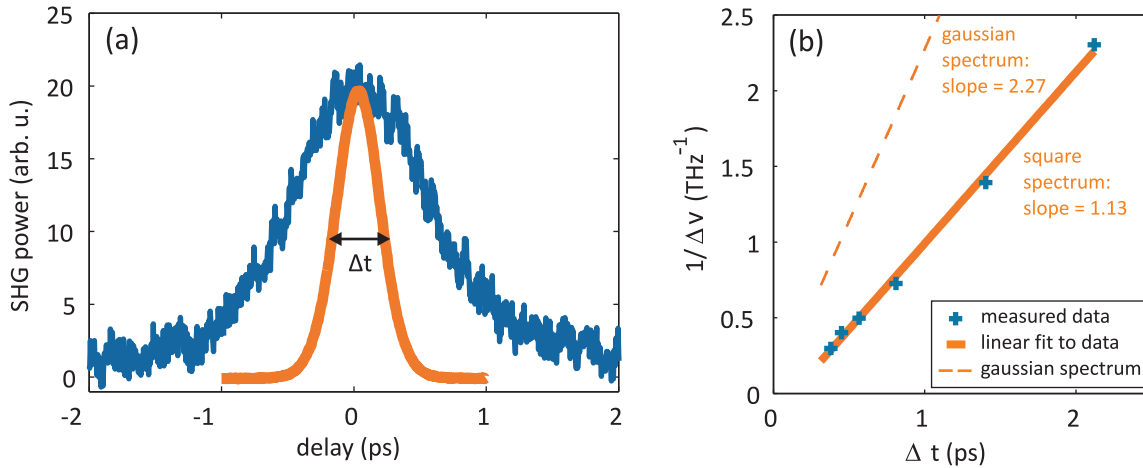


Figure 3.8: (a) Example of two ACF measurements for two different slit width at the PS. (b) Data set of ACFs for different spectral widths of the pump and probe pulses. The data fits to pulses having a square-shaped power spectrum

pulse (red curve). Fig. 3.8(b) shows a complete series of data for different pulse widths. The inverse frequency width $1/\Delta\nu$ is plotted over the ACF duration Δt . One can see from the slope of the fit curve that the data does not behave like for a Gaussian pulse which has a time-bandwidth product of $\Delta\nu \cdot \Delta t = 0.441 = 1/2.27$. It is much closer to a square spectrum with an inverse time-bandwidth product of $0.886 = 1/1.13$ [106], as is expected.

3.2.3 Laser-scanning confocal microscope

A schematic diagram and a photograph of the microscope is displayed on Fig. 3.9. First, the excitation beam profile is cleaned by a pinhole before the light is coupled into the microscope by a dichroic beamsplitter (*AHF, 570 DXCR*, 570 nm cut-on wavelength). The beamsplitter reflects 10% of the incident light above the cut-on wavelength, which is still enough for most of our experiments. The advantage here is, that the light that is coming back after interacting with the QD gets transmitted almost completely which enhances greatly the collection efficiency. For experiments where more power was needed the dichroic beamsplitter was replaced by a standard 50/50 beamsplitter (*Thorlabs, BS017*). In order to address single QDs we are focussing the pump and probe beams down to a diffraction-limited spot by a microscope objective with a numerical aperture of 0.7 (*Olympus, LCDPlanFL N*) and a magnification of 50. The relatively small NA is owed to the fact that we are not submerging the microscope in helium but instead only cool the semiconductor sample. We use a He-flow cryostat (*Cryovac, Konti*) to cool the sample down to temperatures of around 10 K. In this case the working distance of the objective must be large enough to accommodate the cryostat window and one millimeter of insulating vacuum between the objective's half sphere lens and the sample

surface. For 1 mm of glass between the sample and the objective the working distance is about 2.3 mm. The PL emission as well as reflected probe light from the sample is collected by the same objective and sent back into the opposite direction, where it passes the dichroic beamsplitter, dielectric filters (*Omega Optics, 3rd Millennium*) and is focused through a pinhole before it reaches the detectors. The confocal pinhole mainly improves the depth resolution of the microscope but also helps in suppressing emission from laterally displaced sources on the sample surface and reduces stray light. We use an ultrasensitive avalanche photodiode (APD, *Micro photon devices, PDM series*) for single photon counting and an imaging grating spectrometer (*Acton, SP500i*) equipped with a back illuminated deep-depletion charge-coupled device camera (CCD, *Princeton Instruments, PIXIS 100*) for recording PL emission spectra as well as pump-probe spectra.

In most setups the cryostat is mounted horizontally on a two-axes stepper motor translation stage in order to accurately scan the sample through the static focus of the microscope. We decided, however, to mount the cryostat in a vertical position on a mechanical three-axes stage allowing for coarse positioning of the sample. We then employ a laser-scanning microscope [107] to scan the focus over the static sample. This technique requires a telecentric lens system and a two-axes scanning mirror (*PI, S-334*) as displayed on Fig. 3.10. The arrangement is again a 4f-arrangement, very similar to the PS. The center of the scanning mirror is positioned in the focal spot of the first lens ($f = 100$ mm) so that the beam after the lens is traveling parallel to the optical axis for every angle the scanning mirror assumes. The second lens is confocally positioned at a distance of $2f$ from the first lens in order to produce a collimated beam, again. The beam is always dissecting the optical axis at a distance f from the second lens, independent of the scanning mirror's position. This is exactly the point where the back focal plane of the microscope objective is placed. In this way the light always passes the objective without clipping and fills the complete aperture. The mirror position now controls the angle under which the beam passes through the objective and thus the lateral position of the focus in the focal plane.

The microscope was calibrated using a grating with a grating constant of $10 \mu\text{m}$. The deflection angles of the beam from the scanning mirror were translated into lateral displacements of the focus on the sample surface both in the horizontal and the vertical direction. Our microscope objective in combination with two lenses with a focal distance of 150 mm and a maximum deflection angle from the scanning mirror of $\pm 2^\circ$ yield a field of view of approximately $150 \times 150 \mu\text{m}^2$. The microscope was modeled by simple ray-tracing and the field of view could be confirmed by this method. A scanned image of the calibration sample can be seen on Fig. 3.11(a). An attenuated beam from the Ti:Sapphire laser at 720 nm was reflected off the grating sample and detected by the APD. The image is the convolution of the object with the point-spread function (PSF) of the microscope and so the apparent steepness of the grooves as seen on the image is a measure for the lateral resolution of our microscope. A line scan over one groove is displayed on Fig. 3.11(b). The data (blue crosses) could be fit with an error function

3 Transient differential reflectivity spectroscopy of single quantum dots

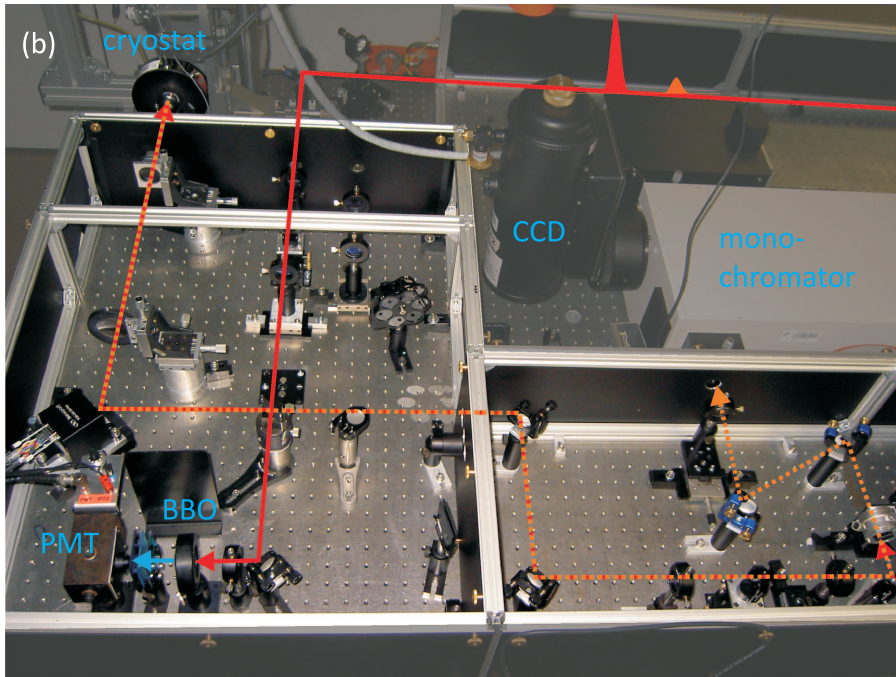
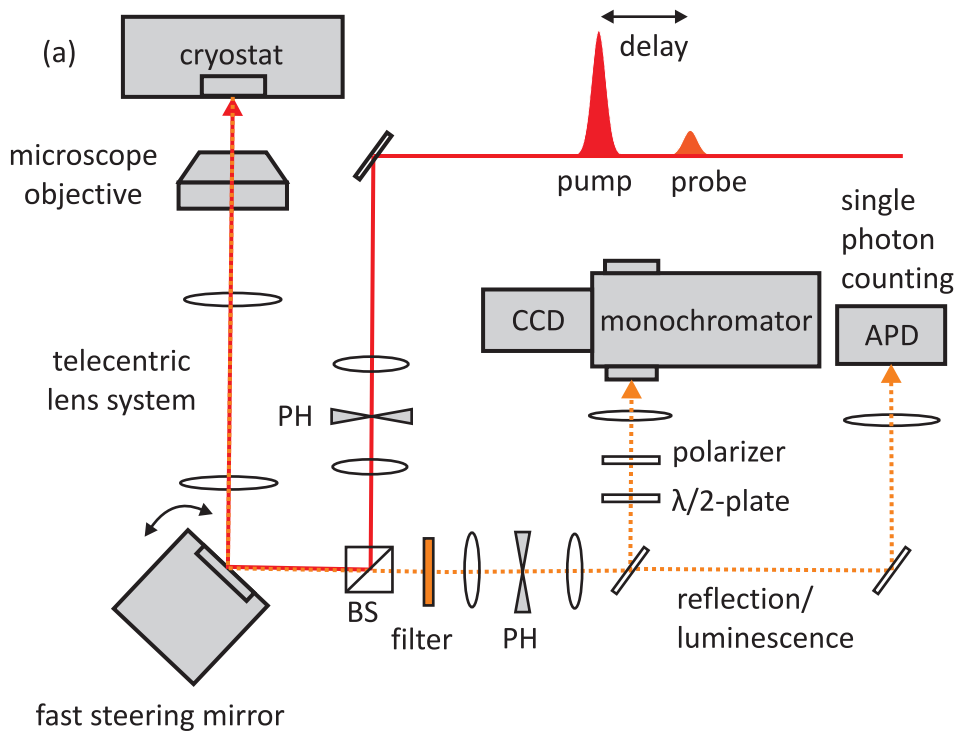


Figure 3.9: (a) Pump and probe pulses are coupled into a laser-scanning confocal microscope in reflection geometry. The reflected light can be detected by an APD, a CCD, or a photodiode, after filtering and dispersion. (b) Photograph.

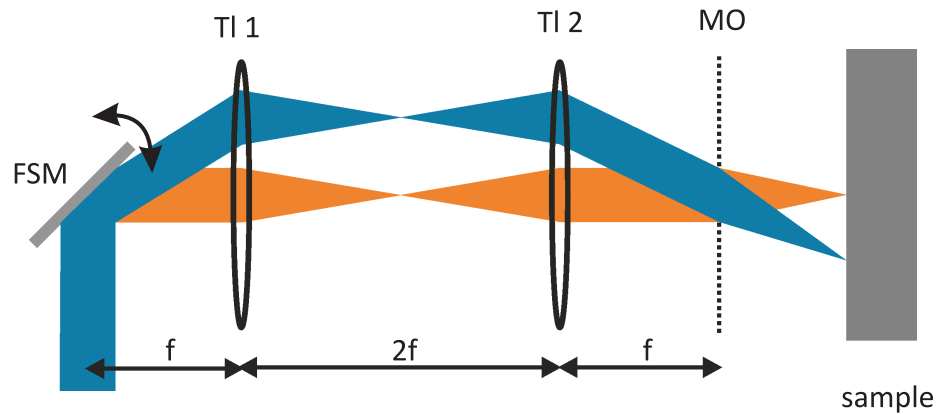


Figure 3.10: A laser-scanning microscope is realized by a fast scanning mirror (FSM), a telecentric lens system (TL1 and TL2) and a microscope objective (MO) in a $4f$ arrangement. The incoupled beam always fills the full aperture of the objective as the focus can be positioned laterally on the sample surface by changing the angle of the scanning mirror.

being the integral over a Gaussian having a FWHM, σ , of 750 nm (red line).

$$I(x) = (f * g)(x) = \int_{-\infty}^{\infty} \frac{I_0}{\sigma\sqrt{\pi}} \exp\left[-\frac{4\ln(2)(x-x')^2}{\sigma^2}\right] \cdot \Theta(x-x') dx' \quad (3.3)$$

Here, $I(x)$ signifies the line scan over one groove along the x -axis, $f(x)$ is the PSF of the microscope and $g(x-x')$ is the step function $\Theta(x-x')$ which models one groove of the calibration grating. This means that we almost completely fill the NA of the microscope objective, as the diffraction limited focal spot diameter for our experimental parameters is 630 nm.

3.3 Signal formation

The key idea (see Fig. 3.12(a)) is that the absorption by a dipole can be understood as the interference of the optical wave scattered at the dipole in forward direction with that passing the dipole unperturbed, known as the optical theorem [108]. The scattered wave itself is too weak to be detected, however, the phase-stable interference with the exciting wave leads to a measurable signal [109]. If we make the scattered wave interfere with the part of the exciting wave that is reflected at the sample surface in the backward direction, then also in this direction we are able to measure an absorption signal. This fundamental effect was used to detect single molecule absorption [110], the steady-state absorption of single quantum dots [111] and also the transient absorption of single quantum dots using

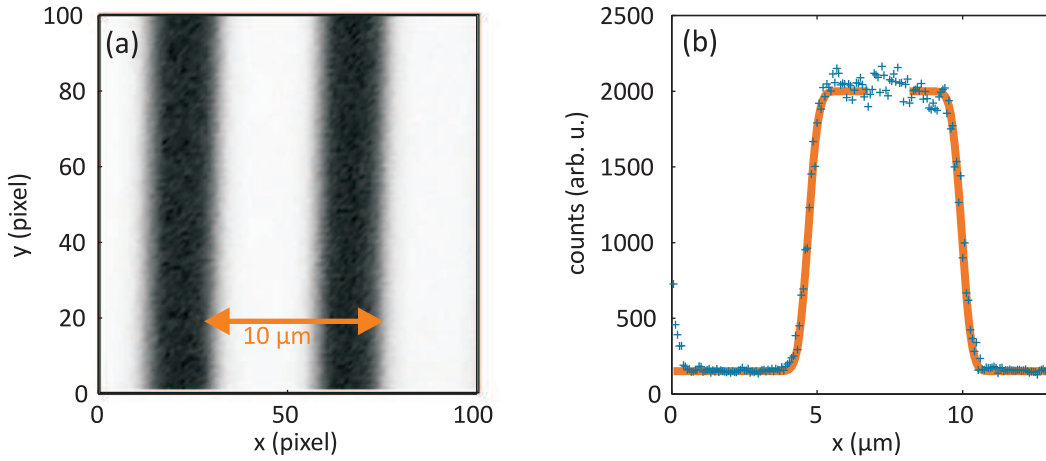


Figure 3.11: (a) Confocal image of the grating used for calibration of the microscope. (b) The line scan over one groove (blue crosses) fits to a PSF of 750 nm FWHM (red line).

a scanning near-field aperture [92]. The near-field aperture increases the signal-to-noise ratio similar to metallic nanoapertures mentioned in section 3.1. Here, we demonstrate that the ultrafast transient signal of a single quantum dot is measurable even without such a near-field aperture, which simplifies very much the necessary experimental efforts. Both absorption and reflection have their origin in the scattered field E_S of a dipole into a halfspace of solid angle 2π [109] (see Fig. 3.12(a))

$$E_S = \tilde{\alpha}(\omega) E_0 \quad \text{with} \quad \tilde{\alpha}(\omega) = \frac{\alpha_0}{2} \frac{-i\gamma}{\delta + i\gamma} \quad , \quad (3.4)$$

where E_0 is the exciting probe field, α_0 the peak absorption of the dipole, $\delta = \omega - \omega_0$ the probe detuning from the dipole's resonance, and $\gamma \ll \omega_0$ the resonance width. The peak absorption can be written as

$$\alpha_0 = \frac{1}{A} \frac{e^2 f}{\epsilon_0 m_0 n \Gamma} \quad . \quad (3.5)$$

Here A signifies the illuminated area (spot size) which can be approximated by $1.13 \phi_{\text{FWHM}}^2$ with ϕ_{FWHM} being the full width at half maximum of the intensity in the focal point. Furthermore, ϵ_0 is the permittivity of vacuum, e and m_0 are the electron's charge and mass, n is the refractive index of the medium surrounding the QD and Γ and f are the dephasing rate and the oscillator strength of the exciton [109]. For purely radiative decay the absorption can be expressed by

$$\alpha_{sp} = \frac{3}{2\pi} \frac{(\lambda/n)^2}{A} \quad . \quad (3.6)$$

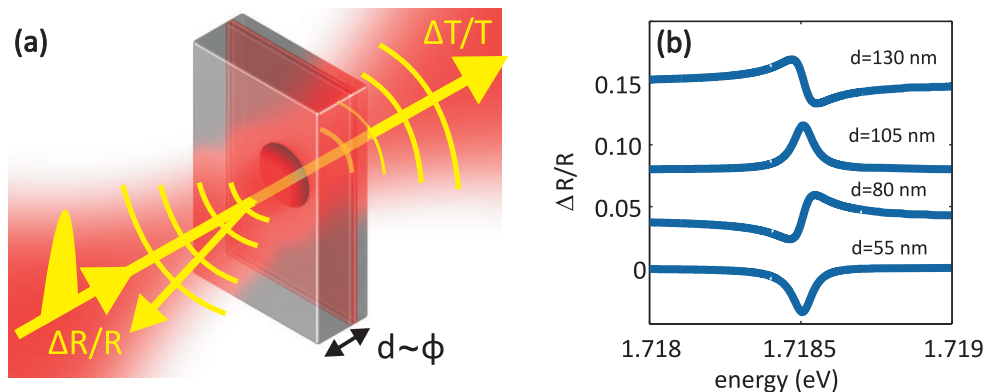


Figure 3.12: (a) The field scattered at the quantum dot interferes with the transmitted as well as with the reflected probe field. It gives rise to transient absorption and reflection features. (b) The phase lag ϕ changes the spectral shape of the transient reflection signal from absorptive to dispersive and back. Line shapes are displayed for four different burial depths of the QD beneath the sample surface.

In this case λ is the resonance wavelength. The purely radiative decay is an ideal case that gives the highest possible absorption signal for the complete absence of nonradiative decay channels. In our case we deal with dots emitting at 720 nm embedded in a GaAs matrix having a refractive index of about 3.45 at low temperatures and our microscope focuses the laser beam down to a spot of 750 nm FWHM. For these parameters α_{sp} assumes a value of 0.033. If we assume an oscillator strength f and a dephasing rate for the exciton transition, we can estimate the value of α_0 . In chapter 4 we determine the dipolemoment to be 18 D which corresponds to an oscillator strength of $f = 6$. We also estimate the dephasing time to be 90 ps at the end of this chapter, so that we can derive a dephasing rate of about $\Gamma = 1.2$ GHz. This value corresponds to a natural linewidth of only $5 \mu\text{eV}$. Using these values the absorption on resonance is $\alpha_0 \approx 0.012$.

The reflectivity of the QD alone can be calculated to be

$$R_{QD} = \left| \frac{E_S}{E_0} \right|^2 = \left(\frac{\alpha_0}{2} \frac{\gamma^2}{\delta^2 + \gamma^2} \right)^2. \quad (3.7)$$

For the above mentioned experimental parameters one can expect a center-to-peak differential reflectivity signal amplitude of $\Delta R/R = 2.7 \cdot 10^{-4}$ from the QD alone. As the spectral resolution of our spectrometer ($100 \mu\text{eV}$) is one to two orders of magnitude too small in order to resolve the natural linewidth of the exciton transition in the QD (several μeV), we can only expect an even weaker signal. For the estimation of $5 \mu\text{eV}$ for the natural linewidth above, we can expect that the signal is washed out and reduced by a factor of roughly 20.

However, it is not the scattered field alone that makes up the transmitted and the reflected signals. We have also to include the transmitted and the reflected fields that

3 Transient differential reflectivity spectroscopy of single quantum dots

did not interact with the QD. The total transmitted and reflected fields are the respective coherent sums with the unperturbed transmitted and reflected probe fields

$$E_T = tE_0 + \tilde{\alpha}(\omega)tE_0 \quad (3.8)$$

$$E_R = rE_0 + \tilde{\alpha}(\omega)e^{i2\phi}t^2E_0 \quad (3.9)$$

where r and t are the Fresnel coefficients for reflection and transmission, respectively, and ϕ is the phase lag the field acquires by traveling from the sample surface to the dipole position. The phase lag ϕ influences the spectral shape of the signal, varying from a absorptive to a dispersive line shape, as shown in Fig. 3.12(b). For a GaAs surface with a reflectivity of about 30%, $|r|$ and $|t|$ are comparable, so that the signal is equally strong in transmission as in reflection. We will therefore use in the following the reflected light to determine the absorption of a single quantum dot.

Taking into account the reflection from the sample surface, the differential reflectivity as a function of the detuning can be written as [109]

$$\Delta R/R \approx \frac{4n}{n^2 - 1} \alpha_0 \frac{\gamma^2}{\delta^2 + \gamma^2} \left(\cos 2\phi - \frac{\delta}{\gamma} \sin 2\phi \right). \quad (3.10)$$

As mentioned earlier, we use AOMs in order to modulate pump and probe pulse trains on a ms timescale. In order to reduce the acquisition time only an area of 400x20 pixels on the CCD directly under the read-out register was illuminated and read out. This means that only 20 rows must be shifted and only 400 pixels must be digitized. The double modulation scheme that we employed to acquire differential reflectivity spectra is sketched on Fig. 3.13. Instead of acquiring a signal frame with pump and the reference frame without a pump pulse, we just displaced the pump pulse train in the reference case. This makes sure that the residual pump light that reaches the CCD chip, in spite of the suppression by polarizing optics, is always the same for signal and reference frames. As the excitations in the sample are short lived compared to the displacement of the pump and probe gating windows, there is no pump-induced signal in a reference frame. The signal frames are consequently acquired with pump and probe gated on at the same time for 0.5 ms and the chip is read out after a dark gating window of 0.5 ms. At this time a TTL trigger pulse is sent to the CCD camera to start the read out process. After an additional short time window (0.05 ms) which allows the charges to be shifted into the read-out register of the CCD chip, the reference frame is acquired. It starts again with the probe pulse train being sent to the sample for 0.5 ms, followed by the pump pulse train window. This pattern is modified for the next two acquisitions so that the probe window is now directly before the trigger. This is done in order to minimize effects from loss of charge in the CCD pixels between exposure and read-out. Now, the gating pattern of the last four acquisitions repeats itself for as long as one wants to integrate. After the measurement is complete one has a dataset of signal and reference frames modulated at 1 kHz and $\Delta R/R$ spectra are obtained by subtracting the sum of the odd

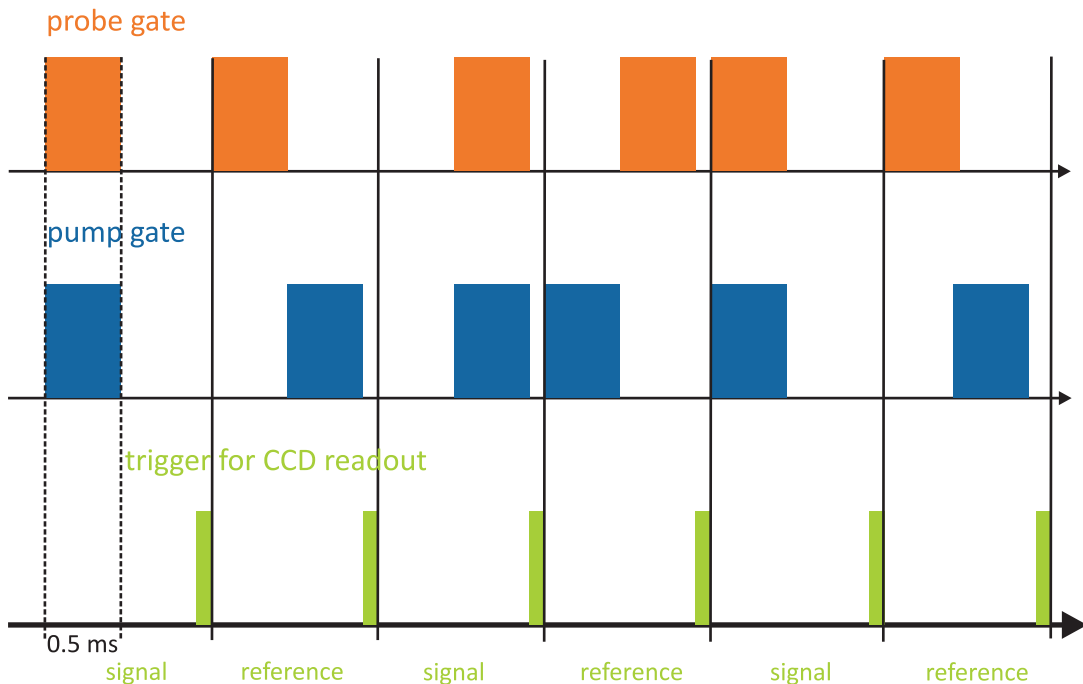


Figure 3.13: Gating scheme: Signal and reference frames are alternately recorded. For a signal frame both pump and probe beams are gated on at the same time by the AOMs, whereas they are displaced in time for a reference frame. Short trigger pulses are fed to the CCD-controller so that the readout is always synchronous to the AOM gating signals.

from the sum of the even frames. An integration time of ten minutes gives, for example, $4 \cdot 10^5$ frames which had about $1.25 \cdot 10^5$ photons incident on each pixel. That sums up to about $5 \cdot 10^{10}$ collected photons making shot-noise limited measurements of signals as small as $4 \cdot 10^{-6}$ possible.

Fig. 3.14 shows an example of the probe spectrum $R(\omega, \Delta t)$ (blue curve) and the difference of subsequent frames $\Delta R(\omega, \Delta t)$ (red curve) as a function of the detuning ΔE from the fundamental exciton transition in a single quantum dot. One can discern two contributions to ΔR : a spectrally broad signal that reproduces the shape of the probe spectrum and a sharp, dispersive feature at the exciton transition energy. The broad signal originates from a modified reflectivity due to the presence of photocarriers created by band absorption in the GaAs substrate and cap [112,113]. According to Fig. 3.12(b), we expect a dispersive spectral feature from the quantum dot at the exciton resonance, as the distance of the quantum dot to the sample surface corresponds to a phase lag

$$\phi = \frac{n_{\text{GaAs}} d}{\lambda} = \frac{3.45 \cdot 130 \text{ nm}}{720 \text{ nm}} \approx 0.2 \pi .$$

This sharp contribution to the spectrum is due to bleaching of the $|00\rangle \rightarrow |01\rangle$ transition (see Fig. 3.14(a)). When the pump pulse populates state $|10\rangle$, the transition $|00\rangle \rightarrow |01\rangle$

3 Transient differential reflectivity spectroscopy of single quantum dots

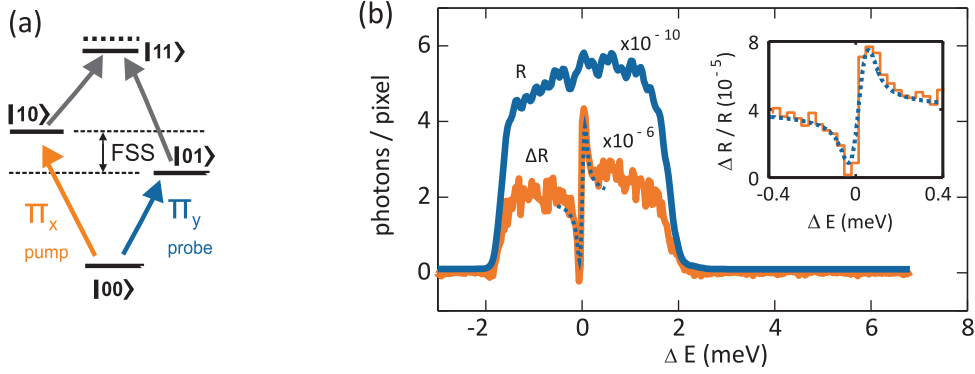


Figure 3.14: Reflected probe spectrum $R(\omega, \Delta t)$ in the presence of the pump alone (blue curve) and with the reference (no pump) subtracted from it $\Delta R = R(\omega, \Delta t) - R_0(\omega)$ (red curve) for a QD 130 nm beneath the sample surface and a delay of 150 ps. Inset: $\Delta R/R$ raw data (red step plot) and fit to the line shape (blue, dashed curve).

can not be driven and no material polarization is created by the probe pulse, in consequence. The amplitude of the dispersive feature therefore monitors the population n_{10} of state $|10\rangle$. The measured lineshape for a certain burial depth is inverted with respect to Fig. 3.12(b) as for a bleaching signal the reference frame shows the absorption feature from the QD, whereas the signal frame has a flat spectrum. The difference of signal and reference is then just the inverted calculated spectrum according to Eqn. 3.10. We fit the lineshape [94, 109] and obtain a zero-to-peak amplitude of $\Delta R/R = 4.0 \cdot 10^{-5}$. The noise of our measurement was determined by calculating the standard deviation of $\Delta R/R$ spectra for a 100 pixel window that is off resonance with respect to the QD. We obtained a noise contribution of $2.3 \cdot 10^5$ photons per pixel. As the amount of photon shot-noise for our signal strength of $5.7 \cdot 10^{10}$ collected photons per pixel is given by $2.4 \cdot 10^5$ photons, we can assume that shot-noise is the only significant source of noise in our experiment.

For a dispersive lineshape and a reduction of 20 due to the finite resolution of our spectrometer we can expect a zero-to-peak signal amplitude of about $3.8 \cdot 10^{-4}$, according to equation 3.10. This value is about one order of magnitude larger than the one obtained experimentally. One has to bear in mind, however, that we have not considered the collection efficiency of our microscope, yet. As our microscope objective has an numerical aperture of 0.7 we only collect scattered light out of a solid angle $\Omega = \int_0^\theta 2\pi \cdot \sin(\Theta) d\Theta$, with $\theta = \arcsin(\text{NA})$ being the opening angle of the detection cone according to our NA. We assumed a dipole emitting spherical waves here, for simplicity. This yields a collection efficiency for the scattered power of $\eta_{\text{coll}} = \Omega/2\pi \approx 0.286$ compared to the entire upper halfspace which we had assumed from Eq. 3.4. As our signal is sensitive to the scattered field, we have to consider a reduction in $\sqrt{0.286} \approx 0.535$. Now, the expected signal is reduced to values around $2.0 \cdot 10^{-4}$ due to the limited collection efficiency, which is still more than five times as large as the signal $\Delta R/R = 4.0 \cdot 10^{-5}$ we actually measure

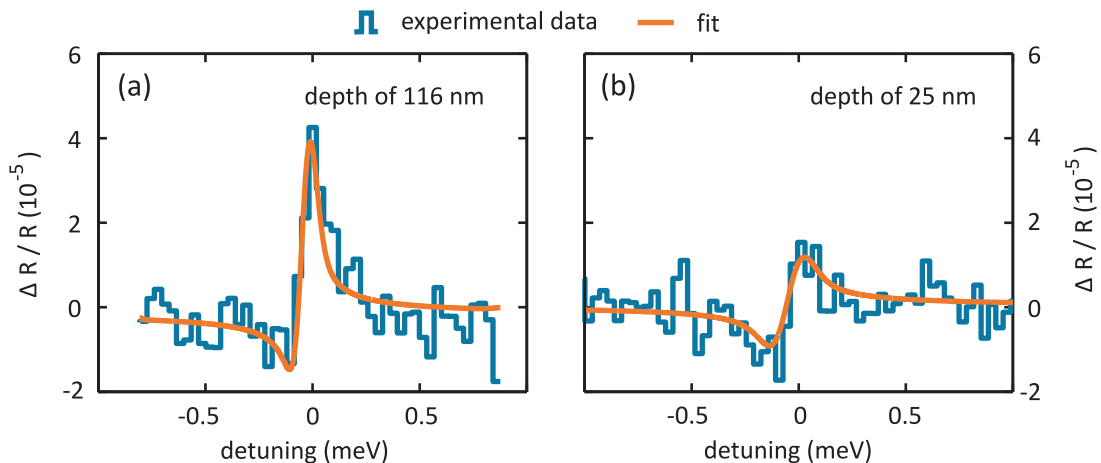


Figure 3.15: The shape of differential reflectivity spectra depend on the phase difference between the scattered and the reflected waves. Experimental data is shown as a blue step plot while the red curve is a fit according to Eq. 3.10. For a single QD buried 116 nm beneath the sample surface the lineshape becomes asymmetric (a). The spectrum of a dot 25 nm from the surface has the same relative shape as our standard dots at 130 nm and a drastically reduced amplitude (b).

in our experiment.

The remaining discrepancy can be explained by the fact that the actual emission pattern of a dipole near an interface is not given by a spherical wave, as we assumed for the simple estimation of the collection efficiency given above. In fact, a dipole which is situated in a material of high refractive index ($n_{\text{GaAs}} \approx 3.45$ at $\lambda = 720$ nm) will emit predominantly into the surrounding material and only a small fraction of the total emitted power can be detected outside of the crystal. Novotny and Hecht describe this situation very well in chapter 10.7 of reference [64]. They give the total emitted power per unit solid angle of a dipole near an interface. For our situation of a dipole oriented in the plane of the interface, which sits at a distance of 130 nm from the surface of a GaAs crystal and which has a resonance wavelength of 720 nm we can collect 1% of the total emitted power using an NA of 0.7. This corresponds to an electric field ratio of 10%. When we consider this collection efficiency, compared to the case where we assumed that we can collect the power from an entire halfspace ($1/\sqrt{2}$ of the emitted field), we can estimate a total center-to-peak signal amplitude of $\Delta R/R \approx 4.4 \cdot 10^{-5}$. This more realistic value agrees very well with our measured signal amplitudes of $\Delta R/R = 4.0 \cdot 10^{-5}$. In spite of the finite monochromator resolution, the limited numerical aperture of our microscope and the relatively low collection efficiency due to the high refractive index material which surrounds our QDs, Fig. 3.14 demonstrates that plain far-field reflection spectroscopy is able to measure transient absorption signals of a single quantum dot.

Figure 3.15 shows differential spectra for samples with a smaller upper barrier thickness as our previously introduced samples which were buried 130 nm beneath the crystal

surface. Experimental data is shown as a blue step plot while the red curve is a fit according to Eq. 3.10. Subfigure (a) shows a case for a distance of 116 nm from the surface. The lineshape of the differential spectrum is not dispersive anymore but almost a peak. Its width is still limited by the resolution of our monochromator and its amplitude is also comparable to those of deeper lying dots. This is no longer the case for a dot which is just separated by 25 nm from the surface, as the example displayed on Fig. 3.15(b) shows. QDs grown close to the surface are interesting in the context of coupling to resonant nanoantennas as introduced in section 2.4.1. Here the linewidth appears to be about $200 \mu\text{eV}$, which would be twice the resolution of the monochromator. The amplitude of the signal is, however, so much decreased that the lineshape can not be determined very precisely anymore. The signal-to-noise ratio is just enough to detect a bleaching feature but not sufficient for more challenging coherent experiments. Both the reduction in signal amplitude and the increase in linewidth for dots close to the surface indicates a fluctuating environment affecting the resonance of the QD via spectral diffusion. This might be due to defects and charge traps near the surface which cause a fluctuating local electric field. The reduced quality of QDs grown close to the surface makes their coupling to plasmonic nanoantennas very challenging. As soon as higher quality samples with passivated surfaces are available, though, coherent studies of coupled hybrid systems can be conducted.

3.4 Filming excitons: Free induction decay

We can follow the dynamics of the exciton in the time domain. A classical example is the perturbation of the free induction decay by the pump pulse [92, 114, 115]. In a density matrix picture, the probe pulse creates coherence between the states $|00\rangle$ and $|01\rangle$. The exponential decay of the coherence leads via Fourier transform to the Lorentzian spectral line of the scattered light. When a pump pulse (coming after the probe pulse) perturbs the decay of the coherence in some way, the spectral shape changes, resulting in a differential signal.

Figure 3.16 presents transient reflection spectra for pump-probe delays varying from -30 ps to +120 ps. Positive delays describe a pump pulse that precedes the probe pulse. In this case the pump pulse depletes the ground state which leads to bleaching signals. We find a dispersive spectral feature that decays with the exciton lifetime on a 200 ps timescale. For negative delays the spectra show fringes that separate further when reducing the pump-probe delay, resulting in hyperbolic features. Figures 3.16(c,d) show cross sections at -10 ps and 24 ps through the spectral maps presented on Figs. 3.16(a,b). Spectral oscillations are clearly visible for negative delays.

The whole dataset can be simulated using a density matrix model of only three levels ($|00\rangle$, $|01\rangle$, $|10\rangle$) that are optically connected in a V shape. We find perfect agreement

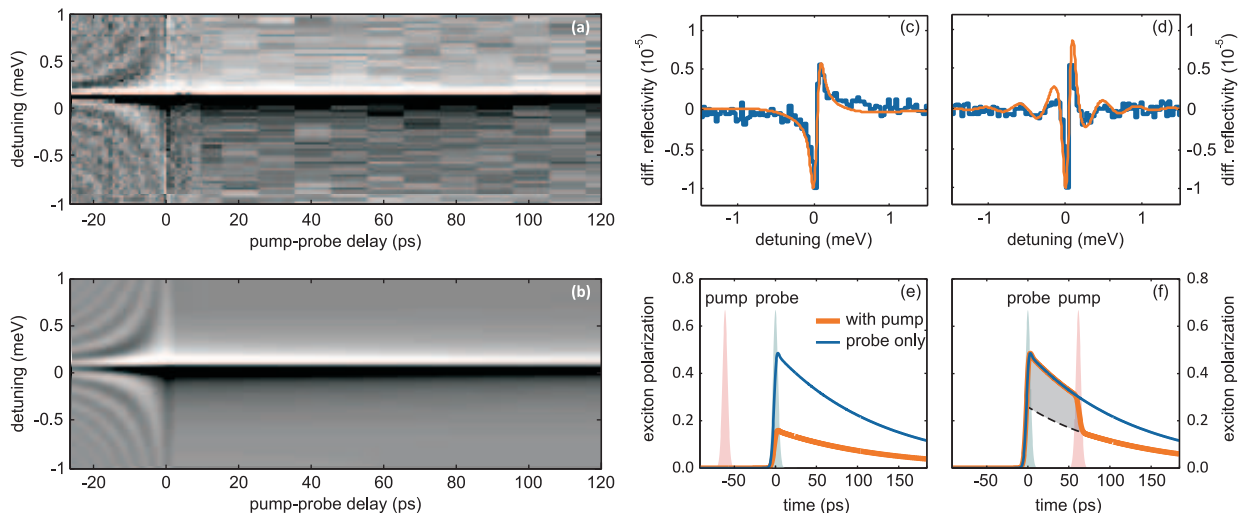


Figure 3.16: Top: Differential spectra as a function of pump-probe delay in experiment (a) and simulation (b). Experimental data of $\Delta R/R$ spectra (blue line) and simulated spectra (red line) for a pump-probe delay of $\Delta t = -10$ ps (c) and 24 ps (d). For negative delays the differential signal is due to perturbed free induction decay of the polarization created by the probe pulse and shows spectral oscillations, as a result. We observe a simple dispersive lineshape originating from bleaching of the exciton's absorption for positive delays. In both cases the signal is due to the pump induced change in the material polarization $P_{\text{QD}}(t)$ that is created by the probe pulse. Temporal evolution of the probed exciton polarization for the probe arriving after the pump pulse (positive delays, (e)) and the probe preceding the pump pulse (negative delays, (f)). In the first case, the pump depletes the ground state, reducing the probed polarization. In the second case, the pump perturbs the polarization, leading to spectral fringes.

in all details when taking into account the interference of the scattered and reflected probe field. The only free fitting parameters are the coherence time $T_2 = 90$ ps and the lifetime $T_1 = 230$ ps of the probed transition.

In the density matrix model the scattered probe field equals the imaginary part of the matrix element $\rho_{|00\rangle|01\rangle}$, describing the probed exciton polarization. Figures 3.16(e,f) depict examples of the temporal evolution for negative and positive pump-probe delay. For positive delay the pump pulse bleaches the ground state $|00\rangle$ so that less polarization is built up, resulting in a weaker scattered field and a dispersive feature in the transient reflection spectrum. For negative pump-probe delays, the decay of the polarization is perturbed by the pump pulse as it bleaches the ground state. The resulting polarization trace can be seen as the sum of a reduced free induction decay and a rectangle with a width equal to the pump-probe delay (shaded area in Fig. 3.16(f)). The latter leads by Fourier transform to the sinc-shaped fringes in the spectral domain. This example shows that the great advantage of spectrally resolved experiments is that one can distinguish

3 Transient differential reflectivity spectroscopy of single quantum dots

between different contributions to the overall signal such as background contributions, coherent artifacts and bleaching by their differing spectral characteristics.

We model the time-dynamics of the quantum dot excitonic state by a V-type three level system (see 3.14(a)). In our case, the three level system interacts with two subsequent electromagnetic pulses, which drive the transitions in various ways and create coherent superpositions of the ground state and the two excited states respectively. These are subject to decay processes, each of which is defined by a population decay rate γ_i and a pure dephasing rate γ'_i . A direct population exchange between the excited states is forbidden. The detuning of the resonances from the rotating frame is called Δ . The splitting frequency between the resonances is called $\omega_{|01\rangle|10\rangle}$. Since the light pulses are spectrally broad compared to the exciton resonances, they are quasi-resonant to both transitions in the case of reasonable energy splitting. It is possible, though, to define a detuning of the pulses much larger than the bandwidth to simulate non-resonant interaction. The pulse detuning is given with respect to the rotating frame.

We can obtain the time-dynamics of the system by solving numerically the corresponding density matrix master equation [116, 117],

$$\dot{\rho} = -i[\rho, \mathbf{H}] + \mathbf{L}\rho, \quad \hbar = 1 \quad . \quad (3.11)$$

Here, ρ is the density operator of the system, \mathbf{H} is the Hamiltonian and \mathbf{L} is a damping operator. The Hamiltonian includes the dynamics due to detuning and frequency splitting of the V-system and the interaction with the light field:

$$\mathbf{H} = (\Delta - \omega_{|01\rangle|10\rangle})\sigma_{|01\rangle|01\rangle} + \Delta\sigma_{|10\rangle|10\rangle} + [\Omega_{|01\rangle}\sigma_{|01\rangle|00\rangle} + \Omega_{|10\rangle}\sigma_{|10\rangle|00\rangle} + H.c.] \quad , \quad (3.12)$$

where the σ_{ij} are the projection operators $|i\rangle\langle j|$. The instantaneous Rabi frequencies $\Omega_{|01\rangle,|10\rangle}$ for each transition are determined by the time-evolution of the pulse envelope only, as the carrier oscillation is compensated by the rotating frame. If the pulses are detuned, the envelope is modulated with the difference between rotating frame and the carrier frequency. Thus, the Hamiltonian is time dependent.

The damping operator describes the phenomenological decay of population and polarization (diagonal and off-diagonal elements of ρ , respectively). It includes the population decay rate γ_i and pure dephasing rate γ'_i of the excited state $|i\rangle$ and the ground state.

When ρ is written as a column vector

$$\rho = \{\rho_{|00\rangle|00\rangle}, \rho_{|01\rangle|00\rangle}, \rho_{|10\rangle|00\rangle}, \rho_{|00\rangle|01\rangle}, \rho_{|01\rangle|01\rangle}, \rho_{|10\rangle|01\rangle}, \rho_{|00\rangle|10\rangle}, \rho_{|01\rangle|10\rangle}, \rho_{|10\rangle|10\rangle}\}^T \quad ,$$

it can be expressed as a 9x9-matrix $\mathbf{L} = \mathbf{L}_{|01\rangle} + \mathbf{L}_{|10\rangle}$, where

$$\mathbf{L}_{|01\rangle} = \begin{pmatrix} 0 & 0 & 0 & 0 & \gamma_{|01\rangle} & 0 & 0 & 0 & 0 \\ 0 & -\left(\frac{\gamma_{|01\rangle}}{2} + \gamma'_{|01\rangle}\right) & 0 & 0 & 0 & 0 & 0 & 0 & 0 \\ 0 & 0 & 0 & 0 & 0 & 0 & 0 & 0 & 0 \\ 0 & 0 & 0 & -\left(\frac{\gamma_{|01\rangle}}{2} + \gamma'_{|01\rangle}\right) & 0 & 0 & 0 & 0 & 0 \\ 0 & 0 & 0 & 0 & -\gamma_{|01\rangle} & 0 & 0 & 0 & 0 \\ 0 & 0 & 0 & 0 & 0 & -\left(\frac{\gamma_{|01\rangle}}{2} + \gamma'_{|01\rangle}\right) & 0 & 0 & 0 \\ 0 & 0 & 0 & 0 & 0 & 0 & 0 & 0 & 0 \\ 0 & 0 & 0 & 0 & 0 & 0 & 0 & -\left(\frac{\gamma_{|01\rangle}}{2} + \gamma'_{|01\rangle}\right) & 0 \\ 0 & 0 & 0 & 0 & 0 & 0 & 0 & 0 & 0 \end{pmatrix} \quad (3.13)$$

$$\mathbf{L}_{|10\rangle} = \begin{pmatrix} 0 & 0 & 0 & 0 & 0 & 0 & 0 & 0 & \gamma_{|10\rangle} \\ 0 & 0 & 0 & 0 & 0 & 0 & 0 & 0 & 0 \\ 0 & 0 & -\left(\frac{\gamma_{|10\rangle}}{2} + \gamma'_{|10\rangle}\right) & 0 & 0 & 0 & 0 & 0 & 0 \\ 0 & 0 & 0 & 0 & 0 & 0 & 0 & 0 & 0 \\ 0 & 0 & 0 & 0 & 0 & 0 & 0 & 0 & 0 \\ 0 & 0 & 0 & 0 & 0 & -\left(\frac{\gamma_{|10\rangle}}{2} + \gamma'_{|10\rangle}\right) & 0 & 0 & 0 \\ 0 & 0 & 0 & 0 & 0 & 0 & -\left(\frac{\gamma_{|10\rangle}}{2} + \gamma'_{|10\rangle}\right) & 0 & 0 \\ 0 & 0 & 0 & 0 & 0 & 0 & 0 & -\left(\frac{\gamma_{|10\rangle}}{2} + \gamma'_{|10\rangle}\right) & 0 \\ 0 & 0 & 0 & 0 & 0 & 0 & 0 & 0 & -\gamma_{|10\rangle} \end{pmatrix} \quad (3.14)$$

The backscattered electric field can be obtained from the time derivative of the imaginary part of the coherent QD polarization, $\text{Im}\{dP_{\text{QD}}/dt\}$. From this field we calculate the scattering spectra of the quantum dot by Fourier transformation [94]. The result is superimposed with the surface-reflected probe pulse to compute the differential spectra. To take care of the limited resolution of our monochromator, the spectra are convoluted with a Gaussian with a FWHM of $100 \mu\text{eV}$.

3.5 Conclusion

We demonstrated that simple far-field reflection spectroscopy is sufficient to determine the ultrafast dynamics of a single self-assembled quantum dot, without any further requirements to the sample design. As long as there is optical access to the quantum dot, ultrafast transient spectra can readily be obtained with our pump-probe scheme. Our double modulation technique makes shot-noise limited data acquisition possible and we could reach a signal-to-noise ratio of 17 in transient absorption spectra from a single QD. The signal amplitude is on the order of 10^{-4} which is mainly limited by the spectral resolution of our monochromator ($100 \mu\text{eV}$) and the spot size of the probe laser on the sample (750 nm). We demonstrated as an example spectrally resolved

3 Transient differential reflectivity spectroscopy of single quantum dots

perturbed free induction decay of a localized exciton in full agreement with a density matrix model involving only a three level V-system. The experimental data agrees well with a population lifetime of $T_1 = 230$ ps and a dephasing time of $T_2 = 90$ ps.

4 Rabi oscillations in single GaAs quantum dots

We are using a spectrally resolved technique of transient differential reflectivity in order to coherently control and read out an excitonic qubit in a single GaAs quantum dot relying entirely on far-field microscopy. We were able to record Rabi oscillations in the fundamental transition of a quantum dot yielding transition dipole moments around $18 D$. The system appears to behave according to the optical Bloch equations for a simple two-level system up until a pulse area of 2π . At higher pump powers I_{pump} the Rabi frequency is not increasing proportional to $\sqrt{I_{\text{pump}}}$ anymore. Instead, we observe a stretching of the Rabi oscillations' period for higher pump powers. We attributed this deviation from the simple two-level system solution to an interaction between the localized exciton in the QD and hot charge carriers that are excited by the pump in the GaAs substrate of the structure.

4.1 Introduction

For many quantum devices as mentioned in chapter 1 it is crucial that the light field is interacting coherently with the matter system. In this way the system can be, for example, completely inverted and the entire population is in the upper state. In order to achieve this in a QD, where the neutral exciton has lifetimes below 1 ns [118], one has to employ ultrafast light pulses [119].

We are using an all-optical pump-probe technique as described in chapter 3 in order to address ground state to neutral exciton transitions in our GaAs/AlGaAs QDs. The pump pulses are driving the system coherently causing population oscillations (Rabi oscillations) between the ground state and the excited state. By setting the pulse energy one can control the degree of inversion in the system and thus write arbitrary charge states into this excitonic qubit. Ultrafast control of the population in a single QD has already been demonstrated for InGaAs QDs using PL [89,120], for naturally formed interface GaAs QDs using differential transmission and four-wave mixing (FWM) [86,121] and differential reflection using a near-field optical microscope [95]. Our approach is to use far-field microscopy only without using nanoapertures in order to increase the SNR of our experiment. Differential reflection of delayed probe pulses is employed in order to read out the charge state of the qubit after its interaction with the pump pulses. The observation of Rabi oscillations is a very convenient test for coherent light-matter interaction as it also yields the magnitude of the exciton's transition dipole moment, μ . Our method is directly measuring the absorption of the exciton and does not require a photon to be emitted such as in PL.

4.2 Quantum mechanics of a two-level system

A quantum mechanical two-level system is the most simple and idealized model system for light matter interaction [122]. It considers two energy levels E_1 and E_2 with static orbits $\phi_1(\mathbf{r})$ and $\phi_2(\mathbf{r})$. The system can exchange energy with the outside world by jumping from one orbit to the other through the emission or absorption of a photon, for example. Although QDs are more complex than a simple two-level system, many effects can be adequately described already by this model. As will become apparent in this chapter, one always has to bear in mind that the system at hand is a semiconductor nanocrystal embedded in a host crystal. So the Rabi oscillations that are observed in our real system differ from those expected for a two-level atom. As a rough rule one can say, that as long as the light only addresses one transition between two energy states and the upper state spontaneously decays with a large radiative rate into the lower state a two-level atom description might be justified. Exciton-biexciton transitions can be suppressed by choosing the right photon energy of the laser pulses due to the substantial biexciton shift

of several meV. A second ground state to neutral exciton transition due to the finite fine-structure splitting in epitaxial GaAs QDs can be excluded by polarization, as the two fine-structure split lines have orthogonal linear polarizations. So under appropriate experimental conditions, the two-level approximation holds to a certain degree and is able to explain the basic behavior of the system.

Before presenting the experimental results on Rabi oscillations in single GaAs QDs, the physics of a two-level system is reviewed and the Optical Bloch Equations are introduced as a convenient, conceptual picture. Furthermore, different decay mechanisms and lifetimes of the excited state are discussed. This theoretical introduction to the material is mostly following [122] and [123].

4.2.1 Time dependent Schrödinger equation

An isolated quantum system is static and neither the states $\psi(\mathbf{r}) = \sum_n \phi_n(\mathbf{r})$ nor the Hamiltonian $H_a = \mathbf{p}^2/2m - V(\mathbf{r})$ depend on time. In this case the time-independent Schrödinger equation $E\psi(\mathbf{r}) = H_a\psi(\mathbf{r})$ is describing the system adequately. Dynamics can be introduced via an external potential $V_{ext}(\mathbf{r}, t)$ which depends explicitly on time and is added to the Hamiltonian of the system. Here, H_a symbolizes the atomic part of the Hamiltonian as opposed to the external potential, $V_{ext}(\mathbf{r}, t)$, which can be created by a time-dependent optical field.

$$H = H_a + V_{ext}(\mathbf{r}, t) \quad (4.1)$$

The resulting Schrödinger equation now reads

$$\left(\frac{\hbar^2}{2m} \nabla^2 + V(\mathbf{r}) + V_{ext}(\mathbf{r}, t) \right) \psi(\mathbf{r}, t) = i\hbar \frac{\partial \psi}{\partial t} \quad . \quad (4.2)$$

We can find solutions to this problem by using the completeness of the wave functions

$$\psi(\mathbf{r}, t) = \sum_n a_n(t) \phi_n(\mathbf{r}) \quad . \quad (4.3)$$

When we now apply equation (4.2) to $\psi(\mathbf{r}, t)$ and bear in mind that the $\phi_n(\mathbf{r}, t)$ are solutions to H_a with energy eigenvalues E_n , we can write the Schrödinger equation as

$$\sum_n a_n(t) [E_n + V_{ext}] \phi_n(\mathbf{r}) = \sum_n i\hbar \frac{\partial a_n}{\partial t} \phi_n(\mathbf{r}) \quad . \quad (4.4)$$

The next step is the projection of equation 4.4 along the functions $\phi_m(\mathbf{r})$ using

$$\langle \phi_m | \phi_n \rangle = \int_V \phi_m^*(\mathbf{r}) \phi_n(\mathbf{r}) d^3r = \delta_{mn} \quad . \quad (4.5)$$

4 Rabi oscillations in single GaAs quantum dots

A compact form of the Schrödinger equation is given by

$$i\hbar\dot{a}_m = E_m a_m + \sum_n V_{mn}(t) a_n \quad , \quad (4.6)$$

using the abbreviation

$$V_{mn}(t) = \int_V \phi_m^*(\mathbf{r}) V_{ext} \phi_n(\mathbf{r}) d^3r \quad (4.7)$$

for the matrix elements of V_{ext} between the states m and n . It should be pointed out that the $\phi(\mathbf{r})$ remain static orbitals and the dynamics of the system is described by the time-dependent probability amplitudes $a_n(t)$ which express the degree that a certain $\phi_n(\mathbf{r})$ is contributing to the state of the system $\psi(\mathbf{r}, t) = \sum_n a_n(t) \phi_n(\mathbf{r})$ at a time, t .

We can describe the interaction between an electromagnetic wave $\mathbf{E}(\mathbf{R}, t)$ of frequency ω and an electron by the external potential

$$V_{ext}(\mathbf{r}, \mathbf{R}, t) = -e\mathbf{r} \cdot \mathbf{E}(\mathbf{R}, t), \quad \text{with} \quad \mathbf{E}(\mathbf{R}, t) = \frac{1}{2} \hat{\epsilon} E_0 e^{-i\omega t} + c.c. \quad . \quad (4.8)$$

Here we choose the position of the atom, \mathbf{R} , to be zero and the polarization state of the optical wave is described by $\hat{\epsilon}$. When the orbitals $\phi(\mathbf{r})$ have a defined parity, the diagonal matrix elements in equation (4.7) have to be zero and the probability amplitudes of a two-level system behave according to:

$$i\hbar\dot{a}_1 = E_1 a_1 + V_{12}(t) a_2 \quad (4.9a)$$

$$i\hbar\dot{a}_2 = E_2 a_2 + V_{21}(t) a_1 \quad (4.9b)$$

with

$$V_{12} = -e\mathbf{r}_{12} \cdot \frac{1}{2} (\hat{\epsilon} E_0 e^{-i\omega t} + c.c.) \quad (4.10a)$$

$$V_{21} = -e\mathbf{r}_{21} \cdot \frac{1}{2} (\hat{\epsilon} E_0 e^{-i\omega t} + c.c.) \quad (4.10b)$$

The matrix elements of \mathbf{r} are again defined like in equation 4.7

$$\mathbf{r}_{mn} \equiv \int \phi_m^*(\mathbf{r}) \mathbf{r} \phi_n(\mathbf{r}) d^3\mathbf{r} \quad . \quad (4.11)$$

It turns out to be convenient to write the equations in frequency units rather than energies, so we can adopt the following conventions:

$$\omega_{12} = \frac{E_2 - E_1}{\hbar} \quad (4.12)$$

$$\chi_{21} = e(\mathbf{r}_{21} \cdot \hat{\epsilon}) \frac{E_0}{\hbar} \quad (4.13)$$

$$\chi_{12} = e(\mathbf{r}_{12} \cdot \hat{\epsilon}) \frac{E_0}{\hbar} \quad (4.14)$$

where ω_{12} is the optical transition frequency and χ is the so-called Rabi frequency which is a measure for the field-atom interaction energy. When we choose the energy of the lower level, E_1 , to be zero, then equations (4.9) can be expressed as

$$i\dot{a}_1 = -\frac{1}{2}(\chi_{12}e^{-\omega t} + \chi_{21}^*e^{i\omega t})a_2 \quad (4.15a)$$

$$i\dot{a}_2 = \omega_{21}a_2 - \frac{1}{2}(\chi_{21}e^{-\omega t} + \chi_{12}^*e^{i\omega t})a_1 \quad (4.15b)$$

When we have a look at the above equations we notice that the solutions for the probability amplitudes are rotating very rapidly. For vanishing external field $a_2(t) = a_2(0)\exp(-i\omega_{21}t)$, which is oscillating with the transition frequency of the two-level system. It is very convenient to make a transformation into a frame of reference that already includes this rapid oscillation. In this way we have a system with small derivatives with respect to time making it much easier to solve the system numerically. The following transformation facilitates this change in frame of reference:

$$a_1(t) = c_1(t) \quad (4.16a)$$

$$a_2(t) = c_2(t)e^{-\omega t} \quad (4.16b)$$

The new equations of motion for the $c_{1/2}$ are

$$i\dot{c}_1 = -\frac{1}{2}(\chi_{12}e^{-2\omega t} + \chi_{21}^*)c_2 \quad (4.17a)$$

$$i\dot{c}_2 = (\omega_{21} - \omega)c_2 - \frac{1}{2}(\chi_{21} + \chi_{12}^*e^{2i\omega t})c_1 \quad (4.17b)$$

We see from the above equations that there are now oscillating and static contributions to the rate of change of the probability amplitudes. As the non-static contributions are oscillating with twice the transition frequency they can be neglected as they will cancel out for time intervals that are longer than one optical cycle of a quasi-resonant wave. This approximation is known as the rotating-wave approximation and it results in the these very simple equations of motion for the probability amplitudes:

$$i\dot{c}_1 = -\frac{1}{2}\chi^*c_2 \quad (4.18a)$$

$$i\dot{c}_2 = \Delta c_2 - \frac{1}{2}\chi c_1 \quad (4.18b)$$

We do no longer need a subscript for the Rabi frequency and the frequency detuning $\Delta = \omega_{21} - \omega$ is introduced. The density matrix of the system is given by

$$\rho = \begin{pmatrix} \rho_{11} & \rho_{12} \\ \rho_{21} & \rho_{22} \end{pmatrix} = \begin{pmatrix} c_1c_1^* & c_1c_2^* \\ c_2c_1^* & c_2c_2^* \end{pmatrix} . \quad (4.19)$$

The diagonal elements of the density matrix are simply the probabilities of occupation for the two energy levels and the off-diagonal entries are the complex amplitudes of the

electron's displacement. So ρ_{21} and ρ_{12} are a measure for the material polarization. The density matrix equations are differential equations which describe the dynamics of the density matrix. They can be constructed from equations (4.18) and (4.19).

$$\dot{\rho}_{12} = i\Delta\rho_{12} + i\frac{\chi^*}{2}(\rho_{22} - \rho_{11}) \quad (4.20a)$$

$$\dot{\rho}_{21} = -i\Delta\rho_{21} + i\frac{\chi}{2}(\rho_{22} - \rho_{11}) \quad (4.20b)$$

$$\dot{\rho}_{11} = -\frac{i}{2}(\chi\rho_{12} - \chi^*\rho_{21}) \quad (4.20c)$$

$$\dot{\rho}_{22} = \frac{i}{2}(\chi\rho_{12} - \chi^*\rho_{21}) \quad (4.20d)$$

Instead of solving equations (4.20) right away, we will first introduce the optical Bloch equations.

4.2.2 Optical Bloch equations

A simple and conceptual description of near-resonant light matter interaction equivalent to the density matrix equations is given by the optical Bloch equations. We can already see from equations 4.20 that it is sufficient only to consider the inversion $\rho_{22} - \rho_{11}$ as the probabilities of occupation never appear alone. Making use of the fact that probability is conserved, $\rho_{11} + \rho_{22} = 1$, in the absence of decay channels, we can describe the system with three instead of four quantities:

$$u = \rho_{21} + \rho_{12} \quad (4.21a)$$

$$v = i(\rho_{21} - \rho_{12}) \quad (4.21b)$$

$$w = \rho_{22} - \rho_{11} \quad (4.21c)$$

Here u and v make up the complex polarization of the two-level system and w is the population inversion. Substituting equations (4.21) into (4.20) gives

$$\dot{u} = -\Delta v \quad (4.22a)$$

$$\dot{v} = \Delta u + \chi w \quad (4.22b)$$

$$\dot{w} = \chi v \quad (4.22c)$$

Writing above equations in vectorial form yields

$$\frac{d\mathbf{S}}{dt} = \mathbf{Q} \times \mathbf{S} \quad , \quad \text{with} \quad \mathbf{S} = \begin{pmatrix} u \\ v \\ w \end{pmatrix} \quad \text{and} \quad \mathbf{Q} = \begin{pmatrix} -\chi \\ 0 \\ \Delta \end{pmatrix} \quad . \quad (4.23)$$

Just like in the fields of nuclear magnetic resonance and electron spin resonance the Bloch vector \mathbf{S} can be placed into the Bloch sphere which is seen on Fig. 4.1(a). The

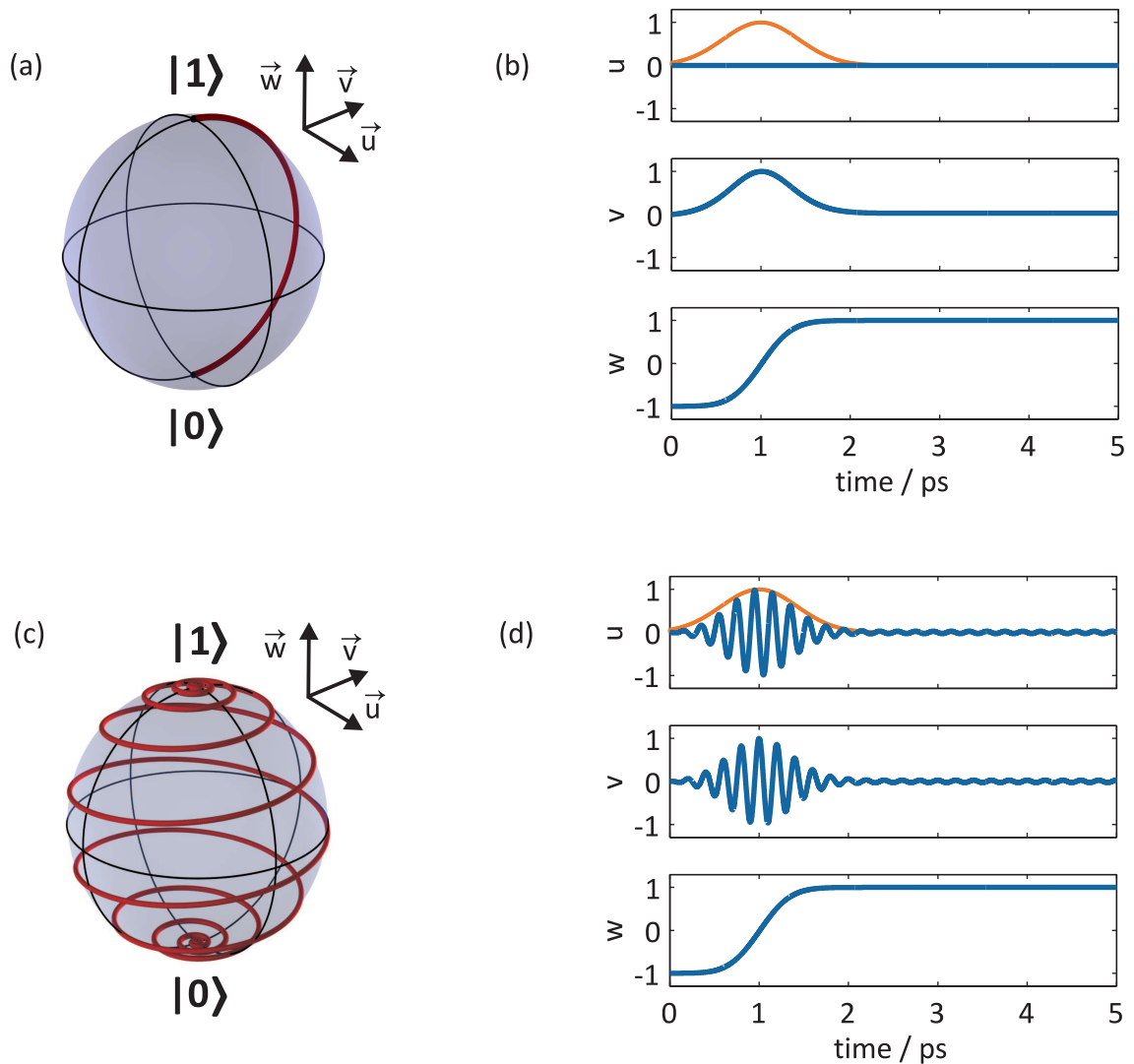


Figure 4.1: Response of a two-level system to a π -pulse: (a) Rotating frame: The red trace on the Bloch sphere shows the state being driven from the ground- to the excited state. (b) Components of the Bloch vector as a function of time. The pump pulse is shown in red. (c) Lab frame: The Bloch vector revolves around the w -axis with the transition frequency, while the system is driven to the excited state. (d) Components of the Bloch vector as a function of time. The pump pulse is shown in red.

displayed solutions were obtained by integrating the optical Bloch equations numerically using a Runge-Kutta algorithm of the 4th order. Here the population inversion is plotted on the vertical axis, whereas the complex polarization is given by the projection of the Bloch vector onto the equatorial plane. The system is residing in its ground state $|0\rangle$ when the Bloch vector is pointing towards the south pole of the sphere and it is fully inverted at the north pole $|1\rangle$. On the equator the polarization is reaching a maximum and the system is in a coherent superposition state $1/\sqrt{2}(|0\rangle + |1\rangle)$ between ground- and excited state. Figure 4.1(a) and (c) show the trace of the Bloch vector on the Bloch sphere during the interaction with a laser pulse of 1 ps in a frame rotating with the transition frequency and in the non-rotating lab frame, respectively. As one can see, the pulse rotates the state up to the north pole around the u -axis, which means that the integral in time over the Rabi frequency χ must be π :

$$\Theta = \int_{-\infty}^{\infty} \chi(t') dt' = \pi \quad , \quad \text{with} \quad \chi(t) = \frac{e(\mathbf{r}_{12} \cdot \hat{\epsilon}) E_0(t)}{\hbar} = \frac{\mu E_0(t)}{\hbar} \quad (4.24)$$

As the total angle of rotation that the optical pulse can inflict on the two-level system is given by the integral over the Rabi frequency one calls this the pulse area. So a pulse that rotates the system completely around the Bloch sphere, so that the state is again in the ground state after the interaction with the optical field, is called a 2π -pulse, for example.

4.2.3 Relaxation phenomena

When a quantum mechanical system is excited from the ground state into an excited state it does not stay in the upper state forever and the material polarization also does not stay coherent with the exciting wave forever. The inelastic decay rate $1/T_1$ can be written as

$$\frac{1}{T_1} = A_{21} + \Gamma_{21} \quad . \quad (4.25)$$

Here A_{21} is the Einstein coefficient for spontaneous emission and the rate Γ_{21} is the non-radiative decay rate which connects levels 2 and 1. T_1 is the time constant by which the population in the upper state decays into the lower state. That means that one can describe these processes by introducing a term $-1/T_1(1+w)$ in the w -component of the optical Bloch equations. However, a decay of population also influences the polarization. Taking also into account the elastic pure dephasing processes with a rate $1/\tau$, we can write the decay rate for the polarization like

$$\beta = \frac{1}{\tau} + \frac{1}{2T_1} \quad . \quad (4.26)$$

From the above equations the inequality

$$T_2 \leq 2T_1 \quad (4.27)$$

follows. The equality holds for vanishing pure dephasing. It is now possible to write down the optical Bloch equations including relaxation effects in the complex form:

$$\dot{u} - i\dot{v} = -(\beta + i\Delta)(u - iv) - i\chi w \quad (4.28a)$$

$$\dot{w} = -\frac{1}{T_1}(1 + w) + \frac{i}{2}(\chi(u + iv) - \chi^*(u - iv)) \quad (4.28b)$$

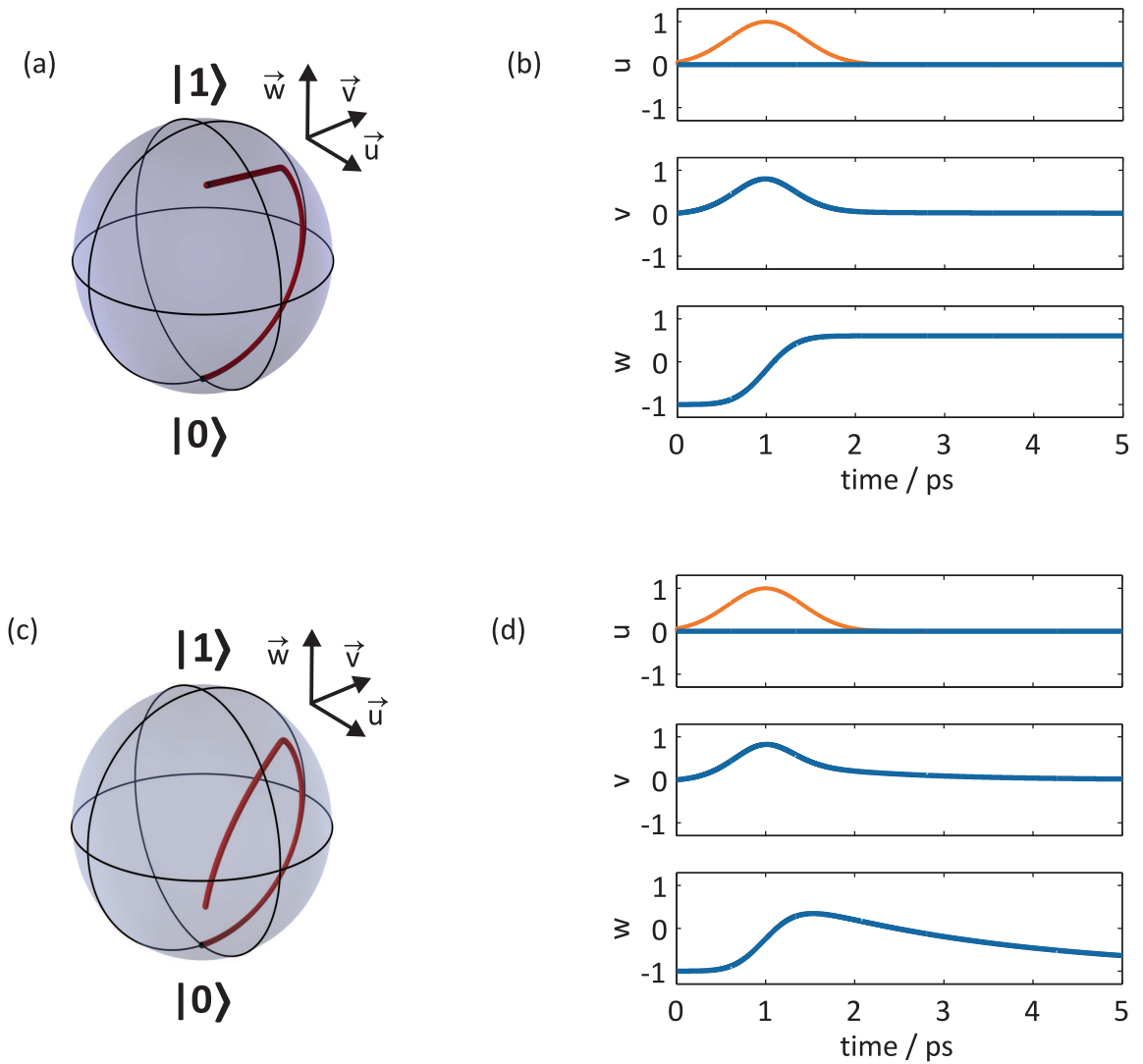


Figure 4.2: (a) Pure dephasing is dominant: The pure dephasing rate $1/\tau$ destroys the coherence or the polarization in the system. The population does not relax (limiting case for $1/\tau \gg 1/T_1$). (b) Components of the Bloch vector as a function of time. The pump pulse is shown in red. (c) No pure dephasing: Population decays with a rate $1/T_1$ and the coherence decays according to equation 4.26 for $1/\tau = 0$. (d) Components of the Bloch vector as a function of time. The pump pulse is shown in red.

Historically, T_1 and $T_2 = 1/\beta$ were called longitudinal and transverse lifetimes, respectively. These terms originate from magnetic resonance experiments and referred to the direction along or transverse to the static magnetic field [124]. On Fig. 4.2(a) and (b) the evolution of the Bloch vector is shown for the case of a high pure dephasing rate ($1/\tau \gg 1/2T_1$) and the case of low pure dephasing ($\beta = 1/T_1$). The excitation is facilitated by a resonant optical pulse with a duration of 1 ps. One can see nicely that elastic dephasing processes ($1/\tau$) pull the Bloch vector towards the w-axis, while inelastic processes make the system decay towards the south pole.

4.3 Experimental technique

Our goal is the measurement of Rabi oscillations in the neutral exciton transition of GaAs QDs. The Rabi frequencies are relatively high, as a 2π -pulse drives the system once around the Bloch sphere in one picosecond, for example. This makes the dynamics of the Bloch vector very fast and we do not directly observe it in our experiment. We record the population oscillations in the power rather than in the time domain. The QD is excited with a certain pulse area and one measures the excitonic population that remains after the interaction with the pump pulse. Solving Eqns. 4.28 for cw excitation one sees that the population varies as $w(t) = 2\sin^2(\chi t/2) - 1$ in time. When driving the system with pulses of pulse area θ the result is $w(t) = 2\sin^2(\theta/2) - 1$, for resonant excitation.

As described earlier, we use differential reflection of probe pulses in order to measure the inversion of the system after a certain delay time Δt with respect to the pump pulses. The basic experimental setup is as the one described in chapter 3. Pump and probe pulses are derived from a Ti:Sapphire laser oscillator and undergo amplitude pulse-shaping and modulation via a grating pulse shaper and an AOM, respectively. For the measurements presented in this chapter, the spectral width of the pulses was set to 2 nm by the slit width of the pulse shapers. For the pump process we can exclude the trion and biexciton transitions in this way. The advantage of this reduced spectral width for the probe pulses is, that the pulses carry more photons per wavelength interval at a constant pulse area. In this way we will have a higher SNR when we probe the system with a π -pulse, for example, as the probing photons are just spread out over a smaller spectral region. Great care was taken that the polarization axes of the pulses were mapped to the excitonic dipole axes in the QD. The polarization direction of the excitons was determined in a first step by polarization resolved PL as seen on Fig. 2.4. Then, the pump and probe beams were polarized accordingly using a Soleil-Babinet compensator, so that the probe pulses only interact with one of the fine-structure split excitonic states and the pump pulses only interact with the other one. The pump beam was suppressed in front of the monochromator using a second Soleil-Babinet compensator. Pump-probe spectra like the one shown on Fig. 3.14 are recorded for various pump powers and the

population of the higher state was extracted by a line shape fit to the spectral data.

4.4 Experimental results

Figure 4.3 shows a representative data set for Rabi oscillations. The idea of the experiment is sketched in subfigure (a). Pump pulses drive coherent population oscillations in the $|00\rangle \rightarrow |10\rangle$ transition. A π -pulse promotes the entire population into the upper state leaving the ground state empty. The presence of this exciton leads to a renormalization of the energy levels so that the $|10\rangle \rightarrow |11\rangle$ transition becomes possible and the $|00\rangle \rightarrow |01\rangle$ transition vanishes. In other words, the excitonic transition orthogonal to the one that is pumped cannot absorb anymore when the ground state is empty, so that the differential absorption of the probe pulses will be zero at the resonance frequency. The QD then becomes invisible for the probe pulse at the neutral exciton transition. Rabi oscillations are driven in one exciton (target exciton), whereas the other transition just serves as a means to make them visible (monitor exciton).

The data was taken at a fixed pump-probe delay of 150 ps in order to minimize contributions of hot delocalized carriers to the pump-probe signal (see chapter 3 and Fig. 4.4(b)). Subfigure (c) shows a spectral map of a complete power series data set. Every column is a $\Delta R/R$ spectrum for a certain pump power such as explained on Fig. 3.14. $\Delta R/R$ spectra are obtained when taking the difference between probe pulse spectra in the presence of the pump pulse (pump AOM open) and without pump pulses (pump AOM closed). A Lorentzian line shape was fit to the spectral data and the bleaching amplitudes (see Fig. 4.3(d)) were extracted.

Having a closer look on Fig. 4.3, we see that the signal rises until it reaches the highest bleaching signal. At this point the population in the pumped excitonic state is at a maximum and the ground state is maximally depopulated, thus suppressing the absorption by the perpendicular exciton transition for the probe photons. Then, the signal decreases with increasing pump power, signifying that the Bloch vector has passed the north pole of the Bloch sphere and more pump power means less population in the target state and less bleaching on the monitor state. It is noteworthy that the signal goes down completely to zero for a 2π -pulse and reaches exactly its maximum value again for a 3π -pulse. This means that we do not observe power-induced dephasing in our experiment as was observed by Unold and co-workers for naturally occurring GaAs QDs [125].

Two periods of the Rabi oscillation were recorded for pump powers up to $200 \mu\text{W}$. The first period closely follows the $\sin^2(\theta/2)$ -shape that is expected from theory. The second period, however, is stretched out to higher pump powers. The data suggests, that the Rabi frequency does not increase linearly with the pump field anymore, as Eqn. 4.14 indicates. Instead, at elevated pump powers the optical field does not drive the two-level

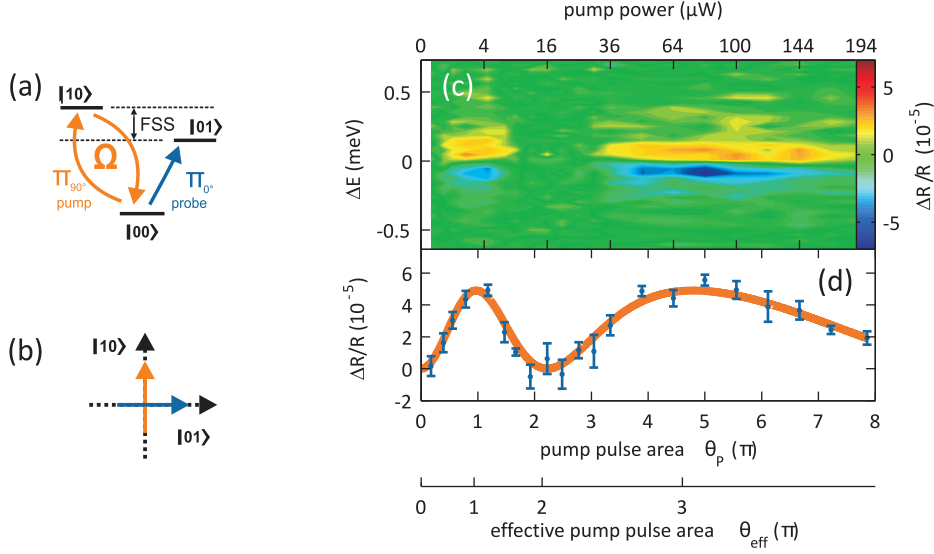


Figure 4.3: (a): Pump pulses drive Rabi oscillations on the $|00\rangle \rightarrow |10\rangle$ transition while orthogonal probe pulses monitor the bleaching on the second neutral exciton transition. (b): Pump and probe polarizations are carefully aligned to the axes of the excitonic dipoles. (c): $\Delta R/R$ spectra as a function of pulse area for $\Delta t = 150$ ps. (d): Bleaching amplitude over pulse area (blue dots) with a $\sin^2(\theta)$ -shaped least square fit considering an effective pulse area due to delocalized carriers around the quantum dot (red curve).

system as effectively as in the low power limit. We find that we can fully describe the data by considering an effective pulse area θ_{eff} which is smaller than the low-power limit θ_P

$$\theta_{\text{eff}} = \theta_P \left(1 - f_{\text{sat}} \frac{P/P_{\text{sat}}}{1 + P/P_{\text{sat}}} \right) . \quad (4.29)$$

This approach is motivated by reminding ourselves that pump pulses which are resonant to the neutral exciton transition also create carriers in the bulk GaAs surrounding the quantum dots. Here P is the pump power and P_{sat} the saturation power for photocarriers in bulk GaAs. f_{sat} is the asymptotic value of the reduction of the pulse area when the photocarrier density is fully saturated. The density of these carriers influences the overall reflectivity of the sample as can be observed in the broad background signal on Fig. 3.14 which is measured about 1-2 meV off the exciton resonance.

The background signal from the data set on Fig. 4.3 is displayed on Fig. 4.4(a). It follows a saturation law and we can determine the saturation power P_{sat} from it. The microscopic origin of the relation between the bulk carrier concentration in the substrate and the pulse area reduction is also subject of current research and will be discussed in more detail in chapter 5. The only fitting parameters in Fig. 4.3 are therefore the proportionality factor f_{sat} , the transition dipole moment μ , and the amplitude of the bleaching signal.

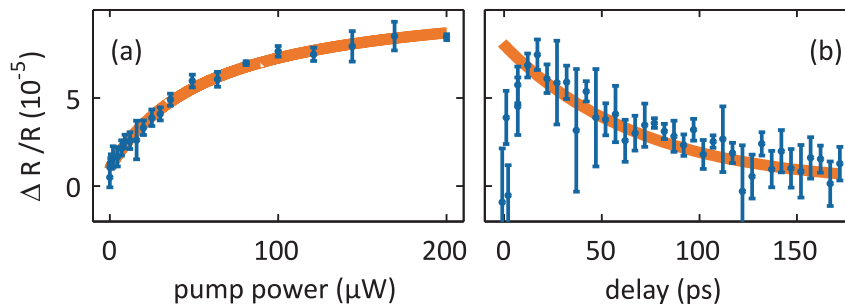


Figure 4.4: (a) Background contribution of the $\Delta R/R$ spectra as a function of pump power for $\Delta t = 150$ ps reveals the saturating photocarrier population in the vicinity of the QD. (b) Background signal decays with a lifetime of 50 ps.

In order to evaluate the stability and reproducibility of our measurement scheme, we varied the delay time Δt from 50 to 200 ps. The signal shows no dependence on the pump-probe delay but a minor reduction in amplitude due to the finite lifetime of the exciton. Comparing the pump powers which correspond to a π -pulse for several quantum dots we obtained transition dipole moments μ between 17 and 19 D. The saturation powers varied between $P_{sat} = 50 - 200 \mu\text{W}$ which corresponds to saturation intensities of 150 to 600 MW/cm^2 . This is in good agreement with the literature values for GaAs [126]. The values for the reduction parameter varied between $f_{sat} = 0.65 - 0.88$. The considerable range of the two parameters describing the delocalized carriers suggests that the environment of the different quantum dots is not very uniform. The transition dipole moments are, however, almost unaffected by the differing environments.

The values of the fit parameters for the data shown on Fig. 4.5 are displayed on table 4.1. Statistical errors were obtained evaluating four subsets of measured data ($1 \cdot 10^5$ frames each) for every curve shown on Fig. 4.5 and fitting them independently. The standard deviation for every parameter obtained from these subsets was taken to be the error of the whole data set ($4 \cdot 10^5$ frames).

The dipole moments in table 4.1 were obtained from Eq. 4.24 assuming the QD to be sitting in the center of a Gaussian laser focus having a FWHM of 750 nm and a pulse duration of 700 fs. We can determine the average pump powers that act like a π -pulse on the QD from the power series shown on Fig. 4.5. In the end we need the time integrated electric field of one pulse at the site of the QD which corresponds to that average power so that we can write:

$$\mu = \frac{\pi \hbar}{\int E(t) dt} \quad (4.30)$$

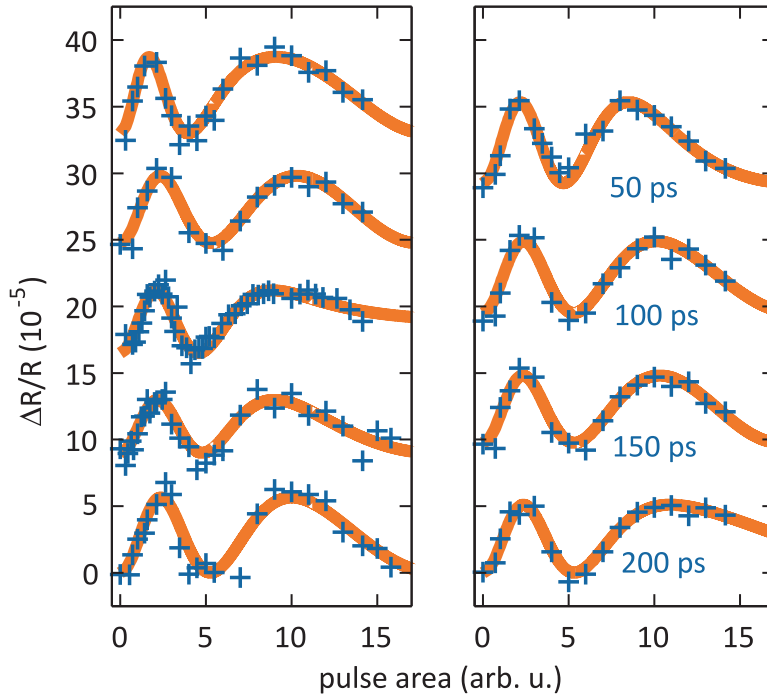


Figure 4.5: Left: Rabi oscillations measured on different QDs at $\Delta t = 150$ ps. Right: Rabi oscillations in one QD at different pump-probe delays.

dot	delay (ps)	P_{sat} (μW)	f_{sat}	μ (D)	A (10^{-5})
A1	150	126 ± 57	0.675 ± 0.040	16.8 ± 0.52	5.60 ± 0.60
A2	150	128 ± 35	0.745 ± 0.035	17.6 ± 0.58	4.73 ± 0.42
A3	150	141 ± 21	0.887 ± 0.063	17.1 ± 0.29	5.43 ± 0.16
A4	150	103 ± 36	0.651 ± 0.052	18.0 ± 0.42	5.32 ± 0.43
A5	150	53 ± 8.3	0.740 ± 0.016	18.8 ± 0.22	5.86 ± 0.24
A4	200	132 ± 11	0.784 ± 0.014	17.0 ± 0.39	5.13 ± 0.022
A4	150	103 ± 36	0.651 ± 0.052	17.1 ± 0.48	5.32 ± 0.43
A4	100	105 ± 5.5	0.653 ± 0.025	17.0 ± 0.07	5.46 ± 0.41
A4	50	209 ± 19	0.882 ± 0.048	17.4 ± 0.22	5.98 ± 0.33

Table 4.1: Numerical values for the saturation power P_{sat} , the asymptotic reduction of the Rabi frequency f_{sat} , the transition dipole moment μ and the maximum bleaching amplitude A . Statistical errors were obtained by evaluating four independent subsets for every data set and taking the standard deviation of the results for these four fits.

In a Gaussian focus the radial intensity profile is

$$I(r) = P_0 \frac{1}{2\pi\sigma_r^2} e^{-\frac{r^2}{2\sigma_r^2}} \quad , \quad (4.31)$$

so that we get the peak intensity at $r = 0$. The integral power is denoted with P_0 and the FWHM is just $\Delta r = 2\sqrt{2\ln(2)} \cdot \sigma_r$.

We consider a train of Gaussian shaped pulses with a repetition rate $\tau_{rep} = 13 \text{ ns}$ and a pulse duration of $\Delta t = 700 \text{ fs}$. The integral of $I(t)$ over one pulse is $I(r=0)\tau_{rep}T/a_{dc}$, with $a_{dc} = 0.4$ denoting the duty cycle of the AOM gate pattern (see chapter 3) and $T = 0.44$ being the combined transmission of the microscope, the cryostat window and the sample surface. This quantity can be seen as an average intensity per pulse at the center of the focal spot. The integral over intensity is now converted into the integral over electric field according to

$$I(t) = \frac{1}{2}\epsilon_0 cn E(t)^2 \quad , \quad (4.32)$$

where ϵ_0 is the vacuum permittivity, c the speed of light and n the refractive index [106]. By integrating Eq. 4.31 over time one can obtain an expression for the integral electric field in the center of the focal spot:

$$\int E(t)dt = \sqrt{\frac{P_0}{\pi\epsilon_0 cn\sigma_r^2 a_{dc}} \tau_{rep} T 2\sqrt{2\pi}\sigma_t} \quad (4.33)$$

This result is obtained using the fact, that $\sqrt{I(t)}$ has a width of $\sqrt{2}\sigma_t$. The intensity cross-correlation of pump- and probe pulses gives the FWHM of the temporal intensity profile $\Delta t = 2\sqrt{2\ln(2)} \cdot \sigma_t$.

4.5 Conclusion

In summary, we were able to record two periods of Rabi oscillations in single GaAs/AlGaAs QDs. The first period follows closely the behavior that is predicted by the optical Bloch equations for a simple two-level system. The stretching of the second period is by no means a signature of dephasing of the excitonic polarization with respect to the pump electric field. Dephasing would manifest itself in a decreasing modulation depth of the bleaching signal. We could not observe any additional pump-induced dephasing for pump powers up to $200 \mu\text{W}$ as the modulation depth stays constant for all data sets. One has to bear in mind, however, that the coherent interaction is taking place only during the absorption of the pump pulse. The probe process measures merely populations and does not strictly require any coherence between pump, exciton and probe, anymore. As we could only observe two periods due to the onset of pulse-area reduction caused by

4 Rabi oscillations in single GaAs quantum dots

excited carriers in the environment of the QD, we are unable to exclude power-induced dephasing for higher Rabi-frequencies.

Transition dipole moments could be deduced from the pump power that was necessary to prepare a complete inversion of the system. The values ranged from about 17 to 19 D, which is in good agreement with the theoretical value for GaAs considering perfect electron-hole overlap. In this case, the oscillator strength can be written as $f = E_p/2\hbar\omega$, with $E_p = 25.7 \text{ eV}$ being the Kane energy for GaAs [109, 127]. Transition dipole moments and the oscillator strength are connected by

$$f = \frac{2m_0\omega_0}{\hbar} \left(\frac{\mu}{e}\right)^2 . \quad (4.34)$$

For our GaAs QDs with a neutral exciton transition energy of 1.725 eV this yields an oscillator strength of $f = 7.4$, which corresponds to a dipole moment of $\mu = 19 D$. This shows nicely that in the QDs under investigation the case of perfect electron-hole wave function overlap is an optimum value for the transition dipole moment, which is nearly reached.

5 Ultrafast switching of excitons

The interaction between the localized exciton in a single GaAs QD and delocalized, excited charge carriers in the vicinity of the QD was studied using two-color pump-probe spectroscopy. A hot cloud of carriers is created in the GaAs substrate which is only separated from the QD layer by a 10 nm thick AlGaAs barrier. We pump the substrate selectively creating excited carrier densities of up to 10^{19} cm⁻³ and probe the QD resonantly after a variable delay time. The excited carriers thermalize on a timescale of about 50 ps and show a characteristic saturation behavior for elevated pump intensities. In the presence of the hot carrier cloud we observe a redshift together with a decrease in absorption strength of the exciton transition in the QD. Experimental data fits to a model based on the photo-Dember effect. A vertical electric field which is caused by charge separation near the substrate-barrier interface is responsible for the redshift and the weakening of the QD absorption via the quantum-confined Stark effect. We demonstrate that we are able to switch off the absorption of the dot on a picosecond timescale with recovery times of around 50 ps which are only dependent on the relaxation time of the substrate material.

5.1 Band absorption in bulk GaAs and vertical electric fields

Transient differential reflection spectroscopy allowed us to record Rabi oscillations on the neutral exciton transition in a single GaAs QD, as described in chapter 4. In the most simple case one can describe single quantum emitters as two-level systems neglecting the environment in which the emitter is situated. It became clear, however, that in our case this very harsh simplification breaks down and we have to include the electronic background of the QD's environment in order to adequately describe our data. We observed that for higher pump powers where the rotation angle of the Bloch vector exceeds the value of 2π our results deviate from the response of a simple quantum mechanical two level system. The angle of rotation was no longer proportional to the square root of the pump power but showed a stretched out shape. We explained this effect phenomenologically by an effective rotation angle (θ_{eff}) which could be expressed by the population density of delocalized hot carriers which are also excited by the pump pulses around the QD (see Eqn. 4.29). This means that there is a connection between the hot carriers around the QD and the QD's ability to interact with resonant light pulses. According to our model, the more carriers we excite near the QD, the weaker becomes the absorption in the QD. In order to gain more insight into the microscopic mechanism behind this interaction we set up an experiment where we selectively pump the GaAs substrate and probe the localized exciton in the QD with resonant pulses. In such a two-color experiment the pump pulses do not excite the QD in any way, as the photon energy is not high enough. The influence of excited carriers in the substrate on the QD's absorption can be studied directly in this manner.

In this chapter we demonstrate how the absorption of a single QD can be influenced by exciting a hot contribution of nearby charge carriers. We first introduce the interaction mechanism and discuss the spectral signature of the delocalized carriers. Modifications to the experimental setup as introduced in chapter 3 are discussed. We show that the differential reflectivity signal from the QD is the difference of a weakened redshifted absorption line and an unperturbed spectral line. This model fits very well to our spectral data by which we can demonstrate ultrafast switching of the absorption in a single QD.

5.1.1 The photo-Dember effect and ultrafast screening in GaAs

If we want to understand the role which excited carriers play in our pump-probe experiments we have to review the excitation kinetics in GaAs. We have to think about the carriers' response to an ultrafast, above bandgap pump pulse at 1.70 eV. The first process is interband absorption, which means that electrons are promoted into the con-

duction band of bulk GaAs while holes remain in the valence band. GaAs has a band gap energy of 1.52 eV at temperatures of around 10 K, so the excess energy of 180 meV is transferred to the carriers' kinetic energy according to the inverse ratio of their effective masses [128]. Electrons are promoted from the light and heavy hole bands to the conduction band and the entire population stays within the Γ -valley. Electrons from light hole bands have a kinetic energy of 103 meV, while light holes have 77 meV ($m_e^* = 0.062 m_0$, $m_{hh}^* = 0.082 m_0$). In the case of excitation from the heavy hole bands the energies are distributed less equally ($E_{\text{kin},e} = 160$ meV, $E_{\text{kin},hh} = 20$ meV, $m_{hh}^* = 0.51 m_0$). The resulting hot distribution of carriers has peaks around the pump energy and is thus far from thermal equilibrium [129].

One can measure this excited population optically by the technique of spectral hole burning [112, 130, 131]. Here, the transmission spectrum of a broad probe pulse is monitored as a function of the pump density at a controllable delay time with respect to the pump pulses. Absorption saturation at elevated pump levels leads to an excitation induced transparency of the sample at the pump wavelength. Thermalization of hot carriers due to carrier-phonon scattering causes the population to relax towards the band edge. The spectral hole shifts red and broadens with increasing delay time as the carriers cool. This process is very efficient and takes place on a sub-picosecond timescale [128, 132]. Once the thermal equilibrium has been reached electrons and holes recombine radiatively at the band edge and so return to their initial groundstates.

Photo-excited electrons have higher kinetic energies than holes due to their smaller effective mass. As a result, their initial velocity is also much higher. If a hot distribution of electrons and holes is created in the focus of a laser beam in an isotropic bulk sample the spatial arrangement of both carrier types are concentric spheres of constant excited carrier concentration. On the one hand the carriers have a certain kinetic energy depending how far away from the conduction band minimum they are created. On the other hand there is a radial density gradient in the charge cloud which causes it to expand rapidly due to radial diffusion currents. The electrons move away from the center faster than the holes as they have a lower effective mass and a higher initial kinetic energy. This leads to a charge separation with an electric field building up between areas of higher hole density in the center and higher electron density at higher distances from the focus. As the charge pattern is concentric there is no net dipole moment associated with it. Once the kinetic energy is dissipated by scattering or stored in the electric field the carriers turn around and the charge separation decays again. This situation changes drastically if we excite hot carriers in the vicinity of an interface such as the sample surface or a layer with a high band gap material. In this case the carriers can be reflected at the interface which breaks the symmetry of the charge pattern. The faster electrons will have a higher concentration further away from the interface while the slower holes stay more or less close to the interface where they have been excited. In this case the centers of charge are no longer coinciding and a net dipolemoment builds up when the hot cloud of electrons expands into the material. This phenomenon is referred to as photo-Dember effect which is observed when light is absorbed near semiconductor interfaces [133, 134].

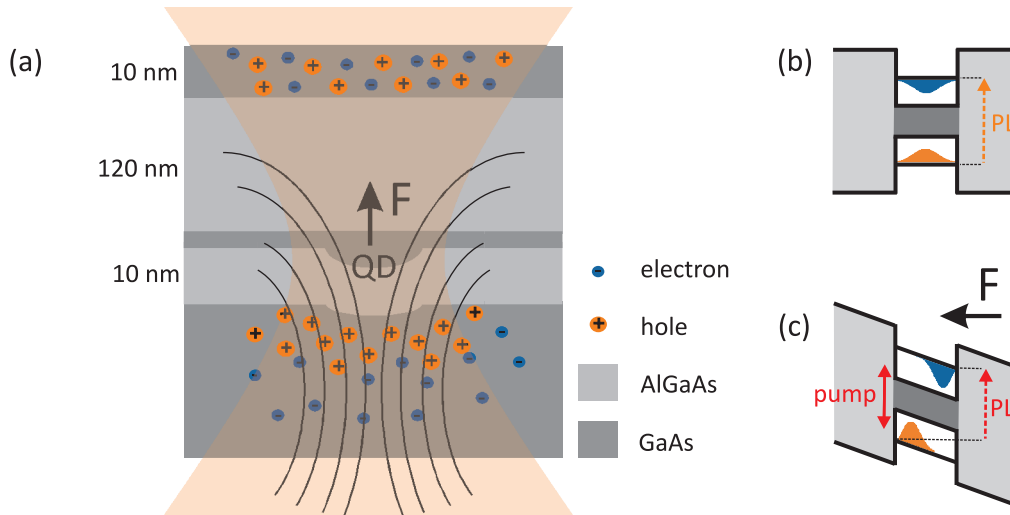


Figure 5.1: GaAs QDs between AlGaAs barriers are exposed to photo-Dember fields created by hot photocarriers at the interface of the substrate and the lower barrier (a). Due to the quantum-confined Stark effect the bound exciton transition in the QD experiences a redshift and a decreased absorption strength (b, c).

Figure 5.1a shows a sketch of this scenario for excited carriers in our sample structure as introduced in chapter 2. A pump beam excites the carrier in the GaAs cap and substrate. The cap is separated from the QD layer by the 120 nm thick upper AlGaAs barrier. The substrate, in contrast, has only a distance of 10 nm from the QD layer making the influence of its hot carriers on the QD much larger. The displacement of the centers of charge for electrons and holes as discussed above leads to the buildup of a dipolar electric field. We can simplify the geometry by assuming a capacitor with circular plates which lie underneath the QD. When the plates are infinitely large in the plane of the interface then the field is confined completely to the volume between the plates with no field leaking out. If we consider, however, the lateral extent of the capacitor (which is basically given by the spot size of the pump beam) to be finite the field lines leak out of the capacitor as sketched on Fig. 5.1(a). This leads to an electric field F which extends also into the QD layer and which is ideally normal to the interface and points upwards [135]. This electric field is referred to as photo-Dember field and it plays an important role in the generation of ultrafast THz-pulses in highly absorbing, intrinsic semiconductors [135–137]. In this context the effect was studied extensively, among other groups, by Dekorsy and coworkers. Monte-Carlo simulations were performed in order to model the response of a semiconductor crystal surface to ultrafast above-bandgap pulses. Reflective electro-optic sampling techniques [138] were used to directly measure the electric field normal to the surface. It was found that while in heavily doped semiconductors THz radiation originates mainly from ultrafast screening of built-in surface electric fields by excited carriers [139], in highly absorbing intrinsic semiconductors it is in fact the photo-Dember effect which becomes the dominating source for THz emission. Both processes involve displacement currents of optically excited carriers which build up

a vertical electric field on ultrafast timescales.

In the case of weak band-bending, where the built-in surface field is weak, electrons and holes are separated due to their differing velocities and the reflection by an interface (Dember-effect). In heavily doped semiconductors, however, charge separation in the photocarrier distribution is owed to the strong surface electric field which is then screened as the dipolar polarization builds up (ultrafast screening). For InAs/GaAs QDs grown on high index planes high built-in fields are obtained [140]. In this system dynamic lineshifts due to ultrafast screening of built-in piezoelectric fields were observed by time-resolved PL measurements [141]. The difference in the power-dependence of both cases is, that the screening effect is proportional to $N_{\text{exc}}^{1/2}$ when N_{exc} is the density of the excited photocarriers, whereas the Dember-field scales linearly with N_{exc} [142]. The polarization ΔP that results from the separation of charge carriers can be expressed as

$$\Delta P(t) = eN_{\text{ext}}(t, z)\Delta z(t), \quad (5.1)$$

where Δz is the spatial separation of the positive and negative centers of charge and e is the elementary charge.

The effects that a vertical electric field has on the absorption properties of a QD are illustrated on Figs. 5.1b and c. The potentials for electrons and holes are bent by the field and the wavefunctions are pulled apart along the growth-direction, where the confinement is strong. This causes a reduced spatial wavefunction overlap and in consequence a reduced transition dipolemoment. The optical transition is also experiencing a redshift as the maximum of the electron (hole) wavefunction will move to regions of lower (higher) potential. This phenomenon in low-dimensional semiconductors is called quantum-confined Stark effect and it has been demonstrated in GaAs quantum films [143] (confinement in one direction) and in CdSe nanocrystals [144] (confinement in three dimensions). The change in resonance energy ΔE of an optical transition in the presence of an electric field F_z can be written as

$$\Delta E = \mu_z F_z + \frac{1}{2}\alpha_z F_z^2 + \dots, \quad (5.2)$$

where μ_z and α_z are the projections along the applied field of the excited state dipole moment and polarizability, respectively. InGaAs QDs have a considerable permanent dipolemoment due to an electron-hole-separation of about 0.4 nm [145]. The hole is localized at the apex of the dot, whereas the electron wavefunction is distributed over the entire dot. This fact has been exploited by Mete Atatüre and his group to use a single InGaAs QD as a very sensitive electric field probe [12]. Houel *et al.* could demonstrate recently, that the Stark-shift in a single QD can detect fluctuations in the local electric field as hole-traps near the QD are populated under optical excitation [146].

Ranber Singh from the research group of Gabriel Bester at the Max Planck Institute for Solid State Research in Stuttgart has performed fully atomistic pseudopotential

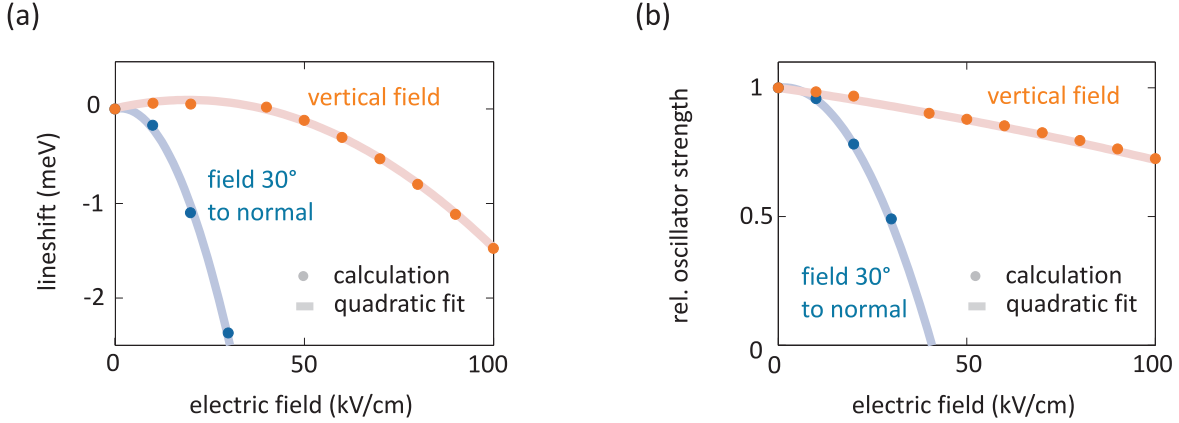


Figure 5.2: Results of atomistic pseudopotential calculations performed by R. Singh from the MPI for Solid State Research in Stuttgart. Redshift (a) and relative oscillator strength (b) as a function of electric field strength for a single GaAs QD. Results are shown for a vertical electric field (red) and a field that is tilted by 30° with respect to the vertical direction (blue). The calculations yield a polarizability of $2.4 \cdot 10^4 \text{ CV}^{-1}\text{m}^2$ for the case of a vertical electric field. In the tilted case the polarizability becomes $3 \cdot 10^5 \text{ CV}^{-1}\text{m}^2$.

calculations [147] in order to evaluate the effect of a vertical electric field on the absorption properties of a GaAs QD. The dimensions of the structure were known from AFM studies [43] on nominally identical samples. We assumed an elongated, lens shaped GaAs dot with a height of 3 nm, a length of 70 nm and a width of 50 nm. The resonance energy of around 1.72 eV for the ground state exciton transition could be reproduced in the calculations. Figure 5.2 shows the predicted redshift (a) and relative oscillator strength (b) as a function of electric field strength for a GaAs/AlGaAs QD. Results are shown for a vertical electric field (red) and a field that is tilted by 30° with respect to the vertical direction (blue). The vertical polarizability was calculated to be $\alpha_z = 2.4 \cdot 10^4 \text{ CV}^{-1}\text{m}^2$. The quadratic redshift due to the quantum-confined Stark-effect is well visible, whereas the reduction in oscillator strength is almost linear in the case of vertical electric fields. We see that relatively small fields which cause a minimal redshift of several μeV already reduce the absorption strength of the exciton transition considerably. When the electric field is not completely normal to the sample surface the polarizability increases, as the carriers are not as tightly confined in the sample plane. Our QDs are quite flat so electrons and holes have more freedom in the lateral direction as opposed to the growth direction.

Besides the predicted redshift and the decrease in oscillator strength the resonance line is also broadened due to spectral diffusion in a vertical electric field [144, 148]. The field-dependent redshift according to Eq. 5.2 is not exactly the same for each shot but distributed around a mean value. Neglecting the out-of-plane electric dipolemoment, the width of this redshift distribution $\Delta(\Delta E)$ is given by the partial derivative of the spectral shift with respect to the field $\partial(\Delta E)/\partial F_z$ and the fluctuation (standard deviation)

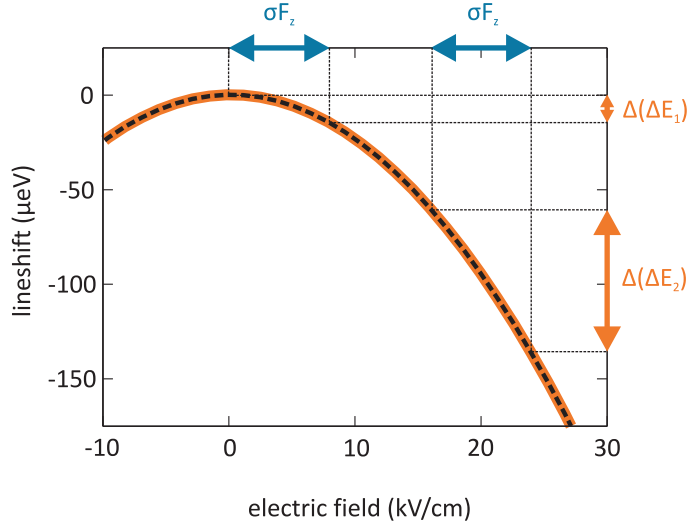


Figure 5.3: Redshift of the neutral exciton transition plotted as a function of the vertical electric field. A small variation in the local electric field σF_z causes a small broadening $\Delta(\Delta E_1)$ due to spectral diffusion for small applied electric field. For higher electric fields, however, the spectral diffusion term $\Delta(\Delta E_2)$ is much increased according to Eq. 5.3.

in the field σF_z :

$$\Delta(\Delta E) = \frac{\partial(\Delta E)}{\partial F_z} \cdot \Delta F_z = 2\alpha_z F_z \cdot \sigma F_z \quad . \quad (5.3)$$

When we decompose the electric field into an external contribution which is essentially given by the Dember-field $F_{\text{ext}} = F_{\text{Dember}}$ and internal fields F_{int} we can rewrite the above expression:

$$\Delta(\Delta E) = 2\alpha_z (F_{\text{Dember}} + F_{\text{int}}) \cdot (\sigma F_{\text{Dember}} + \sigma F_{\text{int}}) \quad . \quad (5.4)$$

One can easily see from Eq. 5.3 that the fluctuation in the local field σF_z is amplified by the pump-induced vertical field leading to a broadening of the shifted line which increases strongly with the redshift. This behavior is conceptualized on Fig. 5.3 showing the redshift as a function of vertical electric field strength for a vertical polarizability of the exciton of $\alpha_z = 2.4 \cdot 10^4 \text{ CV}^{-1}\text{m}^2$. The same fluctuation in the local vertical field of $\sigma F_z = 8 \text{ kV/cm}$ causes a broadening of only $15 \mu\text{eV}$ for small vertical fields (4 kV/cm), whereas it causes a line broadening of $77 \mu\text{eV}$ at a vertical field strength of 20 kV/cm.

In summary, high concentrations of photocarriers in the GaAs substrate modify the absorption of a QD. Vertical Dember-fields cause a redshift and a reduced oscillator strength due to the quantum-confined Stark-effect. In addition, the absorption line is broadened by spectral diffusion caused by fluctuations in the local electric field.

5.1.2 Monitoring the carrier density in the GaAs cap

Besides the above mentioned effects on the QD, carriers that have been excited by inter-band absorption in the GaAs cap and substrate alter the optical properties of the material in a broad spectral range. After thermalization we can describe the hot carrier distribution as an additional contribution ϵ_{free} to the dielectric function of GaAs ϵ_{GaAs} :

$$\epsilon = \epsilon_{free} + \epsilon_{GaAs} = -\frac{\omega_P^2}{\omega^2 + i\gamma\omega} + \epsilon_{GaAs} \quad ; \omega_P = \sqrt{\frac{ne^2}{\epsilon_\infty \epsilon_0 m^*}} \quad (5.5)$$

Here, ω_P is the plasma frequency which is given by the electron density n , the elementary charge e , the background polarizability due to the bound electrons $\epsilon_\infty = 11$, the vacuum permittivity ϵ_0 and the effective mass of the electrons $m^* = 0.067 \cdot 9.1 \cdot 10^{-31}$ kg. The damping constant $\gamma = 0.5$ ps⁻¹ does not have a large impact on the optical properties in the visible spectral range, as the plasma frequency is in the terahertz regime [149, 150]. When we assume a Lambert-Beer law of the form

$$\frac{I}{I_0} = e^{-\alpha(\omega)d} \quad (5.6)$$

for the absorption in GaAs we can estimate the density of the excited carrier cloud. Here, I/I_0 is the ratio of transmitted and incoming light, $\alpha(\omega)$ is the absorption coefficient and d is the thickness of the considered GaAs layer. At a wavelength of 720 nm the absorption coefficient of GaAs is $2 \cdot 10^4$ cm⁻¹ at temperatures around 15 K [151], which means that half the incoming power is absorbed after a thickness of 350 nm. If we consider a cylinder of 350 nm in height and 750 nm in diameter, which corresponds to the spot size of our microscope, we can estimate a mean electron-hole pair density of $1.5 \cdot 10^{24}$ m⁻³ for pulsed laser excitation with 10 μ W of average power at a repetition rate of 76 MHz. The plasma frequency is then given by Eq. 5.5 to be around 13 THz which corresponds to a photon energy of 53 meV. This means, that the excited carriers cannot screen optical fields, but they contribute as an additional term to the dielectric function of the GaAs layer according to Eq. 5.5.

Figure 5.4(a) shows the complex refractive index $\tilde{n} = n + ik$ of GaAs. The reflectivity $R_{1,2}$ from an interface between two media with complex indices of refraction \tilde{n}_i is given for normal incidence by [152]

$$R_{1,2} = \left(\frac{\tilde{n}_1 - \tilde{n}_2}{\tilde{n}_2 + \tilde{n}_1} \right)^2 \quad (5.7)$$

Reflectivities for the vacuum/GaAs interface at the sample surface and for a GaAs/AlGaAs interface such as between substrate and lower barrier are plotted on Fig. 5.4(b). One should note that the refractive indices of GaAs and AlGaAs are very similar so that these interfaces only give a minor contribution to the overall reflectivity (the black line is multiplied by a factor of 10 for better visibility). The inset shows a magnified region

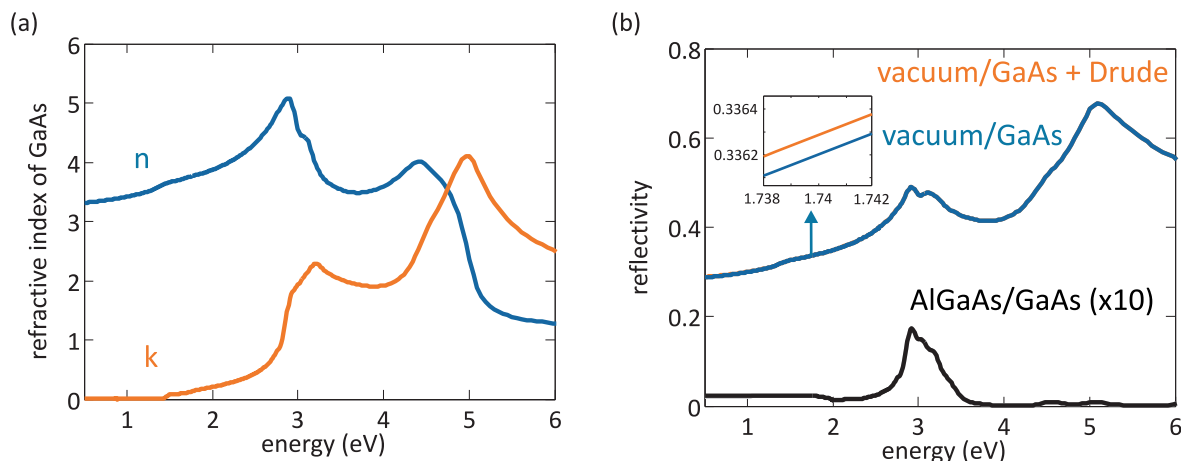


Figure 5.4: Complex index of refraction for GaAs (a). Reflectivity of an AlGaAs/GaAs interface (black line, scaled up by a factor of 10) and of a vacuum/GaAs interface (blue line) (b). The inset shows a magnified region around 1.74 eV which shows the difference in reflectivity due to excited carriers with a density of $1.5 \cdot 10^{19} \text{ cm}^{-3}$ (red line).

around 1.74 eV where the difference in reflectivity between unexcited GaAs (blue line) and a sample with an excited carrier density of $1.5 \cdot 10^{19} \text{ cm}^{-3}$ (red line) is visible. The differential reflectivity $\Delta R/R$ due to the presence of excited carriers is on the order of 10^{-4} in this case, whereas the contribution from GaAs to AlGaAs interfaces is one order of magnitude smaller. For this reason it is the carrier concentration in the GaAs capping layer that can be monitored by differential reflection measurements. The cap is only 10 nm thick, so only 2 % of the pump light is absorbed in this layer. This means we can neglect the cap as a source of photon loss while it still gives us valuable information about the carrier density in the substrate which can be assumed to be of the same magnitude as in the cap.

The differential signal is not a very strong function of the photon energy in the visible spectral range, as the plasma frequency is in the terahertz domain. An example of the broad contribution of delocalized carriers in the GaAs capping layer to a reflective pump-probe spectrum was given on Fig. 3.14. We can extract this background signal when we take the differential reflectivity in a spectral range that is well detuned from the sharp localized exciton transition in the QD (see section 3.3).

We study the decay of the background signal by varying the pump-probe delay for a constant pump power. On Fig. 5.5(a) decay traces are shown for average pump powers ranging from 0.5 to 200 μW . We can see that the photocarriers decay on a 100 ps timescale and that the decay time is not dependent on the pump power. The saturation behavior of the background signal is investigated by recording power series at a constant delay time, as shown on Fig. 5.5(b). The average pump power P is varied from 0 to 200 μW for delay times ranging from 50 to 200 ps. The signal is proportional to

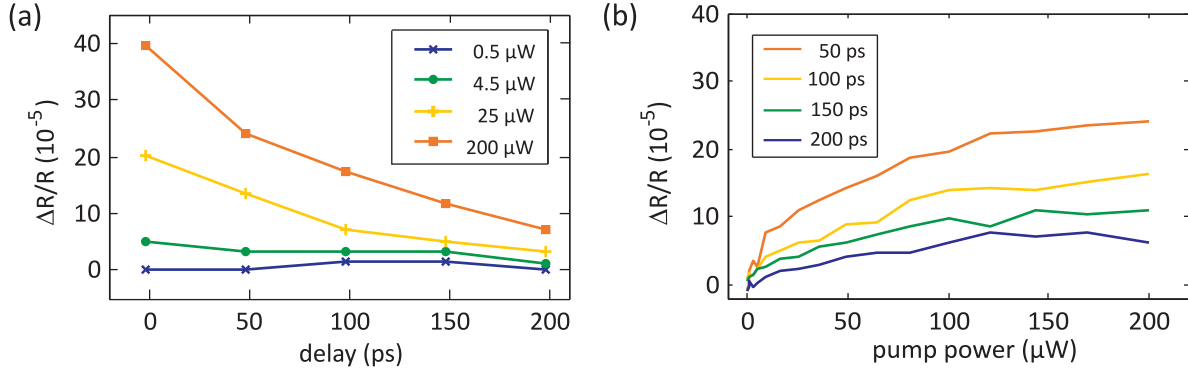


Figure 5.5: Delay series of differential reflectivity due to excited carriers in the GaAs capping layer for various pump powers (a). The hot carrier cloud recombines on a 50 ps timescale. Power series for various pump-probe delays reveal absorption saturation in GaAs (b).

the carrier concentration in the capping layer n following a typical saturation law

$$n = \frac{P/P_{\text{sat}}}{1 + P/P_{\text{sat}}} \quad , \quad (5.8)$$

There is no significant change of the saturation power P_{sat} with pump-probe delay. The overall amplitude of the saturation curve is decreasing for longer delay times, however, due to the recombination of carriers prior to the arrival of the probe pulse. Saturation powers of around 50 μW are a bit smaller compared to the ones that were used in section 4.4 on table 4.1. The reason for this small but well reproduced difference is that the background signal monitors the saturating carrier density in the capping layer, while the carrier distribution in the GaAs substrate interacts with the exciton localized in the QD. This discrepancy in saturation powers might indicate that the defect density in the substrate is higher compared to the capping layer. It has been shown for GaAs grown at different temperatures, that the samples grown at lower temperatures (higher defect density) exhibited a higher saturation power and a faster decay time of the excited carriers [126]. The fabrication process of our GaAs QDs which involves the creation of nanoholes by removing partially capped sacrificial InGaAs QDs using an AsBr etching step (see chapter 2) might be responsible for an elevated defect density in the substrate underneath the QDs.

5.2 Experimental technique

There are two basic experimental realizations which are outlined on Fig. 5.6. Our laser system was introduced in chapter 3.2.1. Here, the probe pulses are always resonant with the neutral exciton transition in the QD at around 720 nm (1.72 μeV). The two cases

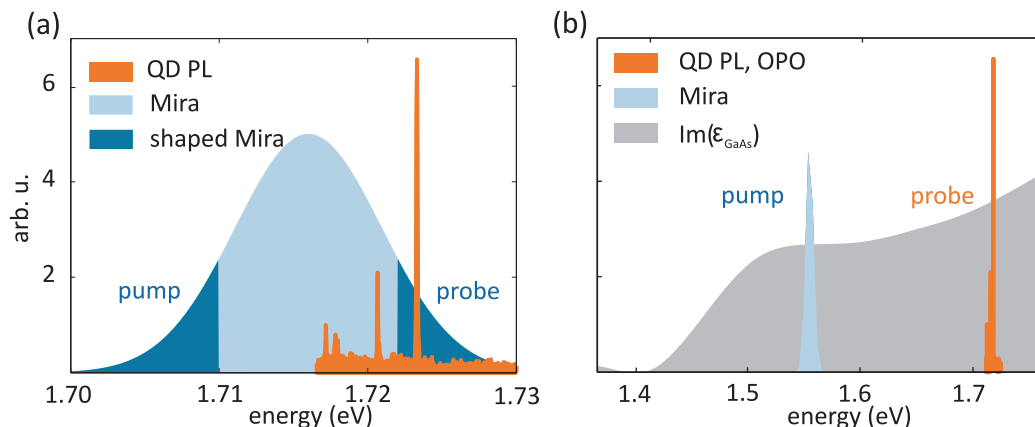


Figure 5.6: Pump and probe pulses are shaped directly out of the Ti:Sapphire spectrum (a). An OPO is employed to generate the resonant probe pulses while the GaAs substrate can be pumped with the Ti:Sapphire output directly (b).

differ in the spectral position of the pump pulses which are not resonant to transitions in the QD but only create carriers in the GaAs substrate. We can shape pump and probe pulses out of the spectrum of our Ti:Sapphire laser (MIRA) which results in pump pulses which do not differ much in photon energy from the probe pulses (a). We take the lower energy slope of the spectrum for the pump pulses so that we do not risk exciting higher states in the QD. The spectral separation is more than 10 meV in this case and the GaAs substrate is excited at 1.70 eV which is well above the bandgap energy of 1.52 eV. For this reason we can neglect the possibility that the pump beam still excites localized states in or near the QD, as higher states in the dot and the wetting layer have higher transition energies than the neutral exciton transition. Another option is to use an optical parametric oscillator (OPO) for frequency conversion as indicated on Fig. 5.6(b). Here we use the MIRA to pump the OPO at around 1.59 eV (790 nm) which is still above the band gap of GaAs. The extinction coefficient of GaAs is indicated as a gray area. The OPO delivers pulses with durations shorter than a picosecond at 1.72 eV (720 nm, red area) which we can use to probe the QD resonantly. The GaAs substrate is pumped by a split-off part of the MIRA output (blue area). Here, the difference in photon energy is above 150 meV for pump and probe pulses which also ensures that no localized resonances can be excited in the QD and the pump exclusively excites the substrate. As in earlier experiments, we record reflectivity spectra of the probe pulses and compare the case of a pumped sample to the case where the pump beam is blocked with a modulation of 1 kHz. This technique results in differential reflectivity spectra

$$\Delta R/R = \frac{R(\omega, \tau) - R_0(\omega)}{R_0(\omega)},$$

where $R_0(\omega)$ is the reflectivity spectrum without the pump beam and $R(\omega, \tau)$ signifies the reflectivity spectrum with active pump beam for a pump-probe delay τ . Differential reflectivity spectra directly reveal the influence of the hot carriers in the substrate on the QD's absorption.

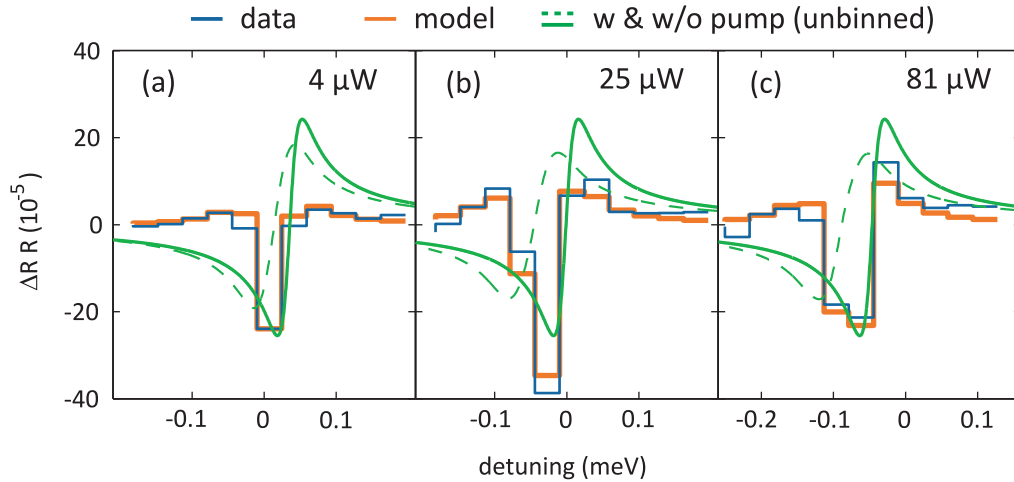


Figure 5.7: $\Delta R/R$ spectra for low power (a), intermediate power (b) and high power (c). The experimental data (blue) can be reproduced by a model (red) which consists of the difference of the unperturbed QD absorption (solid green) and the redshifted and decreased absorption of the QD due to the photocarriers in the GaAs substrate (dashed green). The increased broadening of the shifted signal at elevated pump powers is caused by spectral diffusion due to fluctuations in the local electric field.

Two-color pump-probe experiments were carried out as described above. We recorded delay series at a fixed power and power series at a fixed pump-probe delay time. In order to explain the signal shapes and the model for our spectra we want to discuss first three differential spectra taken at a delay time of 50 ps and with pump and probe pulses shaped directly out of the Ti:Sapphire spectrum as shown on Fig. 5.6(a). Figure 5.7 shows the differential reflectivity of a single GaAs QD for small pump powers (a), intermediate powers (b) and high powers (c). As $\Delta R/R$ spectra contain always the difference between the case of a pumped and an unexcited sample, we also have to include this comparison into our model. We know the width and the spectral shape of the interference of the backscattered wave from the QD and the light reflected from the sample surface from chapter 3. The solid green lines on Fig. 5.7 represent the model curve of the spectral interferogram for an unexcited substrate and the dashed green line is the case for a pumped sample where a cloud of hot carriers was generated 10 nm underneath the QD. If the pump pulses had no effect on the absorption by the QD the two lineshapes would coincide and the differential signal would vanish. From the spectrally resolved lineshape we can differentiate between signal contributions that originate in a shift of the absorption line and a change in the absorption amplitude. As we can see, the difference of these two lineshapes (red line) describes the experimental data (blue line) very well after binning to the pixels of the CCD camera. Here, the difference between the green curves was averaged over the width of one pixel in order to take the finite pixel size of the CCD camera into account. Even details such as the appearance

of little shoulders on either side of the central dip (a, b) and increasing asymmetry due to the smaller signal amplitude for higher pump powers (b, c) are clearly reproduced. The data shows a red shift together with a diminished absorption of the QD exciton in the presence of photocarriers in the substrate as predicted by the atomistic calculations which were presented on Fig. 5.2. Additionally, the pumped signal displays broadening of its lineshape due to spectral diffusion, according to Eq. 5.3. As the absorption of the pumped system gets weaker the overall differential signal is more and more dominated by the constant unperturbed (not pumped) signal and so the general shape of the signal becomes more dispersive for increasing pump powers.

For the sake of clarity we will now go over the model and all relevant parameters. As stated above, the model can be seen as the difference of an unaltered and a shifted lineshape B, which is the dispersive lineshape function introduced in chapter 3.

$$B(\delta, \gamma_0) = A \frac{\gamma_0^2}{\delta^2 + \gamma_0^2} \left(\cos 2\phi - \frac{\delta}{\gamma_0} \sin 2\phi \right) \quad (5.9)$$

It is characterized by an amplitude A, a phase ϕ_0 which determines the shape, a resonance energy E_0 for which the frequency detuning $\delta_0 = 0$ and a width γ_0 . The phase is given by the optical path between the sample surface and the QD layer and it is known together with A and γ_0 from earlier measurements (see chapter 3). The differential signal can thus be expressed in terms of the original lineshape B and a line which is reduced in amplitude by a factor a, redshifted by ΔE and which has a width γ that is increased due to spectral diffusion.

$$\Delta R/R = B(\delta_0, \gamma_0) - aB(\delta_0 + \Delta E, \gamma) \quad (5.10)$$

In order to model the experimental data we first need a factor of proportionality b between the background signal which is a measure of the carrier density n in the substrate (Eq. 5.8) Dember-field, so that $F_{\text{Dember}} = b \cdot n$. The value of the electric field then determines the redshift and the reduction in absorption strength according to our atomistic calculations displayed on Fig. 5.2. The width of the pumped line is calculated from the Dember-field and the polarizability according to Eq. 5.3 and the value for the fluctuation of the local electric field. The last parameter is the pixel offset δ_0 which determines the relative position from the center of the fixed line to the pixel grid on the CCD camera. This parameter has to be adjusted to the dataset but it bears no physical significance at all. Table 5.1 summarizes the role of each parameter and the way the values are assigned in our model. In the end, there are only two physically relevant parameters which we need to chose in order to describe our measurements. These parameters are the fluctuation of the local field σF and the ratio of carrier density and Dember-field strength b. All the other are either known, taken from calculations or merely instrumentation parameters which are dependent on the alignment.

This example already shows that we can modify the absorption properties of a single QD by exciting hot carriers in its vicinity. We can weaken the absorption strength

symbol	comment	value assigned by...
n	relative carrier density	from background signal
b	Dember-field strength per carrier density	adjusted to data
σF	fluctuation in the local electric field	adjusted to data
a	amplitude reduction due to vertical electric field	from atomistic calculations
ΔE	redshift due to vertical electric field	from atomistic calculations
δ_0	pixel offset, purely technical parameter	adjusted to data

Table 5.1: Parameters used to model differential reflectivity spectra of the neutral exciton transition when pumping the GaAs substrate.

and redshift the transition line by energies exceeding the natural linewidth. Figure 5.7(c) exhibits redshifts on the order of the width of the differential signal. It has to be noted, however, that this width is given by the resolution of our spectrometer ($100 \mu\text{eV}$) and that the natural linewidth of the exciton transition is in fact smaller. The spectral resolution of our setup is equivalent to 3 pixels on our CCD camera. Differential spectra, however, are the difference between two spectra and can exhibit features which are much sharper than the ones on a single spectrum. This can be seen very well on Fig. 5.7, where differential spectra have very sharp features which are basically just one pixel broad. In the following section we want to give a more complete picture of the switching behavior by investigating its power dependence as well as its transient properties.

5.3 Results

In this section we discuss pump-probe data for the two experimental conditions introduced above. We measured differential reflectivity spectra of the neutral exciton transition in single QDs where photocarriers are excited in the GaAs substrate using photon energies of 1.70 eV (close to the QD exciton) and 1.59 eV (just above the bandgap energy of GaAs). The influence of the carrier cloud on the QD is revealed by differential spectra as discussed on Fig. 5.7. Here, we want to present several datasets which show the pump-induced switching of a single confined exciton in the power- and in the time domain. The experimental data is reproduced well by a model which assumes the vertical Dember-field to be proportional to the carrier density in the substrate, as is expected. This means that we can model the Dember-field by a saturation law as in Eq. 5.8 for a power-dependent dataset and by an exponential decay for a delay-dependent measurement, as shown on Fig. 5.5. The only free parameters are a factor of proportionality between the photocarrier density and the strength of the Dember-field, as well as a fluctuation in the local electric field of the QD as discussed in Eq. 5.3 for the line broadening

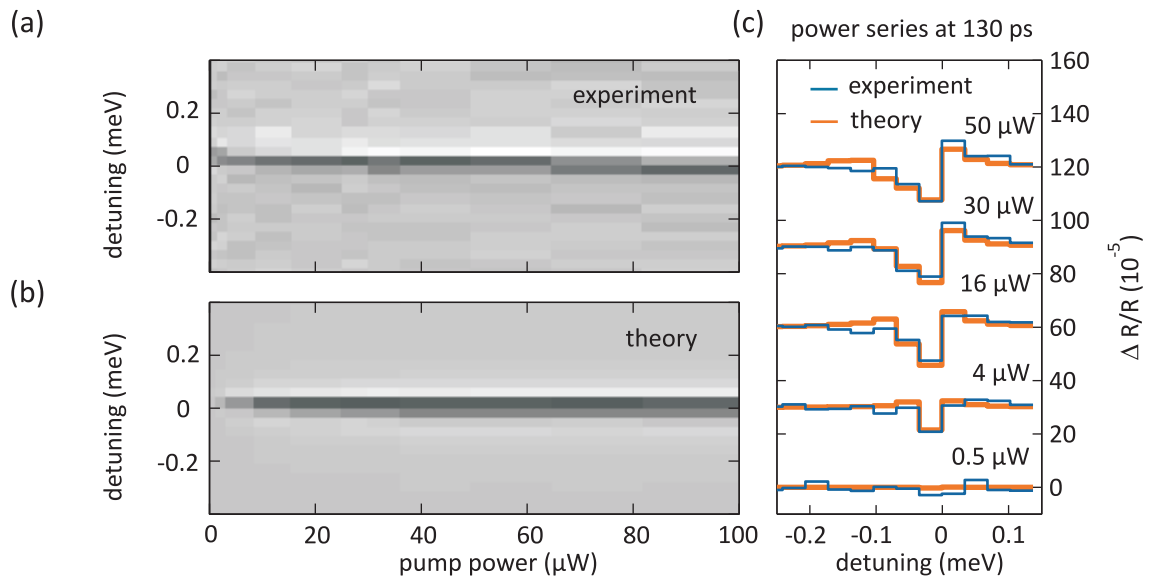


Figure 5.8: Power series at a delay of 130 ps pumped at 1.70 eV. Differential reflectivity spectra (a) are well reproduced by a model (b) assuming a vertical Dember-field which is proportional to the saturating photocarrier density in the GaAs substrate. The model involves a peak electric field of 16 kV/cm resulting in a redshift of 100 μeV and a reduction of 5% in oscillator strength, according to atomistic pseudopotential calculations. Representative spectra are displayed together with their respective model spectra (c) for several average pump powers. Curves are shifted vertically for clarity.

due to spectral diffusion. Both of these parameters can be influenced strongly by the environment of the dot and the overall purity and composition of the sample. Relative photocarrier densities (normalized to their peak-values) as a function of power or delay time are directly taken from the background signal as described on Fig. 5.5.

5.3.1 Pump 180 meV above the bandgap energy of GaAs

For the experiments where we pump well above the bandgap energy we shaped both pump and probe spectra out of the spectrum of a Ti:Sapphire spectrum, as is illustrated on Fig. 5.6(a). The photocarriers in the substrate are generated at about the same energy as in resonant experiments such as the Rabi-oscillations we presented in chapter 4. A major disadvantage of this arrangement comes from the fact that in order to ensure that the pump does not excite the QD directly but only the substrate, we need some spectral distance between the pump and the QD transitions. This means that we have to limit ourselves to the flanks of the Ti:Sapphire spectrum and that we shape out the center part of the spectrum completely. In consequence, we are severely limited in power. We are able to pump at an average power of 90 μW , while still probing at 1.5 μW .

Figure 5.8 shows a power series taken at a pump-probe delay of 130 ps. The experimental data (a) is well described by a model (b) which was introduced above. Additionally, some measured spectra are shown together with the according spectra resulting from our model (c). We can see that the differential spectrum changes in strength and in shape up to pump powers of $40 \mu\text{W}$. This observation can be understood in terms of a saturating photocarrier density as in Eq. 5.8. The carriers are the origin of the vertical electric field which thus saturates with increasing power, accordingly. The data could be reproduced by assuming a saturation power of $25 \mu\text{W}$ and a fluctuation in the vertical field of 3.5 kV/cm . For zero Dember field the intrinsic field fluctuation causes a broadening of $3 \mu\text{eV}$ by spectral diffusion according to Eq. 5.4. The value of the saturation power is identical with the one obtained from the background signal contribution from the capping layer for this dataset, as shown on Fig. 5.5(b). It should be pointed out that we did not fit each spectrum individually but rather the entire dataset is reproduced by a model involving only the above mentioned two free parameters describing the physics. Of course, there are also other experimental parameters involved which are partly known from other measurements. These parameters include the amplitude and the width of the unpumped lineshape which is known from earlier pump-probe measurements (see chapter 3 and 4). The relative spectral position of the unperturbed line with respect to the pixel borders is a pure instrumentation parameter which has a profound impact on the resulting differential lineshape and which needs to be adjusted for sensible results. It can be seen from Fig. 5.7 that this relative spectral position is crucial for the shape of the binned model signal.

For small powers the differential signal is just a sharp dip which is only one pixel wide ($4 \mu\text{W}$ spectrum). It results from a slight redshift of the exciton line due to the quantum-confined Stark-effect. With increasing pump power the redshift also increases and a stronger vertical electric field also broadens the line (spectral diffusion) and decreases the oscillator strength of the transition. These effects can be seen in the broader differential signal and the flatter slopes on the low-energy side of the spectrum ($16\text{-}50 \mu\text{W}$ spectra). For the highest pump power of $100 \mu\text{W}$ we achieved a Dember-field strength of 16 kV/cm at the position of the QD which caused a redshift of $100 \mu\text{eV}$, a reduction in oscillator strength of 5% and a broadening of the lineshape of $9.5 \mu\text{eV}$.

An important result is that our model, in which the vertical Dember-field is linearly proportional to the photocarrier density in the GaAs substrate, reproduces the experimental data extremely well. The fact that both the background signal from the capping layer and the Dember-field in our model have the same saturation power is a reassuring sign. Now, we want to exploit the full power of our time-resolved spectroscopy technique and record the differential absorption signal of the exciton line as a function of delay time. In this way we can literally watch how the absorption line is altered by the buildup of an electric field and how it returns again to the unperturbed line as the field decays.

The outcome of such a delay series pumped at $9 \mu\text{W}$ is displayed on Fig. 5.9 in the

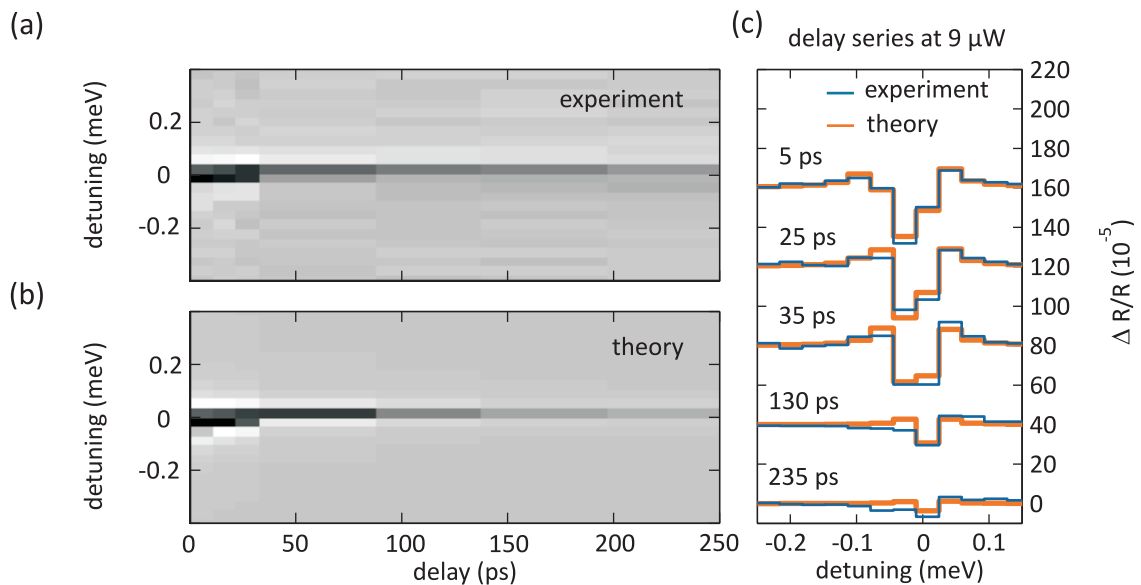


Figure 5.9: Delay series at an average pump power of $9 \mu\text{W}$ at 1.70 eV . Differential reflectivity spectra (a) are well reproduced by a model (b) assuming a vertical Dember-field which is proportional to the exponentially decaying photocarrier density in the GaAs substrate. The model involves a peak electric field of 13 kV/cm resulting in a redshift of $70 \mu\text{eV}$ and a reduction of 4% in oscillator strength, according to atomistic pseudopotential calculations. Representative spectra are displayed together with their respective model spectra (c) for several pump-probe delays. Curves are shifted vertically for clarity.

same manner as the power series, above. We can see very clearly here that the differential signal is very strong for small delays and it decays, just as the background signal on Fig. 5.5(a), on a 50 ps timescale. In our model for the spectra displayed on Fig. 5.9(b) the Dember-field is treated as an exponential decay which assumes half its peak value after 50 ps. The fluctuation in the vertical electric field was assumed to be 1.5 kV/cm , for this dataset. The redshift is nicely visible by a broader differential signal in the presence of a dense photocarrier cloud for short delay times.

This measurement shows that we can redshift the exciton transition in a single QD by more than the natural linewidth and decrease the absorption strength by several percent on an ultrafast timescale. The QD returns into its original state on a picosecond timescale as the photocarriers in the substrate recombine. The fall time of the switching process seem only to be limited by the recombination time of the substrate material which indicates a potential for an even faster recovery of the system.

5.3.2 Pump 7 meV above the bandgap energy of GaAs

Even though we kept a spectral distance of 10 meV to the lowest transitions in the QD for all measurements presented in the previous section, the possibility of exciting defect states in the wetting layer or in the environment of the QD can not be excluded. We can perform an even cleaner two-color pump-probe experiment by lowering the pump photon energy so that it is just above the GaAs bandgap energy. In this way we can minimize the possibility of exciting anything but bulk GaAs in the sample structure. For this reason we choose an optic-parametric oscillator (OPO) in order to generate probe pulses which are resonant to the neutral exciton transition in the QDs while we pumped the GaAs substrate with the output of our Ti:Sapphire laser at 1.59 eV which is also used to pump the OPO (see chapter 3.2.1). Now, the substrate is pumped at only 7 meV above its bandgap energy which also results in less thermal energy being transferred to the crystal. As the parametric process is very efficient and we do not have to use grating pulse shapers, we can reach average pump powers exceeding 300 μW in this configuration. It should be noted that the results in this section were obtained from a different QD as the ones from above.

Experiments similar to those presented in the previous section were performed for lower pump energy, as described above. We also recorded differential absorption spectra as a function of power and delay time. Figure 5.10 shows a power series measured at a fixed pump-probe delay of 50 ps for pump powers up to 250 μW . The modeling was performed in the same way as presented above with a Dember-field saturating at an average pump power of 50 μW and an electric field fluctuation of 5 kV/cm. Here, our model describes the experimental data with a peak electric field of 28 kV/cm causing a redshift of 166 μeV , a reduction in absorption strength of 6% and a line broadening of 63 μeV .

A comparison of the two pumping arrangements yields a generally similar behavior. The basic trend is the same, as we start with a rather narrow dip at low pump powers which eventually broadens. The differential spectrum develops into a dispersive line-shape for high pump powers which is basically given by the unperturbed absorption line. This can be understood by recalling that the differential spectrum is always the difference between reflection spectra in which the pump beam is blocked or impinging on the sample (see chapter 3). When the absorption line in the signal spectra is broadened and redshifted by the pump pulse it does not contribute as strongly to the differential spectrum which is dominated by the unchanged line from the reference spectra. A comparison with Fig. 5.8 also shows some differences. On the one hand, changes in the spectrum generally occur at higher pump powers, as the photocarriers have less initial kinetic energy and the Dember-effect is thus less pronounced for comparable pump powers. On the other hand, the saturation power is roughly twice as high as in the case presented in the last section. One has to bear in mind that we sample a single QD and its environment in a laser focus of about 800 nm in diameter. As a result of the small

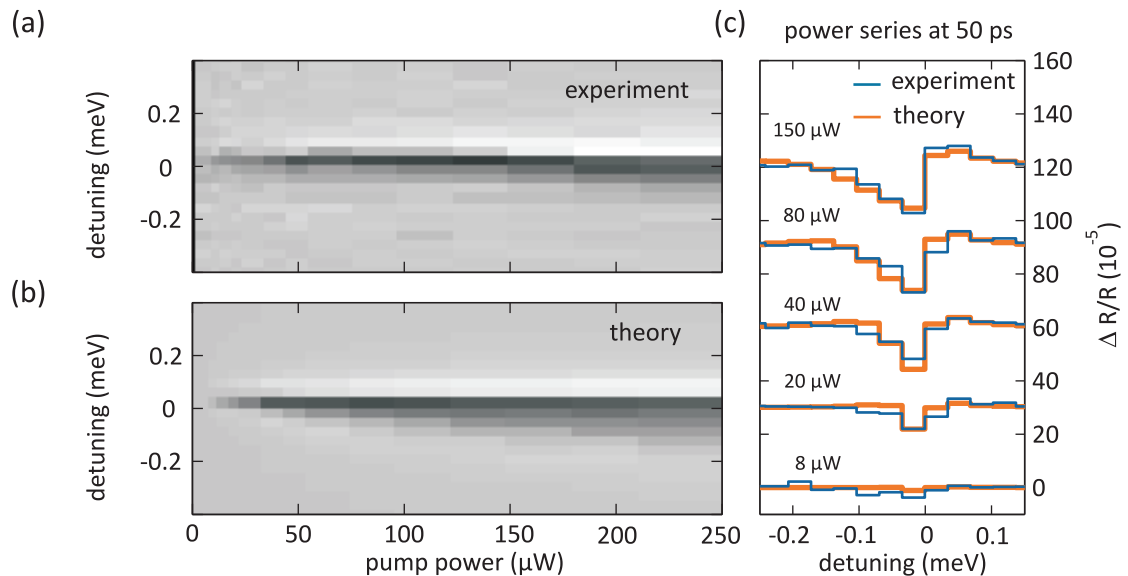


Figure 5.10: Power series at a delay of 50 ps pumped at 1.59 eV. Differential reflectivity spectra (a) are well reproduced by a model (b) assuming a vertical Dember-field which is proportional to the saturating photocarrier density in the GaAs substrate. The model involves a peak electric field of 28 kV/cm resulting in a redshift of 166 μeV and a reduction of 6% in oscillator strength, according to atomistic pseudopotential calculations. Representative spectra are displayed together with their respective model spectra (c) for several average pump powers. Curves are shifted vertically for clarity.

sampling area a considerable variation in the local environment (defects, wetting layer thickness, shape of the nanohole, etc.) is to be expected.

A delay series using pump pulses at 1.59 eV and an average power of 55 μW is displayed on Fig. 5.11. Also in this case our model is able to reproduce all experimentally observed spectral features perfectly. The agreement in model and experimental data seen especially well on the 0 ps spectrum on subframe (c). Here, the redshifted and broadened line for small delays leads to a dispersive differential feature with a very shallow red flank and a broad shoulder extending up to 200 μeV on the low-energy side of the zero-detuning position. Both the background signal from the cap and the Dember-field in our model decay with a half-life time of around 50 ps. The intrinsic vertical electric field fluctuates with an amplitude of 5 kV/cm in our model for this dataset. The highest field of 24 kV/cm is, of course, reached at zero time delay resulting in a redshift of 140 μeV and a reduction in oscillator strength of 6%. The broadening due to spectral diffusion of 58 μeV is comparatively high in this dataset.

In summary, switching experiments at a pump energy of 1.59 eV show the same trends as at higher pump energies. The main difference is seen in the fact that higher pump-powers are required to cause a certain vertical electric field. A probable explanation for

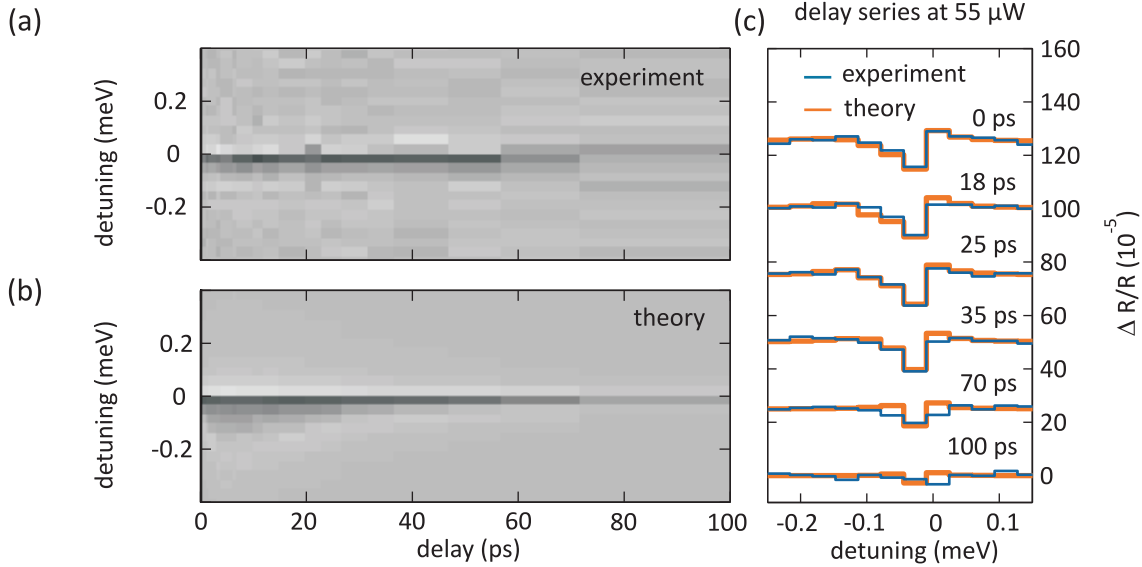


Figure 5.11: Delay series at an average pump power of $55 \mu\text{W}$ at 1.59 eV . Differential reflectivity spectra (a) are well reproduced by a model (b) assuming a vertical Dember-field which is proportional to the exponentially decaying photocarrier density in the GaAs substrate. The model involves a peak electric field of 24 kV/cm resulting in a redshift of $140 \mu\text{eV}$ and a reduction of 6% in oscillator strength, according to atomistic pseudopotential calculations. Representative spectra are displayed together with their respective model spectra (c) for several pump-probe delays. Curves are shifted vertically for clarity.

this observation is the lower initial momentum of generated photocarriers resulting in lower diffusion currents and consequently in a smaller Dember-field for a certain carrier density.

5.4 Conclusion and outlook

We demonstrated in this chapter that we are able to switch the absorption line of a single GaAs QD by all-optical means on an ultrafast timescale. The switching mechanism is based on transient photo-Dember fields which are created by a dense cloud of photocarriers in the substrate layer situated 10 nm below the QDs. Photocarriers were excited by interband absorption in bulk GaAs in two pumping configurations. In one case the pump photon energy is just slightly lower than the neutral exciton transition in the QD (1.70 eV) and in the second case we pump just above the band edge of GaAs at 1.59 eV . We obtained lower saturation powers for high photon energies and also higher vertical fields already at lower pump powers, compared to the low energy pump scenario.

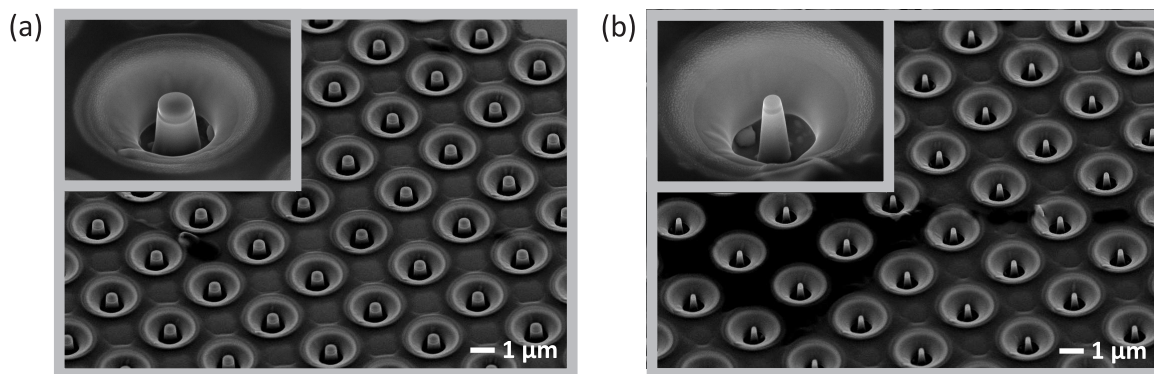


Figure 5.12: Scanning electron microscope image of micropillar structures fabricated by focused ion beam milling using Ga ions. For pillars with diameters lower than the spot size of our optical microscope (750 nm) we expect increased leakage fields at the position of the QD. This should already be the case for 500 nm wide pillars (a), but we can also fabricate smooth structures as narrow as 200 nm (b).

The QD's reaction to vertical electric fields is governed by the quantum-confined Stark-effect. This interaction was modeled by Ranber Singh and Gabriel Bester who performed atomistic pseudopotential calculations for our system. These calculations give quantitative results for the field-dependent vertical polarizability and for the reduction of the oscillator strength of the neutral exciton transition in an ideal QD. Realistic dimensions for the QDs were obtained from AFM-studies on nominally identical samples.

The absorption line can be redshifted in this system by more than the natural linewidth but it is sensitive to fluctuating local charges which results in a broadening. For the field strengths that were realized in our experiments the reduction in absorption strength is measurable but ranges in the lower percent range. The vertical electric field which mediates the switching process is built up on a sub-picosecond timescale and exhibits recovery times which are basically given by the carrier recombination time in the substrate material (50 ps in our case). This opens up opportunities for improvement, as GaAs which is grown at low temperatures is known to have drastically shorter recombination times. While carriers recombine with a half-life of about 50 ps in our samples which were grown at 500° C, the carrier lifetime can be reduced to values below 1 ps for growth temperatures of around 200° C [153]. Saturation powers can also be significantly higher than in GaAs which is grown at higher temperatures [126]. This would mean, that more dense carrier clouds can be created before absorption saturation sets in. This will result in higher Demmer-fields allowing for larger pump-induced redshifts and eventually drastically reduced oscillator strengths of the exciton transition in the QD.

We are also currently investigating the option to create high aspect ratio micropillars on high density QD samples. In such a structure where the interface between the substrate and the lower barrier would be in the middle of a pillar the effective lateral

extent of the photocarrier cloud is given by the diameter of pillar. If we perceive the distribution of electrons and holes as a plate capacitor, as introduced in Sec. 5.1.1, we see that there are more field lines leaking out from between the plates for smaller plate diameters. We already tried to fabricate pillars having diameters smaller than the spot size of our microscope by focused ion beam milling. A scanning electron microscope image of such a structure is shown on Fig. 5.12. Here, the structures are milled out of the material using a focused beam of Ga ions. We fabricated pillars of various diameters such as 500 nm (a) and 200 nm (b). At the foot of the pillars one can see pieces of deposited gallium and ablated ejecta mixed with gallium are also deposited at the fringe of the depression around the pillar. Overall, the pillars appear very smooth and regular. The next step in this project will be to find suitable QDs in the middle of a pillar structure and repeat the experiments described in this chapter. We are expecting to see stronger vertical fields for thinner pillars due to the limited lateral extent of the photocarrier cloud in the GaAs substrate. Alternatively, micropillars could be fabricated by electron-beam lithography followed by dry etching as is done in the group of Alfred Forchel at the university of Würzburg [154].

6 Coherent beats in a single GaAs quantum dot

We optically prepare an entangled superposition of the fine-structure split neutral exciton states in a single GaAs quantum dot using a broad band resonant pulse. The time evolution of the excitation in the quantum dot is read out by transient differential reflection spectroscopy. The nonradiative Raman coherence between the two exciton states becomes manifest in quantum beats which are superimposed on the radiative decay of the exciton population. From the damping time of the quantum beats ($T_{\text{Raman}}=90$ ps) we can estimate the pure dephasing time to be around $T_{\text{pure}}=150$ ps.

6.1 Introduction

In the following chapter we want to shed more light on the coherent properties of GaAs quantum dots. As the coherent aspect of the presented Rabi oscillations is limited to the interaction between the pump light and one exciton transition we did not yet discuss coherences in the matter system by itself. We showed, however, in chapter 3 that time resolved perturbed free induction decay (PID) agrees with a dephasing time of around 90 ps. The PID dataset was, however, not very sensitive to the dephasing time of the exciton, so that the uncertainty for this value can be assumed to be quite large. As introduced in chapter 2, the crystal ground state and the fine-structure split neutral exciton transitions form a V-type system. Both bright exciton transitions are optically coupled to the groundstate, while the population transfer between them requires a spin-flip process and is therefore very slow. It is known from the literature [155] that coherent superposition states of both exciton states can be excited. The mutual coherence between these orthogonal states (Raman coherence) can be measured by recording quantum beats originating in the frequency difference of the involved transitions. This coherent effect becomes manifest in transient PL measurements as an oscillating feature which is superimposed to the normal decay trace. In our case, we detect this oscillating signal component in the amplitude of the transient differential reflectivity from a single QD [156]. Quantum beats between the light- and heavy hole excitons in bulk GaAs were recorded by Ferrio and co-workers using time resolved differential transmission [157]. In inhomogeneously broadened QD ensembles quantum beats can be used to measure the FSS in the time domain [158]. The Raman coherence time of an entangled superposition state of the orthogonal neutral exciton transitions in CdSe QDs [159, 160] and in InAs QDs [155] were determined via the damping of the quantum beat signal. Quantum beats have also been successfully applied to determining the electron g-factor in InP QDs while the exciton fine-structure splitting (FSS) was varied by an external magnetic field [161, 162].

We will first introduce entanglement in two-qubit systems. The complete polarization-resolved PL characterization of the GaAs QD which was used for the experiments covered in this chapter is presented. Furthermore, the experimental details concerning the preparation of an entangled state and its detection are discussed. Finally, we present transient differential reflectivity spectra exhibiting quantum beats from an entangled exciton state.

6.2 Entangled two-qubit states

When we consider the two exciton states of the fine-structure doublet we can see them as two qubits. The combined system can be characterized by states $|00\rangle$, $|10\rangle$, $|01\rangle$ and

$|11\rangle$, signifying the groundstate, the two orthogonal excitons and the biexciton, respectively. We can also excite linear combinations of the above states, such as the Bell state $|\phi\rangle = 1/\sqrt{2}(|10\rangle + |01\rangle)$ [160]. Bell states are basic examples for entangled states in a two-qubit system.

More generally, a state is an entangled state when it cannot be written as a product state of the two qubits. Consider the states $|\psi\rangle_A$ and $|\psi\rangle_B$ for qubits A and B. A state of the combined system $|\psi\rangle_{AB} = \sum_{i,j} c_{ij} |i\rangle_A \otimes |j\rangle_B$ is an element of the Hilbert space $\mathbf{H}_A \otimes \mathbf{H}_B$. The state is called separable, if $c_{ij} = c_i^A c_j^B$, meaning that the compound state can be written as a product state of the two single qubit states $|\psi\rangle_A = \sum_i c_i^A |i\rangle_A$ and $|\psi\rangle_B = \sum_j c_j^B |j\rangle_B$ [163]. If $c_{ij} \neq c_i^A c_j^B$ the state is called inseparable or entangled.

If one performs a one-qubit measurement on each subsystem (A and B) for the Bell state given above, the result will be random for each series of measurements. One can not determine entanglement from only one single qubit measurement. The entanglement manifests itself in correlations between both series of measurement. If system A is measured and found in the state $|1\rangle_A$ that implies that state B is $|0\rangle_B$. This phenomenon, which is also referred to as the collapse of the wavefunction, does not occur in a mixed state.

6.3 Photoluminescence characterization of the quantum dot

In this section we present PL data of a single QD in order to characterize the system in which we perform coherent experiments. We chose a dot that has a comparatively large FSS of around $100 \mu\text{eV}$ which is about the spectral resolution of our experiment. In this case we can easily determine the FSS from polarization resolved PL spectroscopy as introduced in chapter 2. Here, we place a $\lambda/2$ -plate and a polarizer in front of the monochromator and record PL spectra while rotating the waveplate. In this manner only light of a certain linear polarization direction can pass the optical elements. This analysis is shown for the dot that was used throughout this chapter on Fig. 6.1. Carriers are excited in the sample by a continuous laser at 532 nm. Electrons and holes relax into the QD potential and recombine radiatively. The complete dataset is shown on Fig. 6.1a where each line is a PL spectrum for a certain rotation angle of the $\lambda/2$ -plate. Subfigure (b) shows two representative spectra as indicated by the dashed lines in (a). (c) shows a close-up view of the neutral exciton line (X) which clearly exhibits a FSS leading to an oscillating pattern of the maximum emission as a function of the direction of the detected polarization. We fit the PL data using a Lorentzian lineshape (d) which yields a FSS of $97 \mu\text{eV}$.

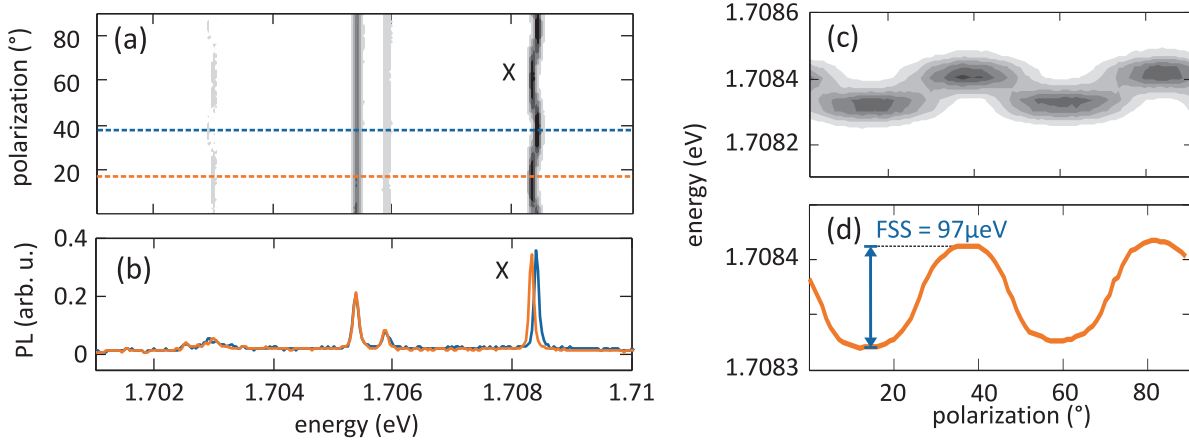


Figure 6.1: Polarization resolved PL characterization of a single quantum dot reveals the fine structure of the neutral exciton. Complete dataset (a), two representative spectra (b) as indicated by the dashed colored lines on (a), close-up view of the neutral exciton transition (c), and the peak position of a Lorentzian fit (d) to the PL data shown on (c).

6.4 Coherent beats in a single quantum dot

In chapter 4 we presented experiments where a pump pulse creates a coherent superposition of the ground state $|00\rangle$ and the exciton state $|10\rangle$. The population which remains after the interaction with the pump pulse is read out after a delay time Δt using a resonant probe pulse. Fig. 6.2(a) shows the differential reflectivity spectrum in this case when the orthogonal transition is probed. We see exactly one dispersive feature from bleaching of the probed transition as described above. By rotating the polarization of the pump beam by 45° (see Fig. 6.3a) we can create a coherent superposition of the two bright exciton states $\alpha|10\rangle - \beta|01\rangle$ (see Fig. 6.3b), the so called Raman coherence [155]. As the transition energies differ by the FSS the resulting state will exhibit a beating with just this frequency difference. We probe the evolving superposition state with an orthogonally polarized probe pulse as a function of the pump-probe delay Δt . An example of a typical $\Delta R/R$ -spectrum for this configuration is shown on Fig. 6.2b. We can identify two overlapping dispersive features as both transitions can absorb pump and probe pulses. So we measure a bleaching signature for each of the two neutral exciton transitions. Although the FSS energy can not be determined as accurately from differential reflectivity measurements as from PL data we can still see that the datasets agree quite well with each other in terms of the FSS energy. The lineshape that was used to fit the differential data on Fig. 6.2b (red line) actually contains two lineshapes as in (a) with the splitting that was determined from the PL measurements presented above. The experimental setup and the formation and detection of the differential signal was already discussed in chapter 3.

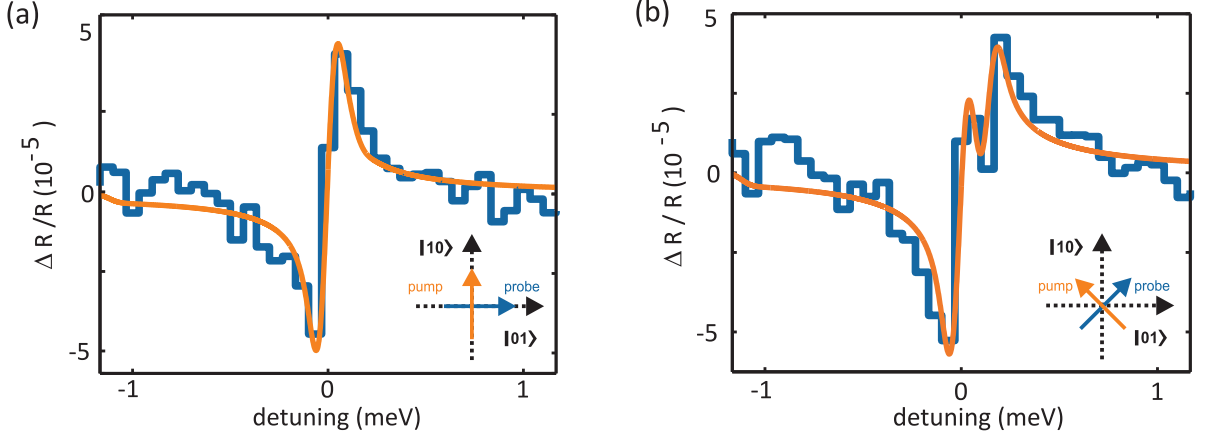


Figure 6.2: Differential reflectivity spectra (blue step plot) and fit (red line) when pump and probe beams are polarized so that they interact with one exciton, each (a). Pump and probe are rotated by 45° so that they both interact with both excitons (b). The two fine-structure split transitions are both clearly visible in (b), whereas in (a) only the probed transition gives a signal.

The excitation and readout processes can be described in terms of quantum-mechanical superpositions and projections. In the following, we neglect for simplicity the population that is left by the pump-pulse in the ground state $|00\rangle$. We also neglect the population in the biexciton state $|11\rangle$ as the biexciton binding energy (6 meV) is large enough to bring the exciton-biexciton transition out of resonance with the pump laser. At a time $t = 0$ we create an entangled superposition state $|\psi(0)\rangle = |-\rangle = 1/\sqrt{2}(|10\rangle - |01\rangle)$. The state evolves in time as

$$|\psi(t)\rangle = 1/\sqrt{2} (e^{i\omega_1 t}|10\rangle - e^{i\omega_2 t}|01\rangle) \quad (6.1)$$

$$= 1/\sqrt{2} e^{i\omega_1 t} (|10\rangle - e^{i\omega_{12} t}|01\rangle), \quad (6.2)$$

where $\omega_{1,2}$ are the angular frequencies of the two excitonic transitions and ω_{12} is their difference frequency.

After the pump-probe delay time Δt we probe the polarization of the excited dipole along the polarization axis of the probe pulses, which corresponds to a state $|+\rangle = 1/\sqrt{2}(|10\rangle + |01\rangle)$ in the exciton basis. The probe projects $|\psi(t)\rangle$ onto $|+\rangle$. The probability of finding $|\psi(t)\rangle$ in the probe polarization direction is

$$\begin{aligned} |\langle\psi(\Delta t)|+\rangle|^2 &= \langle\psi(\Delta t)|+\rangle\langle +|\psi(\Delta t)\rangle \\ &= (1 - e^{-i\omega_{12}\Delta t}) \frac{1}{4} (1 - e^{i\omega_{12}\Delta t}) \\ &= 1 - \frac{1}{2} \cos(\omega_{12}\Delta t). \end{aligned} \quad (6.3)$$

We thus can expect a $(1 - \cos(\omega_{12}\Delta t)/2)$ beating in a series of transient reflectivity

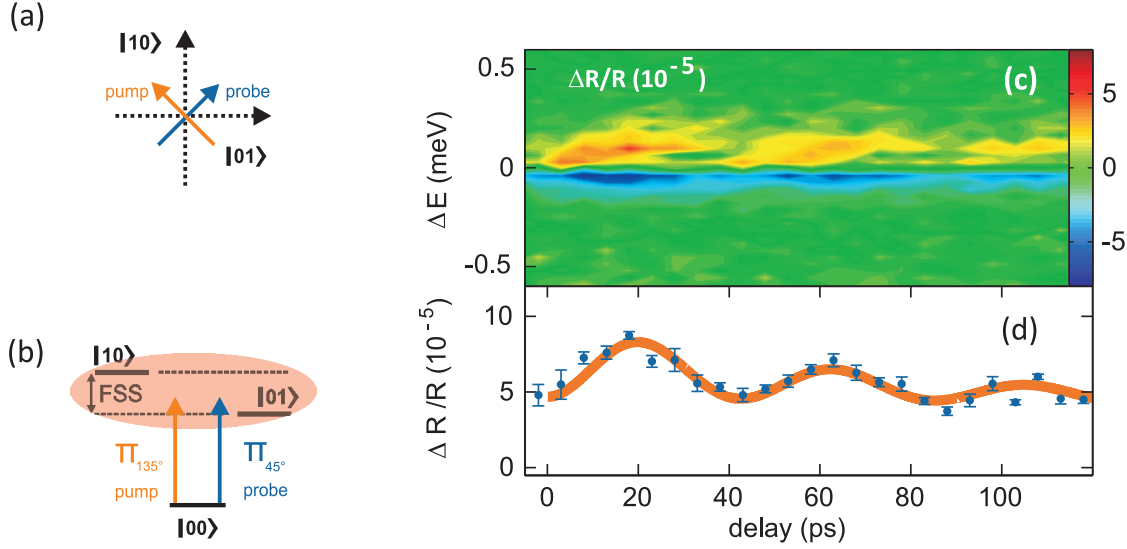


Figure 6.3: Pump and probe fields are oscillating in planes which are tilted 45° against the axes of the exciton polarizations. In this way a coherent superposition state is excited (b). Raw data of the $\Delta R/R$ spectra as a function of pump probe delay (c). Signal amplitudes of the excitonic state (blue dots) have been extracted from the spectral data by a least square fit (see Fig. 6.2) assuming two transition lines with a difference in energy equal to the FSS (d). The transient can be fitted by a population decay with a time constant T_{pop} superimposed with quantum beats having a damping time T_{Raman} . (red line)

spectra when varying the pump-probe delay Δt .

Let us now turn to the experimental realization. Both pump and probe pulses were adjusted to a pulse area of $\pi/2$ which corresponds to an average pump power of $1.5\mu\text{W}$. The transient $\Delta R/R$ spectra shown as a spectral map on Fig. 6.3c reveal three quantum beats. The two overlapping spectral signatures of both excitonic transitions were fit by two equally strong lines at a fixed separation. The amplitude of this spectral signature is obtained for each pump-probe delay Δt and depicted on Fig. 6.3d. It can in turn be fitted by assuming that not for all pump cycles a coherent superposition was reached. We carry out the experiment on a single dot but not with a single pump event. The pump-probe experiment is repeated at a frequency of 76 MHz so that we deal with a time ensemble of pump cycles rather than with an ensemble of many individual QDs in the focal area. Within this time ensemble we have now cases where a coherent superposition of both exciton states is prepared, but we also have the cases where the coherence of the laser was not transferred to the matter system and a mixed state was created. The coherent superposition state shows the beating that decays with a characteristic Raman coherence time T_{Raman} . The rest of the time ensemble just was excited either to $|10\rangle$ or $|01\rangle$, followed by a population decay with a time constant T_{pop} . The sum of both

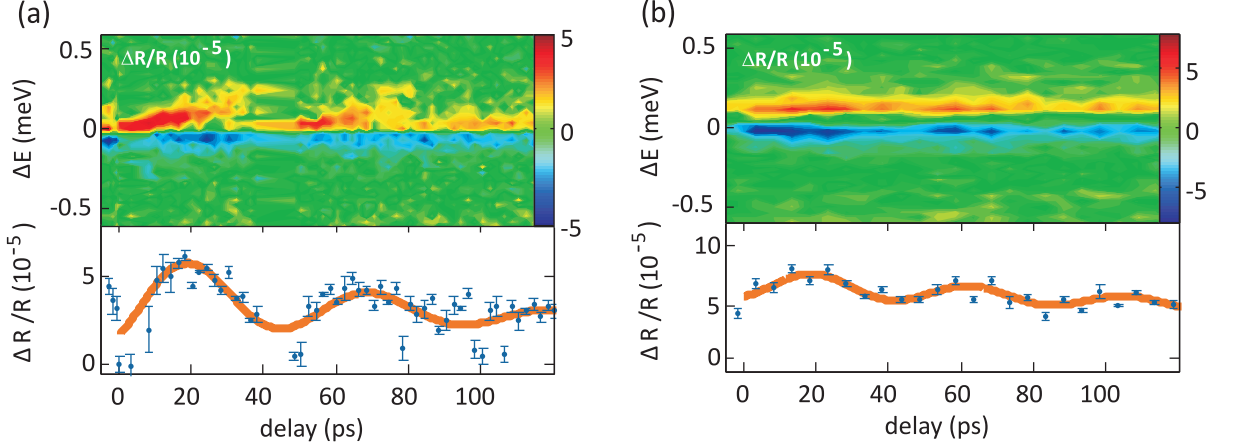


Figure 6.4: Additional datasets for quantum beats. While the signal is rather poor on (a), the quantum beat signature in the cleaner dataset (b) resembles very much the one displayed on 6.3.

contributions yields the signal:

$$\Delta R/R = ae^{-\Delta t/T_{\text{pop}}} + b(1 - \cos(\omega_{12}\Delta t)/2) e^{-\Delta t/T_{\text{Raman}}} \quad (6.4)$$

The amplitudes extracted from the $\Delta R/R$ spectra are described very well by this model, as can be seen by the good agreement of the data points and the least square fit (red line on Fig. 6.3d). We find $T_{\text{pop}} = 230$ ps and $T_{\text{Raman}} = 90$ ps. The beating period corresponds to $\hbar\omega_{12} = 96 \mu\text{eV}$ which is very close to the FSS of $97 \mu\text{eV}$ determined by photoluminescence. From the Raman coherence time T_{Raman} and the population decay time T_{pop} we calculate [160] the pure dephasing time of the coherent polarization to about $T_{\text{pure}} = (T_{\text{Raman}}^{-1} - T_{\text{pop}}^{-1})^{-1} \approx 150$ ps.

If we treat the excited state $|\psi\rangle = C_{00}|00\rangle + C_{01}|01\rangle + C_{10}|10\rangle + C_{11}|11\rangle$ as a pure state we can quantify the degree of entanglement (E) using the entropy of entanglement (S) of one subsystem alone [164].

$$E(|\psi\rangle) = S(\rho_A) = S(\rho_B) \quad , \quad (6.5)$$

with the von Neumann entropy $S(\rho) = -\text{Tr}(\rho \log_2 \rho)$. The reduced density matrix ($\rho_{A/B}$) is obtained by calculating the partial trace for the whole system over the degrees of freedom of subsystem B/A (A and B signify the two excitonic qubits):

$$\rho_A = \text{Tr}_B |\psi\rangle\langle\psi| \quad (6.6)$$

We assume that the two single exciton states are always equally populated by the pump pulse and that the biexciton state can be neglected as discussed above. As the polarization direction of the pump beam is tilted 45° against the exciton axes, each exciton sees $1/\sqrt{2}$ -times the electric field as in the case where both axes are aligned. This means that

dataset	T_{beat} (ps)	E_{FSS} (μeV)	T_{pop} (ps)	T_{Raman} (ps)	T_{pure} (ps)
Fig 6.3	43	96	230	90	150
Fig 6.4b	43	96	350	110	160
Fig 6.4a	46	90	300	54	66

Table 6.1: Numerical results for the presented datasets showing quantum beats. While the first two sets ($\pi/2$ -pulse) are fairly similar, the third one (π -pulse) deviates substantially which is also owed to the high amount of noise in the data.

for an average power that would correspond to a $\pi/2$ -pulse in collinear pump geometry (as shown on Fig 6.3), we obtain populations of

$$C_{01}^2 = C_{10}^2 = \frac{\sin^2(\pi/(4\sqrt{2}))}{2} \approx 0.14 \quad , \quad (6.7)$$

so that we excite the state $|\psi_{\pi/2}\rangle = 0.85|00\rangle + 0.37|01\rangle + 0.37|10\rangle + 0.0|11\rangle$. The density operator is in this case given by:

$$\rho_{\pi/2} = |\psi_{\pi/2}\rangle\langle\psi_{\pi/2}| = \begin{pmatrix} 0.72 & 0.32 & 0.32 & 0.00 \\ 0.32 & 0.14 & 0.14 & 0.00 \\ 0.32 & 0.14 & 0.14 & 0.00 \\ 0.00 & 0.00 & 0.00 & 0.00 \end{pmatrix} \quad (6.8)$$

The partial trace ρ_A is then just

$$\rho_A = \begin{pmatrix} \rho_{\pi/2}(1,1) + \rho_{\pi/2}(2,2) & \rho_{\pi/2}(1,3) + \rho_{\pi/2}(2,4) \\ \rho_{\pi/2}(3,1) + \rho_{\pi/2}(4,2) & \rho_{\pi/2}(3,3) + \rho_{\pi/2}(4,4) \end{pmatrix} = \begin{pmatrix} 0.86 & 0.32 \\ 0.32 & 0.14 \end{pmatrix} \quad (6.9)$$

After diagonalization of ρ_A , we calculate according to Eqn. 6.5 an entropy of entanglement of $E \approx 0.14$.

In order to achieve a higher degree of entanglement we have to use more pump power, as a Bell state of $E=1$ has $C_{01} = C_{10} = 1/\sqrt{2}$. Figure 6.4a shows such an attempt for a π -pulse. Here, we ideally prepare a wavefunction $|\psi_{\pi}\rangle = 0.44|00\rangle + 0.63|01\rangle + 0.63|10\rangle + 0.0|11\rangle$ with an entropy of entanglement of $E=0.73$. The data is clearly more noisy as the previously discussed dataset which is partly due to the shorter integration time for this measurement. Maybe hot delocalized carriers that were discussed in chapter 4 already affect the coherence of the excited state for these moderate pump powers of $4.0 \mu W$. Figure 6.4b shows an additional dataset with a $\pi/2$ -pulse taken from the same QD as the data presented above.

Table 6.1 contains the fit parameters for all presented datasets modeled according to 6.4. One can see that the extracted parameters agree very well for the $\pi/2$ -pulses (first two lines), whereas the more noisy dataset deviates quite strongly. It is also noteworthy,

that the pure dephasing time is much shorter in the case of higher pump power. The quantum beats are damped much stronger in the case of a π -pulse, as a consequence. This might be an indication for the introduction of additional dephasing channels in the presence of delocalized charge carriers close to the QD. A dataset with a pump power of $7.0 \mu\text{W}$ ($\theta \approx 1.7 \pi$) was recorded but it showed no quantum beats anymore (not shown).

6.5 Conclusion

To sum up, we recorded quantum beats between the fine-structure split neutral exciton states by transient reflection spectroscopy. Both transitions are excited equally by resonant pump pulses that are linearly polarized along a direction at 45° with respect to the axes of the excitonic dipoles. The data could be fitted by an exponential decay superimposed with a damped oscillation. The period of this oscillation was identified as the reciprocal frequency difference of the two excitonic states that could be determined by polarization-resolved PL spectroscopy. From the damping rate we determined dephasing times of around 150 ps for a pump pulse area of $\pi/2$ and 66 ps in the case of a π -pulse. In any case, the pure dephasing time is always smaller than the population relaxation time in our experiments. This means that the coherence time is not limited by the population lifetime of the exciton and pure dephasing can not be neglected in our system. As a rough estimate for the degree of entanglement in the system we calculated the entropy of entanglement. Here, we neglected the population in the biexciton state as the biexciton binding energy is quite large compared to the spectral width of pump- and probe pulses which are resonant to the neutral exciton transitions. We also assumed the transition dipole moments of the two neutral exciton transitions to be equally strong resulting in equally populated states. When we prepare the system using a $\pi/2$ -pulse we can achieve a degree of entanglement of $E \approx 0.14$, whereas a π -pulse excites a state with $E \approx 0.73$. We want to stress that the above mentioned calculation is based on a wavefunction that we did not determine experimentally. We assumed a density matrix as an idealized response to the pump pulses. The full density matrix can be experimentally determined using quantum state tomography [86, 165]. In order to prepare Bell states having an entanglement of unity one must use higher pump powers. Our samples seem not to be suited for this purpose, as the relatively short distance of 10 nm between the QD and the GaAs substrate is posing a serious problem for the state preparation at elevated powers. Hot, delocalized charge carriers are formed in the substrate and perturb the exciton state in the QD.

7 Spectroscopy of lateral InGaAs quantum dot molecules

Lateral quantum dot molecules promise a scalable approach to quantum registers. The individual neutral exciton states can be controlled by a lateral bias voltage. In this way radiative emission of localized excitons can be switched between the two quantum dots in the molecule. Here, we report on coherent absorption spectroscopy of a single quantum dot molecule. By transient reflection spectroscopy we demonstrate that not only the emission but also the absorption switches from one dot to the other when varying the applied electric field. This result is consistent with Rabi oscillations showing a radically suppressed dipole moment for the non-emitting exciton transition.

7.1 Introduction

Self-assembled quantum dot molecules (QDMs) were studied extensively in recent years due to their potential application as basic building blocks in quantum computation [166] and as tunable single-photon sources [99]. Individual neighboring quantum dots are coupled in a controlled way by shifting their excitonic states with gate electrodes via the Stark effect. Vertically arranged QDMs [167–169] make the application of individual electrodes technologically demanding and the upscaling to larger quantum registers problematic. An attractive alternative are laterally coupled quantum dot molecules [170,171]. Their planar geometry allows for coupling in two directions and makes upscaling of the system conceptually straight-forward. Connections between individual QDMs can be realized by plasmonic wires [172] and waveguides [24].

While a signature of the coupling between the quantum dots in the QDM is observable in steady-state photoluminescence, an application of the QDM in the field of quantum computing requires ultrafast spectroscopy [86]. All operations on the quantum register need to be completed within the coherence time of the quantum dot which is typically in the order of some tens to hundreds of picoseconds [91,173]. In this chapter we present ultrafast transient reflection spectroscopy [174] on a single InGaAs quantum dot molecule.

This chapter is organized as follows: After introducing our quantum dot molecules, linear optical spectra are presented and a model that is able to describe these findings is briefly summarized. Then we turn to coherent experiments on a single QDM by demonstrating Rabi oscillations on one of the exciton transitions. We also present a comparison between the bias-dependent emission and absorption properties, obtained from photoluminescence and transient reflection measurements on the same QDM [175]. Finally, we show a selection of bias-dependent PL data that are not in agreement with current models and assumptions. The presented data, which is by no means uncommon for our sample, illustrates the fact that the structure and its optical properties are not fully understood yet.

7.2 Fabrication and processing

Samples presented in this chapter were grown in the group of Armando Rastelli and Oliver Schmidt from the *Institute for Integrative Nanosciences* in Dresden. Lateral InGaAs QDMs were fabricated by molecular beam epitaxy in combination with AsBr₃ in situ selective etching of buried sacrificial InAs QDs [176]. AFM images and schematic sketches (side-view) from different stages of the sample growth are displayed on Fig. 7.1. First a GaAs substrate with stepped mounds is created by overgrowth of high density InAs QDs. Now a sacrificial dot layer is grown where InAs dots form preferentially at

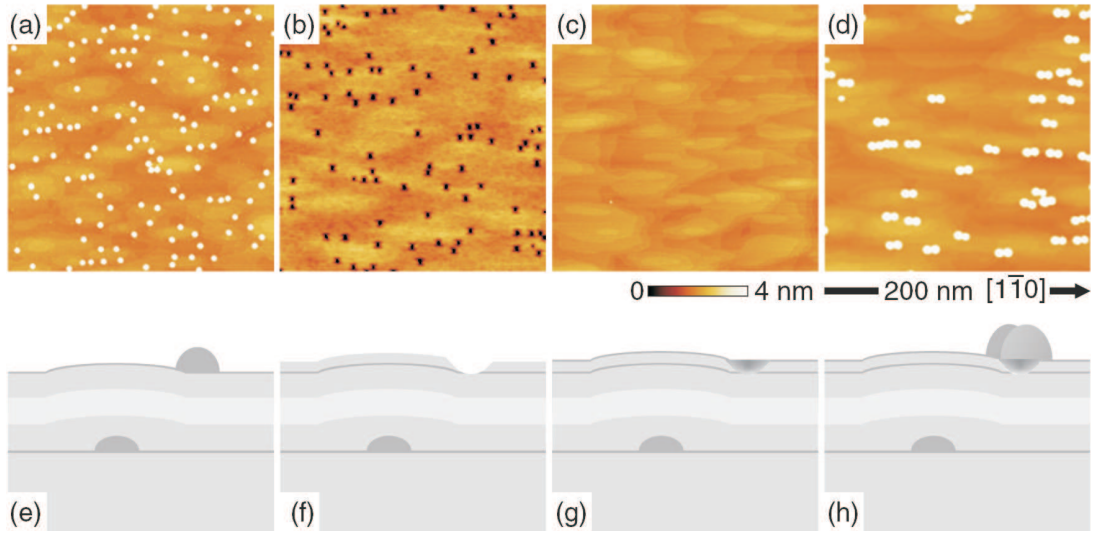


Figure 7.1: AFM images of (a) sacrificial InAs QDs grown on a non-flat surface over stepped mounds formed by overgrown InAs QDs, (b) nanoholes, (c) nanoholes filled with 1ML of InAs and (d) InAs QDMs form around the filled nanoholes (basins) when more InAs is evaporated. Figures (e)–(h) show the corresponding schematics of the sample in the $[110]$ direction. Reproduced after Ref. [170]

the edges of the mounds (Fig. 7.1(a, e)). After overgrowth with 10 nm of GaAs the sacrificial InAs QDs are removed by AsBr_3 etching resulting in bowtie shaped nanoholes in the GaAs surface at the positions of the removed dots (b, f). Growing 1.8 monolayers of InAs on top of the nanoholes creates InGaAs QDMs which are aligned in the $[1\bar{1}0]$ crystal direction (d, h). The sample is now finished by applying a GaAs cap. For a more detailed description of the sample growth see Ref. [170] and references therein. Quantitative results on the QDMs' morphology were obtained by selective wet chemical etching and atomic force microscopy (AFM) [177]. The GaAs cap was removed from the structure so that the height, the diameter and the edge-to-edge distance of the QDs could be measured. Statistical analysis of numerous single QDMs yielded dimensions of 2-3 nm in high, about 40 nm in diameter and an inter-dot distance of 2-12 nm.

In order to control the emission and absorption of the QDMs we apply external electric fields along the molecular axis using an gold electrode structure applied by photolithography. We use a series of interlacing finger electrodes of alternating polarity as shown on Fig. 7.2(a). A voltage source is connected to the upper and lower combs of the electrode structure resulting in relatively uniform electric fields along a direction normal to the fingers. Figure 7.2b shows a scan of the sample surface recorded with a standard confocal PL microscope excited into the wetting layer at around 860 nm (1.44 eV). The image reveals PL from single QDMs at 920 nm (1.35 eV) located between the gold electrodes. The suppression of reflected excitation light was just chosen so that the electrodes are still visible as bright vertical stripes. The gap between two neighboring electrodes (d) is 10 μm wide so that a bias voltage (U) of 1 V corresponds roughly

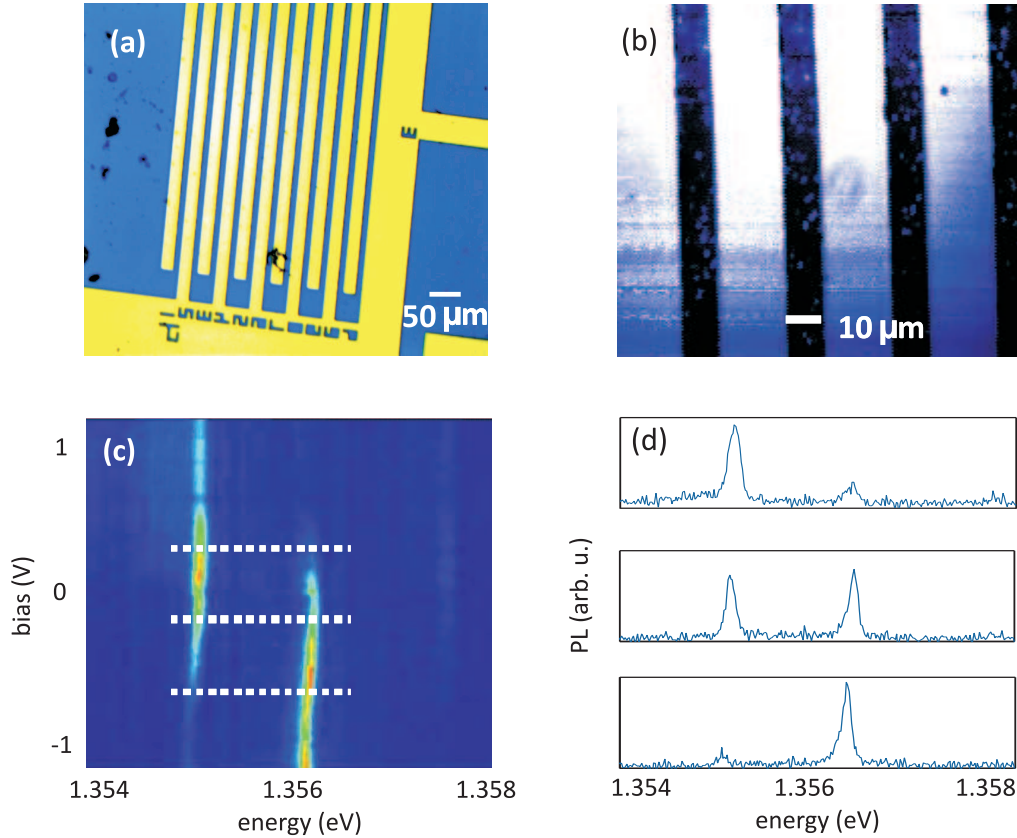


Figure 7.2: a: Reflection microscope image of the electrode structure. Interlacing Au-fingers that are contacted with an external voltage source provide lateral electric fields. b: Combined confocal PL and reflection microscope image revealing single QDMs between the finger electrodes. c: PL emission is tuned by a lateral bias voltage from one dot to the other. d: Cuts through the spectral tuning map as indicated on (c).

to a field strength $\mathbf{F} = U/d$ of ± 10 kV/cm. A demonstration of the QDMs' tunability can be seen on Fig. 7.2(c). As the bias voltage is tuned from 1 V to -1 V we measure PL spectra where only the lower energy exciton, both excitons or only the higher energy exciton are emitting.

7.3 Linear optical properties

Before performing ultrafast experiments on a QDM it was characterized by standard micro-PL measurements. The experimental setup is basically the one described in 3. As the transition energies of the QD's s-shell is lower in the InGaAs material system as compared to the GaAs structures described earlier, refractive optics had to be ex-

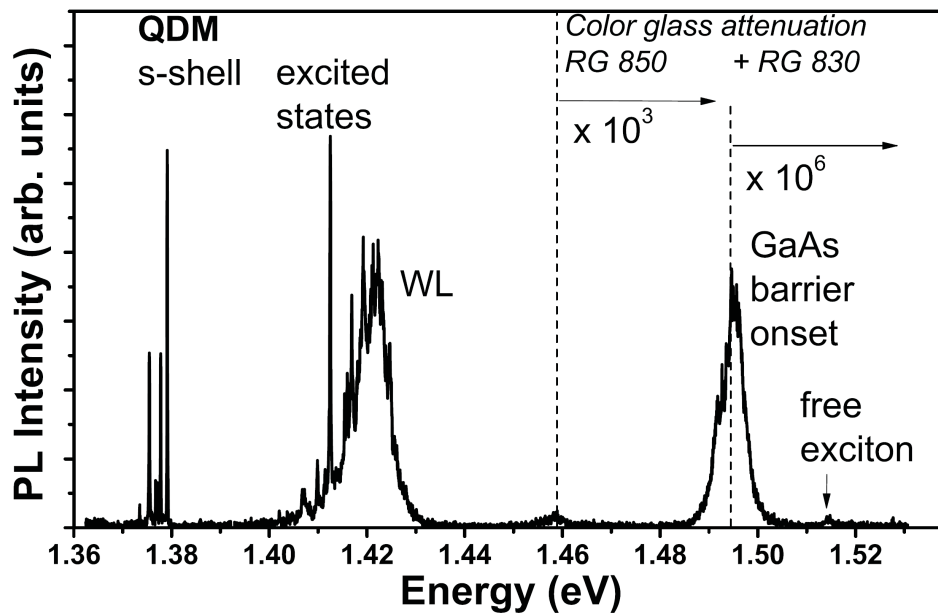


Figure 7.3: PL emission spectrum of a single InGaAs QDM nonresonantly excited at 1.55 eV. The s-shell of the QDM is energetically the lowest group of transitions which emit at around 1.38 eV. Wetting layer states (WL) are at higher energies around 1.42 eV, followed by bulk GaAs PL. Color glass longpass filters have been utilized in order to reduce the bulk contribution to the intensity level of the emission from the localized states. Reproduced after Ref. [178]

changed. For experiments on QDMs lenses with an anti-reflection coating for the near infrared and a microscope objective which is optimized for the infrared spectral region (*Olympus*, LCPlan N IR, 50x, NA 0.65) were used.

Figure 7.3 shows the PL emission of the structure in a wide spectral window at 4.2 K. This measurement was performed by Claus Hermannstädter at the *Institut für Halbleit-optik und Funktionelle Grenzflächen* of the university of Stuttgart [178]. The sample was excited nonresonantly at 1.55 eV. We can see contributions directly from the QDM such as the s-shell at around 1.38 eV and excited states at higher transition energies. The InAs wetting layer has its emission maximum at 1.42 eV and photoemission from bulk GaAs sets in from 1.48 eV. Longpass color glass filters were used in order to attenuate the emission from the bulk material which is much stronger than the emission from the nanostructure. All PL measurements presented in the following part of this chapter were carried out with quasi-resonant excitation into the wetting layer maximum. Compared to the case of nonresonant excitation above the GaAs band edge, excited photocarriers relax more efficiently into the QDM which results in clearer spectra at lower excitation densities. For the three bias regimes outlined on Fig. 7.2(c) we examined the excitation power dependence of individual emission lines in order to identify their origin. Excitonic

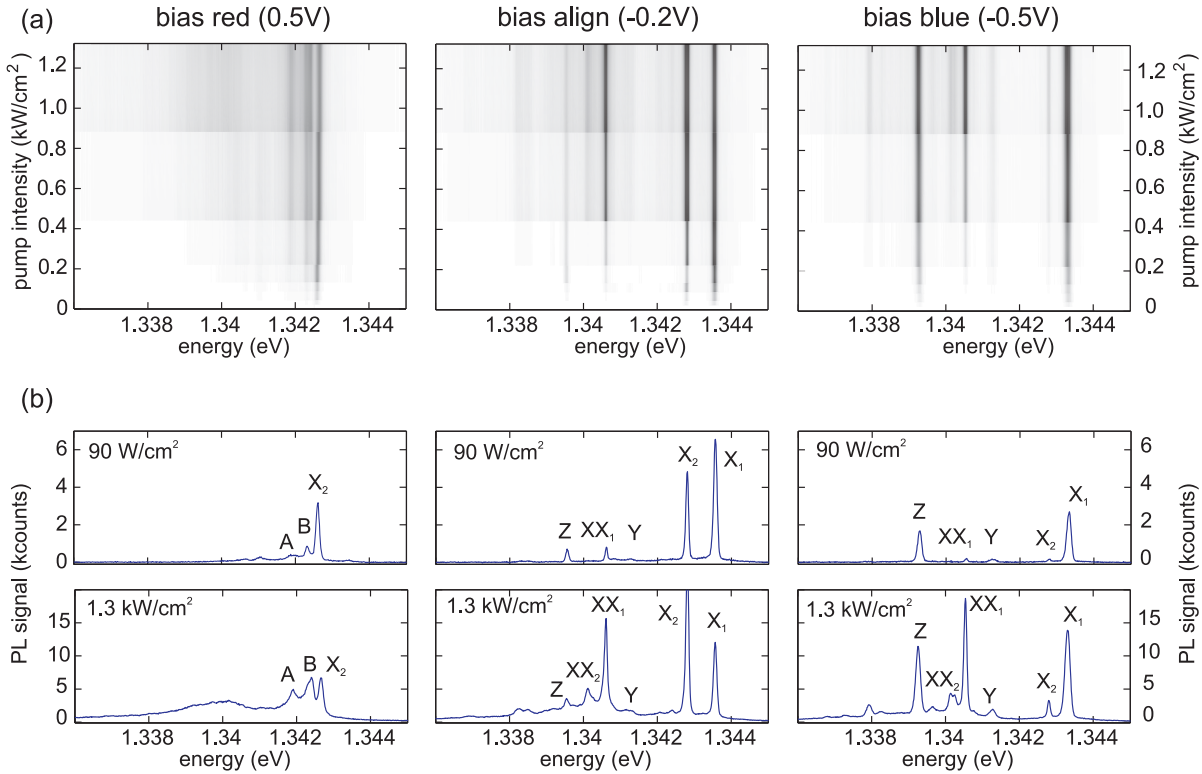


Figure 7.4: a: Powerseries for bias voltages of 0.5 V, -0.2 V and -0.5 V. b: Example spectra for low and high excitation density including labels of observed transitions. A broad background feature on the low energy side of the exciton lines is very pronounced for the positive bias regime. Well-defined single lines can be obtained for higher pump powers in the negative bias range.

and biexcitonic transitions should have a linear and a superlinear dependence on pump power, respectively. The spectral maps for a bias voltage of 0.5 V (red exciton emits), -0.2 V (alignment bias) and -0.5 V (blue exciton emits) are displayed on Figure 7.4(a). Plots (b) show example spectra for low and higher power including labels for the observed transitions. Finally, Fig. 7.5 are double logarithmic plots of the integral PL emission from the most prominent spectral features in the three power series. We can identify the two neutral single exciton transitions ($X_{1,2}$) as the two lines having the highest transition energy and a linear power dependence. Clearly, two lines show a quadratic power dependence and are thus attributed to biexciton-exciton transitions ($XX_{1,2}$) which are shifted about 2.5 meV to the red from their respective exciton-groundstate transition. Two additional transition lines (Y, Z) can not be properly attributed. For positive bias voltages we observe a broad background on the low energy side of the exciton lines for elevated pump powers, whereas we can still record well-defined single lines in the negative bias regime. Two rather broad transitions (A, B) with linear power dependence appear in this bias region slightly redshifted with respect to X_2 .

Overall, our linear PL characterization is confirming main results of earlier work on

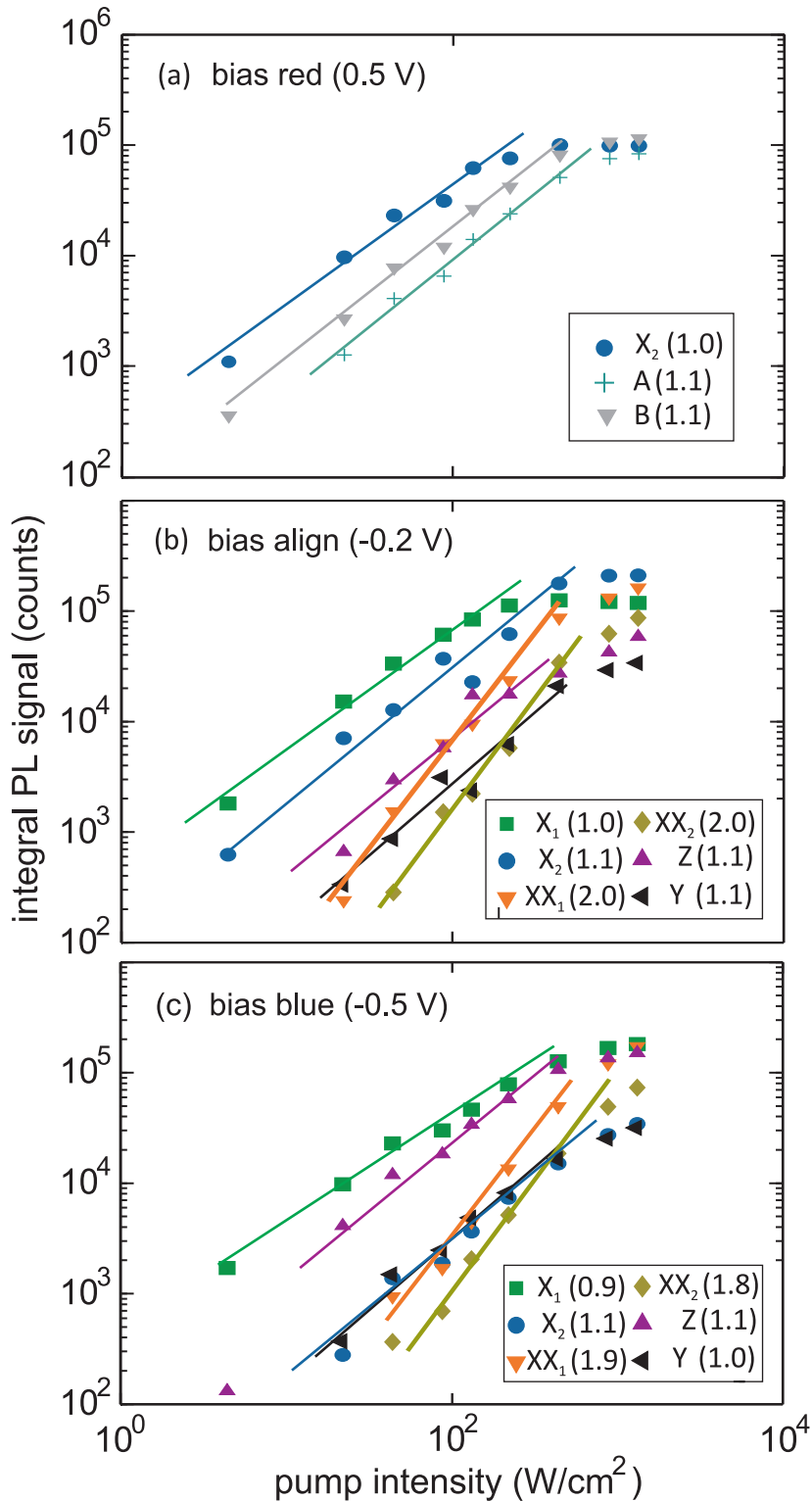


Figure 7.5: Double-logarithmic plots of integral PL emission of prominent spectral lines for the three bias regimes displayed on Fig. 7.4. Excitonic ($X_{1,2}$) and biexcitonic transitions ($XX_{1,2}$) can be identified by their power-dependence.

similar samples [100]. These results can be explained by a kinetic model for electrons and holes which are nonresonantly excited in the wetting layer and relax separately into the QDM. Time-resolved experiments on GaAs quantum wells showed that nonresonantly excited charge carriers must cool down for several picoseconds before they can form excitons [179, 180]. We can also assume that electrons relax into the QDM before the holes due to their higher mobility.

This model has been confirmed by atomistic empirical pseudopotential calculations [147] in the group of Gabriel Bester (*"Theory of Semiconductor Nanostructures"*, Max Planck Institute for Solid State Research, Stuttgart) and by PL spectroscopy in the group of Peter Michler (*"Institut für Halbleiteroptik und Funktionelle Grenzflächen"*, University of Stuttgart) [181]. Based on detailed morphological studies [170] an atomistic model of the structure including two dots and an In-rich basin was created. It was found that the single particle heavy hole states are confined to either the left or the right dot within the molecule and thus have a negligible inter-dot tunneling rate. The electrons, however, do not see two independent dots but a connected structure that is linked by the basin. They can tunnel quite freely from one dot to the other and will in turn always assume the position of the lowest absolute potential in the QDM. Consequently, we can distinguish between three bias regimes depending on the position of the electron prior to radiative recombination and emission of a photon. Figure 7.6 summarizes the kinetic model for nonresonant excitation for three bias regimes. The single particle hole wavefunctions are localized at one dot in the molecule. Electron wavefunctions have significantly higher probability amplitudes at potential minima and they are delocalized over the whole structure when the external electric field (F) aligns electron energy levels in both dots ($F=F_e$). As only direct excitons have a high rate of radiative recombination (bright excitons) we can only detect a photon when the electron and the hole are localized in the same dot. That means that the localization of the electron prior to exciton formation determines the dot out of which we can detect photoemission for a given external field. In consequence we see that emission from both dots is possible when the electron is delocalized over the whole QDM, whereas only one bright exciton can be formed for fields differing from the alignment field F_e . This part of the theoretical description can fully explain the presented PL measurements. Another prediction from the atomistic model is concerned with the absorption spectrum of the QDM. The absorption lines for both direct neutral excitons are expected to be both visible and equally strong, independent of the external electric field. This aspect of the model has not been confirmed as no experimental data on the QDMs' absorption exists, so far. We set out to test this prediction by measuring the absorption of the QDM by differential reflection spectroscopy.

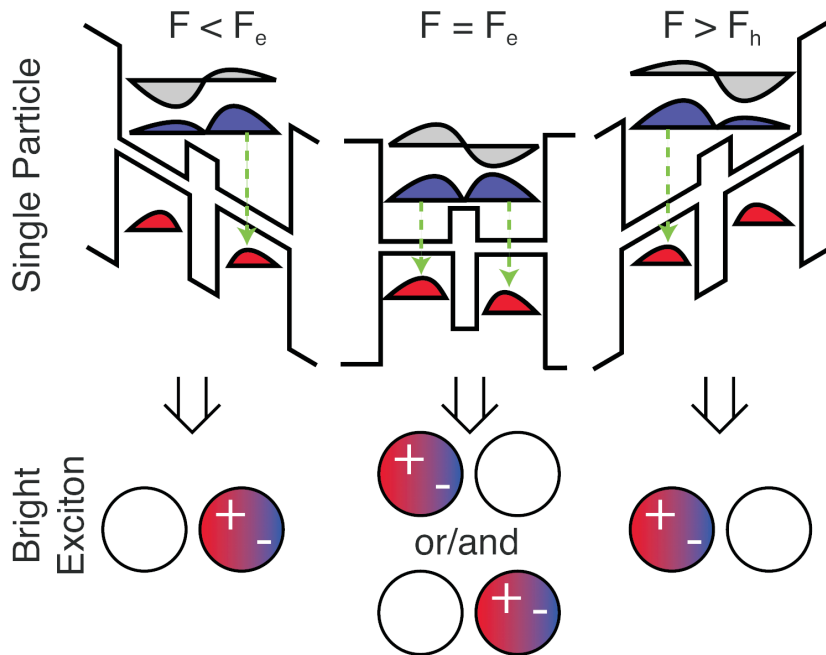


Figure 7.6: Visualization of the nonresonant PL emission scheme. Single particle hole wavefunctions are localized at one dot in the molecule. Electron wavefunctions have significantly higher probability amplitudes at potential minima and they are delocalized over the whole structure when the external electric field (F) aligns electron energy levels in both dots ($F=F_e$). In a kinetic model electrons relax into the QDM first and assume their position of minimal energy through tunneling, whereas holes enter the structure second and stick to the dot into which they relaxed. As exciton formation follows the thermalization of the hot single charge carriers a photon can only be emitted from the dot that contains an electron, as indicated on the figure for the three bias regimes. Reproduced after Ref. [181]

7.4 Rabi oscillations of a single exciton transition in a QDM

Differential reflection spectroscopy compares the spectra of a probe pulse reflected while the system is in the ground state to reflection spectra taken from an excited system. A detailed description of the experimental method is given in chapter 3. It was previously applied to lateral GaAs interface fluctuation QDMs [95] using a scanning near-field microscope. We carried out ultrafast coherent spectroscopy of a single QDM using a double modulation scheme [156,174]. Orthogonal linearly polarized pump- and probe pulses are obtained from a mode-locked Ti:sapphire laser having a pulse duration of about 150 fs. The pulses undergo spectral pulse shaping and subsequent amplitude modulation by acousto-optic modulators. The pump pulse train can be delayed by a time Δt versus

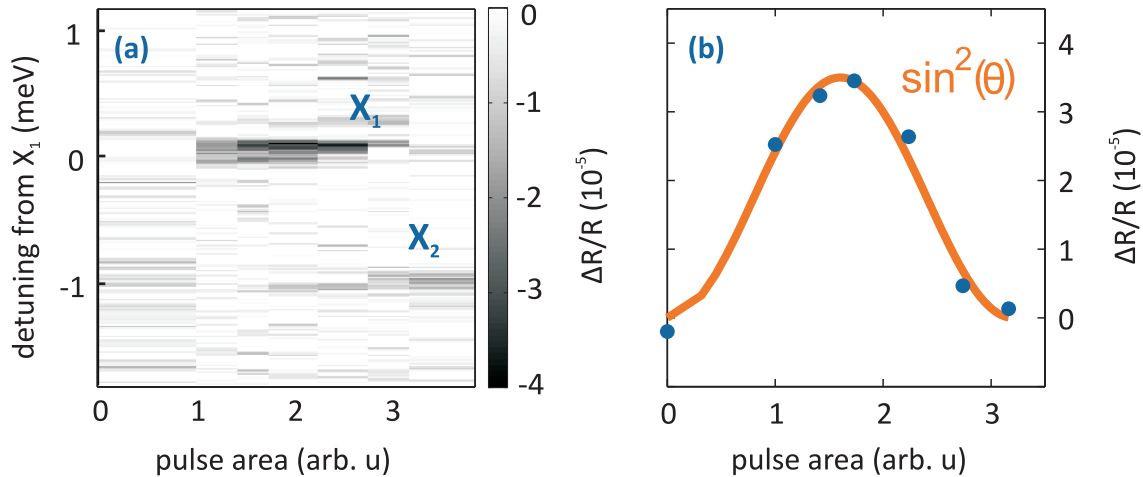


Figure 7.7: a: Raw data of $\Delta R/R$ spectra for a powerseries taken with a bias voltage of -1.2 V (mainly X_1 emits). b: The integral bleaching signal shows a \sin^2 dependence on pulse area.

the probe pulses by means of a mechanical stage. Differential reflectivity spectra $\Delta R/R$ are taken by recording an alternating series of signal and reference spectra at a rate of 1 kHz. For signal spectra $R(\omega, \Delta t)$ both pump and probe beams are gated on whereas for reference spectra $R_0(\omega)$ only the probe beam is gated on. The difference of signal and reference spectra yields consequently the pump-induced spectral response of the quantum dot, $\Delta R(\omega) = R(\omega, \Delta t) - R_0(\omega)$ [92, 109]. The ground state of an optical transition can be depopulated by pump pulses which leads to a bleaching signal in the differential spectrum [96]. The absorption of the pumped transition is then directly proportional to the amplitude of the spectral bleaching feature. Another origin for differential signals lies in the coupled nature of the QDM. We can no longer perceive the structure as two single dots but as one quantum system. The excitation of an exciton in one dot leads therefore to a renormalization of energy levels for the entire QDM so that the single exciton transition in the other dot vanishes and biexcitonic transitions appear instead in the excited system. In other words, whenever the QDM absorbs a photon on any transition leading to an excited state, all absorption lines of the empty QDM change and we can see a differential signal at the respective resonance energies.

A classical effect in coherent spectroscopy is Rabi oscillations [90, 182, 183]. Experiments on single GaAs dots as well as a theoretical description within the framework of the optical Bloch equations were presented in chapter 4. A quantum mechanical two-level system interacts with resonant optical pulses shorter than its decoherence time. The system is driven coherently back and forth between the ground state and the excited state during the interaction time with the pulse. We can write for the population w of the upper state

$$w(\theta) = \sin^2(\theta) = \sin^2\left(\int_{-\infty}^{\infty} \mathbf{E}(t)\boldsymbol{\mu}/\hbar dt\right) \quad , \quad (7.1)$$

where θ is the pulse area, $\mathbf{E}(t)$ is the envelope of the electric field and $\boldsymbol{\mu}$ is the dipole moment of the transition. This means that we can expect a \sin^2 -shaped dependence of differential reflection signal $\Delta R/R$ on the electric field strength. The latter is proportional to the square root of the average pump power.

The pump and probe pulses were shaped so that they are resonant with both exciton transitions X_1 and X_2 (5 meV broad, 150 W/cm² probe intensity on average). We chose zero delay for all measurements so that we are only sensitive to absorption and can ignore all relaxation processes. The bias voltage was set to -1.2 V so that only the exciton with the higher transition energy (X_1) emits in PL. Figure 7.7a shows a power series as a spectral map. Every vertical cut corresponds to a $\Delta R/R$ spectrum at a certain pump power. The integral pump-induced bleaching signal for every pump power is plotted on Fig. 7.7(b). The experimental data fits very well to the theory for a simple two-level system as discussed above. We find a transition dipole moment $|\boldsymbol{\mu}|$ of about 30 Debye. On the spectral map one can see that the second transition (X_2) is starting to be driven only at elevated pump powers. This is in contrast to the kinetic model of the photoluminescence which predicts absorption into both exciton transitions.

7.5 Comparison of emission and transient absorption spectra

To investigate this finding in more detail, we now turn to the bias-dependence of the QDM absorption. From the Rabi oscillations we can infer that an average pump intensity of about 300 W/cm² corresponds to a π -pulse, i.e., completely inverts an exciton transition. This situation gives the maximal pump-probe signal as can be seen on Fig. 7.7. Therefore we adjust both pump and probe pulses to π -pulses for the following experiment.

Figure 7.8a shows bias voltage-dependent PL spectra. We see that for positive bias voltages only X_2 emits, whereas X_1 becomes brightly emitting for negative bias. The alignment case is realized around the zero bias. The corresponding bias region was investigated for the same QDM by transient reflection. $\Delta R/R$ spectra are displayed as a spectral map on Fig. 7.8(b). We can clearly see that the absorption by the QDM behaves basically like the PL emission. The lower energy exciton absorbs for positive bias voltage and the high energy exciton absorbs in the negative bias domain. Again, this is in contrast to the kinetic model which predicts two bias-independent absorption lines.

We also find several differences between the two datasets. We do not observe at any bias voltage the absorption into both excitons simultaneously. The main difference, however,

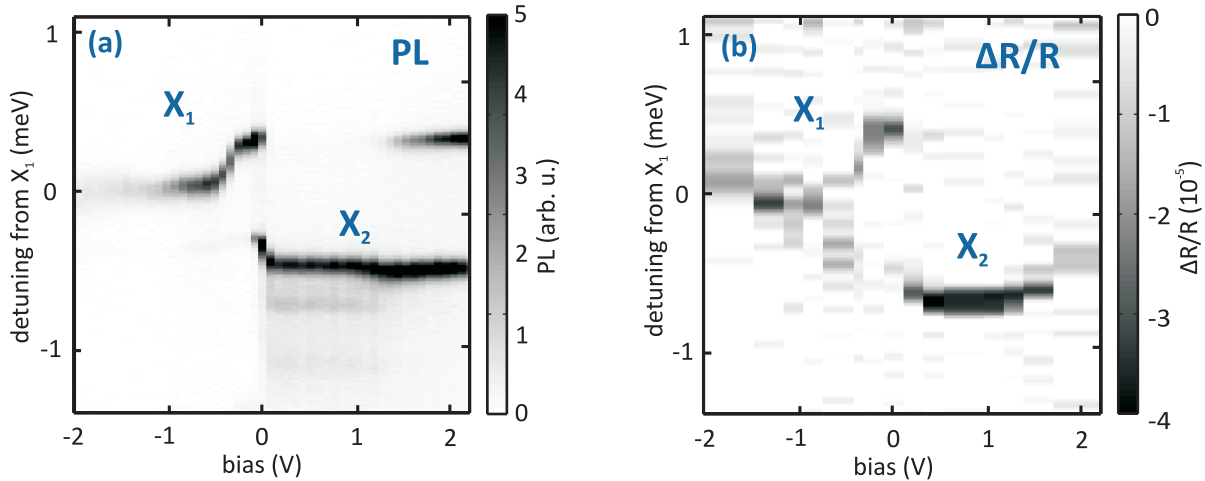


Figure 7.8: a: PL spectral map of QDM emission as a function of the external bias voltage. The PL emission shifts from one exciton to the other when crossing the alignment bias. b: Differential reflection spectra of the same QDM in the corresponding voltage region. The general trend is that also the bleaching signal (absorption) switches from one dot to the other in accordance with the PL emission.

is the prominent reappearance of X_1 in PL emission for bias voltages higher than 1 V which is absolutely absent in absorption. It coincides with the decreasing absorption of X_2 as seen on Fig. 7.8(b). The origin of these two effects is not understood in this system.

Despite of these differences between the non resonantly excited PL emission and the transient absorption experiment, it is obvious that the absorption follows the PL emission as a function of the bias voltage. This means that the transition dipole moments of both direct exciton transitions in the QDM are affected strongly by the bias. We are able to switch not only the emission but also the absorption of the QDM from one dot to the other.

7.6 Bias dependent photoluminescence

This section will give an overview of bias-dependent PL spectra from single QDMs. We will emphasize features in the QDMs' tuning behavior which are not explained by current models but which were observed frequently on our sample. In general we can state that individual molecules differ quite strongly from one another in their optical properties and in their response to an external electric field. Besides, it becomes quite clear that not only data from transient reflection experiments are disagreeing with current models but also several features of PL spectra cannot be properly explained. After some general considerations and recapitulating predictions from theory we will present various

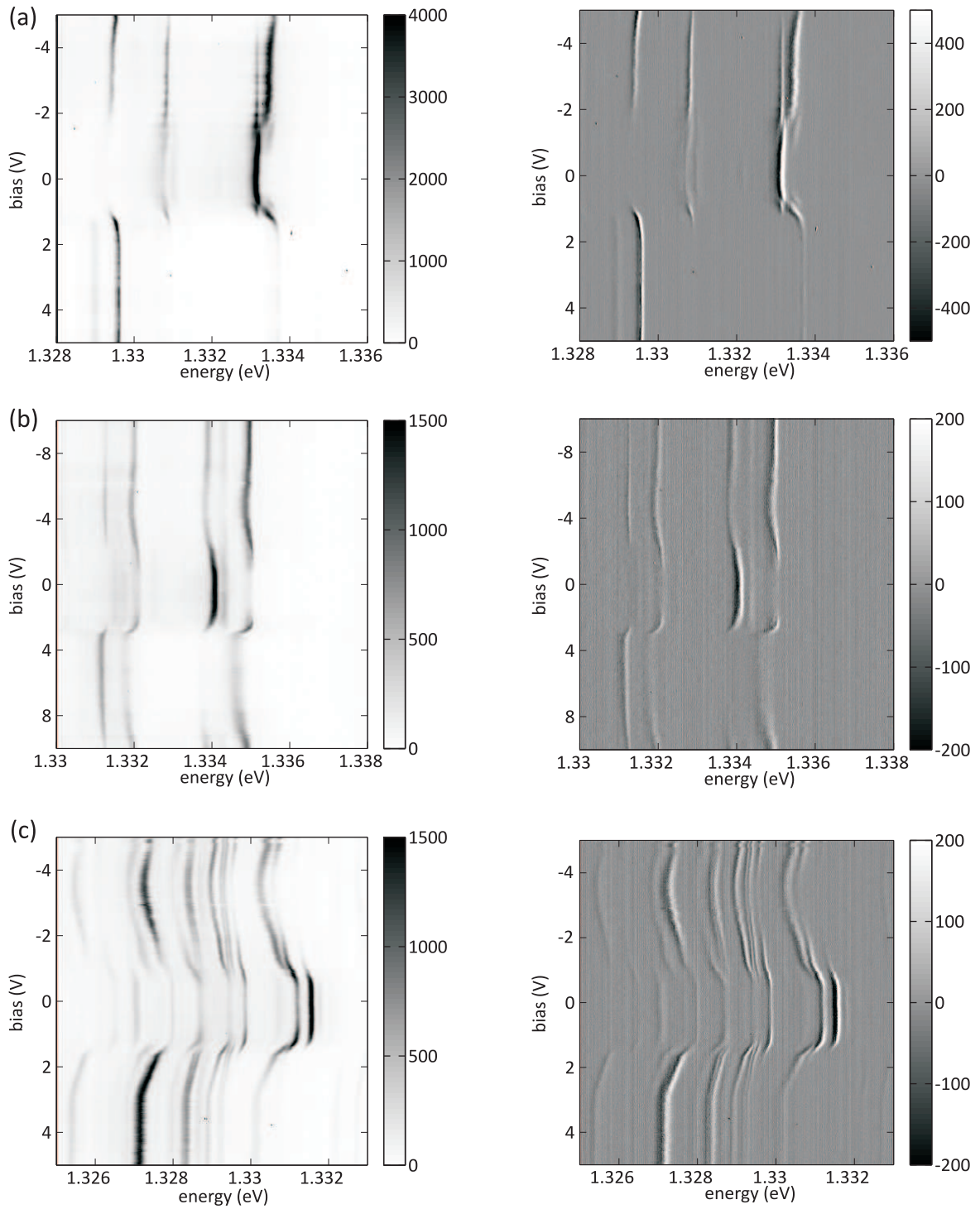


Figure 7.9: Bias-dependent PL emission spectra for three different QDMs (a-c). On the right hand side the derivative of the PL emission with respect to energy is displayed.

bias-dependent PL measurements and discuss prominent and recurring features.

In a QDM the configurations of charge carriers can be more complex than in a single QD. We are not only dealing with neutral excitons (X), trions ($X^{-/+}$) and biexcitons (XX) in one dot, but in two different dots, as the dots composing the QDM are never identical. We also have to consider indirect species, where carriers are distributed over both dots. A neutral exciton can be formed just in one dot ($e_R h_R, e_L h_L$) or it can be an indirect exciton where the electron and the hole are in different dots ($e_L h_R, e_R h_L$). These two cases differ drastically in the context of electric field dependent experiments. First, only the recombination of electrons and holes in the same dot should have a big oscillator strength and only those bright transitions can be resonantly excited. Secondly, only charge configurations with a non-zero permanent in-plane dipole moment show a pronounced shift of their resonance energy as a function of the external electric field. A direct exciton, for example, ideally has almost the same resonance energy independent of the applied field, whereas the resonance energy of an indirect exciton has a strong linear field dependence but only a small oscillator strength (dark state) [181]. Bias-dependent resonance energies and oscillator strengths were calculated from an atomistic model for numerous excitonic species including charged states [184]. Especially in the case of negative trions anticrossings between bright states and dark indirect states were predicted.

Figure 7.9 shows bias-dependent PL emission spectra from three different QDMs. The spectral maps on the left hand side are composed of simple PL spectra, whereas on the right hand side the derivative of the PL emission with respect to photon energy is plotted for enhanced visibility of spectral lines. Especially for narrowly spaced spectral features the differential presentation helps separating different lines. The datasets all show a region around the zero bias in which the PL spectra are very similar and no influence of the electric field is observed. At a voltage of $\pm 1-2$ V the spectra show an abrupt change which is more or less symmetric for both bias directions. Figure 7.9c is the most highly symmetric example both in spectral position as well as in brightness of spectral features while (a) is not at all symmetric in the emission strength of the visible transition lines. Figure 7.9b is resembling very closely the QDM that was investigated in the previous sections of this chapter. It also exhibits a strong asymmetric kink of the lines around the bias where the emission switches from one line to the other (around 2 V here). Switching of the emission from one line to another can be explained by tunneling processes as was presented in the previous sections. The abrupt shift of the resonance energy of all spectral lines, however, can not be explained by tunneling due to external fields. This effect can be seen on Fig. 7.9(b) at around 1 V and on (c) at around 3 V. This collective shifting of all transition energies might be due to filling of charged trap states in the vicinity of the QDM at the respective bias voltage. Another surprising observation can be made in the data displayed on Fig.7.9(c) where the resonance position of relatively bright transitions have a strong dependence on the external field. This effect was evident in a group of QDMs in clear contrast to the predominant case where QDMs have bright lines that do not change their resonance position linearly with the

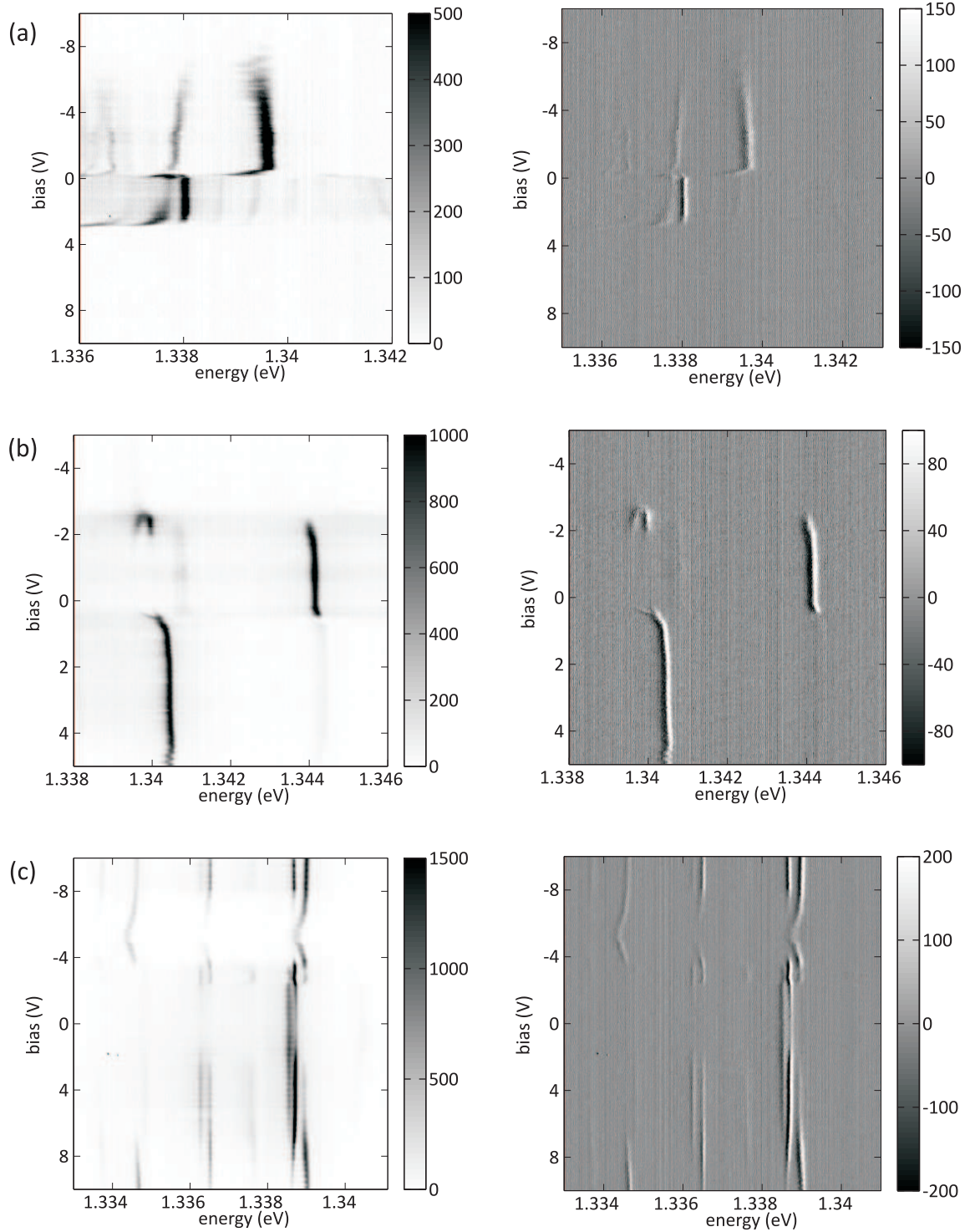


Figure 7.10: Bias-dependent PL emission spectra for three different QDMs (a-c). On the right hand side the derivative of the PL emission with respect to energy is displayed.

bias voltage but stay generally at one position until they switch. This behavior implies that the excited state prior to radiative recombination has a nonzero permanent dipole moment in the sample plane. The only states that satisfy this condition are indirect excitonic species where the electron and the hole which recombine are from two different dots.

The tuning behavior of three more QDMs is displayed on Fig. 7.10. Pronounced switching of the strongest lines is clearly visible. Although these examples lack the obvious symmetry of the cases presented on Fig. 7.9, there are some features which the datasets have in common. A sharp, sudden kink of spectral features around the zero bias is very pronounced in (a) and (b) and all bright transitions show only a minor bias dependence in resonance position. We find again one example of relatively bright transitions that still show a huge spectral shift as a function of the external electric field (c). This example is, however, not as pronounced as in Fig 7.9c. The last three examples do not fit as a whole into a pattern which was regularly observed in our measurements but some isolated features can still be found in most of the QDMs that were studied.

The six presented tuning maps of single QDMs showcase that despite of certain similarities and a group of QDMs that showed uniform behavior in bias-dependent PL emission the sample contains very diverse quantum systems. In order to draw more generalized conclusions and working towards QDM-based devices more uniform samples and much better statistics are necessary. Atomistic modeling can already explain some effects and features, such as field dependent switching of PL emission, but the whole bias tuning behavior of QDMs is not yet satisfactorily described. Especially the frequently observed symmetric tuning case, strongly emitting, apparently indirect excitonic species as well as pronounced kinks of transition lines are not accounted for in current models. Close collaboration between groups involved in sample growth, optical characterization and theoretical modeling is vital to future progress on this system.

In conclusion we applied transient differential reflection spectroscopy to a single lateral InGaAs QDM. We recorded Rabi oscillations driven on a direct exciton transition in the power domain. Our measurements showed that the transition dipole moments in the QDM are strongly influenced by electric fields along the molecular axis. The QDM can basically be treated as a single dot when the bias voltage is adjusted so that one direct exciton transition dominates the absorption spectrum. Furthermore, we compared the QDM's PL emission and its absorption as a function of the external electric field. Despite some differing details these two profoundly dissimilar techniques resulted in well comparable bias-dependent spectra which follow the same trend. The absorption as well as the PL are switched from one direct exciton transition to the other when passing the alignment bias. This finding is direct evidence for field-dependent switching of the transition dipole moments in the QDM. This interpretation is in full agreement with the Rabi oscillations.

Generally, transient absorption spectroscopy is a valuable technique for the characteri-

zation of structures beyond PL measurements. Its time resolution is only limited by the duration of the employed optical pulses. It also does not depend on the emission of a photon or the relaxation of population to a lower level in order to produce a signal. Our technique provides spectroscopic information on all absorbing transitions in the structure. We expect this method to find application in the spectroscopy of non-emitting transitions and in the determination of dipole moments via Rabi oscillations.

8 Conclusion

Semiconductor quantum dots (QDs) are attractive candidates for numerous applications in the field of quantum information processing and for studying light-matter interaction on ultrafast timescales. In the latter case, solid-state single quantum systems are particularly well suited as model-dipoles due to their robust nature. They do not suffer from bleaching or blinking and are very long-lived. In a QD confinement in all three spatial dimensions leads to discrete electron and hole states. Bound electron hole pairs (excitons) can be excited in a QD under resonant optical irradiation. Structures of high crystalline quality and purity can be grown in a molecular beam epitaxy (MBE) chamber under ultra high vacuum (UHV) conditions. QDs fabricated in this way have appealing optical properties such as narrow and bright transition lines.

In this study strain-free GaAs QDs between two AlGaAs barrier layers were investigated. Our samples were grown by *Lijuan Wang* and *Paola Atkinson* in the group of *Oliver G. Schmidt* (MPI FKF Stuttgart and IFW Dresden). In a first step, nanoholes are created on a GaAs layer by removing partially overgrown sacrificial InGaAs QDs in an AsBr₃-etching step. The nanoholes are transferred to the upper surface of the lower AlGaAs barrier during its epitaxial growth. The resulting holes in the AlGaAs barrier is now filled with GaAs leading to the formation of inverted, lens-shaped GaAs QDs. Due to their asymmetric and elongated shape the two groundstate bright exciton transitions have orthogonal linear optical selection rules and their transition energy differs by the fine-structure splitting (FSS). This also means, that the excitonic dipoles are oriented along the [110] and [1 $\bar{1}$ 0] crystal axes and are therefore fixed in space. Polarization-resolved photoluminescence (PL) emission spectroscopy of single dots at temperatures around 10 K yield FSS energies between 50 and 150 μeV .

For the coherent spectroscopy of single QDs a far-field transient differential reflectivity technique was developed. Pump and probe pulses are derived by pulse-shaping from a Ti:Sapphire femtosecond laser. Pump pulses prepare an excited state in the QD which can be read out by delayed probe pulses. The differential signal can be described as the spectral interferogram from the backscattered wave from the QD and the probe light which is reflected at the sample surface. The phase difference between these two waves determines the spectral shape of the differential signal. For dots buried 130 nm beneath the sample surface we detect a dispersively shaped spectral feature at the exciton resonance position. The differential signal is always the difference between probe spectra without a pump pulse and those with active pump pulse. In this way they are a measure

for pump-induced changes in the system. A double-modulated measurement scheme allows for the shot-noise limited detection of differential signals as low as $2 \cdot 10^{-6}$ for an integration time of 10 minutes. With signal strengths of about $4 \cdot 10^{-5}$ a signal-to-noise ratio (SNR) of 17 was reached. Perturbed-free induction decay data from a single exciton could be described by a density matrix model involving the crystal groundstate and the two fine-structure split groundstate exciton states. The data fits well to a model system with a population relaxation time of 230 ps and a coherence time of 90 ps.

A classical example for coherent effects in light-matter interaction are Rabi-oscillations. Here, a resonant optical field drives coherent population oscillations between a groundstate and an excited state. In this way arbitrary population inversions can be prepared in the QD by adjusting the power of a short laser pulse. We carefully adjusted the polarization axes of pump and probe pulses, so that they each only interact with one of the two orthogonal exciton transition dipoles in the QD. The pump pulse drives Rabi-oscillations on one of the two exciton transitions and the probe pulses read out the population inversion in the system via a bleaching signal on the second orthogonal transition due to the pump-induced depopulation of the common crystal groundstate. In this way we exploit the level structure in this quantum mechanical V-system for our measurements. When the pump fully populates one excited state the probe can not create a coherent polarization on the orthogonal transition to the other excited exciton state anymore and a differential signal can be measured. Using this mode of measurement we recorded Rabi-oscillations on several dots and for delay times ranging from 50 to 200 ps. From the period of our Rabi-oscillations we can determine the transition dipole moments of the neutral exciton transition. We determine values of around 18 D, which corresponds to an oscillator strength of around 6 for our GaAs dots.

It turns out that the first period of the population oscillations is still described very well by a simple two-level system. The second period, however, appears to be stretched out with increasing pump power. We explain this observation by the influence of delocalized carriers which are excited only 10 nm underneath the QDs in the GaAs substrate. The density of these delocalized carriers can be determined relative to its saturation value from a spectrally broad background contribution to the differential reflectivity signal. Our experimental data for the Rabi-oscillations can be reproduced by a model in which the effective Rabi frequency at a certain pump power is reduced by a factor which is proportional to the density of the free carriers in the substrate. Saturation powers were realistic for GaAs and the high-power limit of the Rabi frequency reduction amounts to 70%. This means that due to the presence of free carriers in the vicinity of the QD the efficiency of the light-matter coupling is drastically reduced. The microscopic mechanism for this surprising observation was investigated in a following experiment where the substrate is selectively pumped. The influence of the electron-hole gas in the underlying substrate on the absorption spectrum of a single QD was studied in a true two-color pump probe experiment.

The unique structure of our QD samples, in which the lower barrier has a thickness

of only 10 nm, results in a strong interaction between free carriers in the substrate and localized states in the QD. When photocarriers are excited at a semiconductor interface, such as the one between the substrate and the lower barrier, diffusive currents cause a spatial carrier distribution with differing centers of charge for electrons and holes. This so-called photo-Dember effect is well known in semiconductor physics and has been studied extensively in the context of THz emission under pulsed optical excitation. Holes stay near the interface while electrons are reflected from the interface and move rapidly into the substrate due their higher mobility. This charge separation is the origin of a vertical electric field at the location of the QD sitting 10 nm on top of the free carrier cloud. The QD is very sensitive to a variation of the external electric field via the quantum-confined Stark-effect. The potential drop along the confinement direction leads to a lowering of the exciton resonance energy and to a reduced oscillator strength due to decreased overlap of the electron and hole wavefunctions. We successfully exploited this mechanism to demonstrate ultrafast switching of the neutral exciton transition in a single GaAs QD via light-induced DC electric fields.

Both the redshift and the reduction in oscillator strength were calculated as a function of vertical electric field strength by *Ranber Singh* and *Gabriel Bester* (MPI FKF Stuttgart) using an atomistic pseudopotential technique considering realistic structural data, obtained experimentally from nominally similar dots. We study experimentally in detail the influence of hot carriers in the vicinity of single QDs in dependence of the pump power and the pump-probe time delay. Our spectral data can be described in every detail when we include line broadening by spectral diffusion to our model. Fluctuations in the electric environment as small as 1.5 kV/cm are amplified by the Dember-field and cause increasingly broadened lineshapes for highly excited substrates. The strength of the Dember-field is proportional to the density of the photocarriers in the substrate and can be modeled according to the background contribution to our differential spectra. We only have to adjust the Dember-field strength per carrier density and the fluctuation in the intrinsic vertical electric field to our data in order to fit our model. Power-dependent measurements indicate that the Dember-field saturates with the carrier density so that field strengths up to 28 kV/cm are obtained. Delay series show directly the ultrafast switching of the transition line with rise times of below 1 ps and recovery times of around 50 ps which are given by the decay time of excited photocarriers in the GaAs substrate. The reduction of the exciton's oscillator strength is a minor effect of up to 6% within the vertical field regime accessible in our measurements. The main effect is rather the redshift which can be as large as 160 μeV and which is thus much larger than the natural linewidth of our QDs.

We also demonstrated the preparation of entangled coherent superpositions of exciton states in a single QD. As there is no direct dipole transition between the two exciton states, the mutual coherence between both excitons is referred to as Raman-coherence. Here, we excite the QD at an angle of 45° with respect to the bright excitons' dipole axes and read out the system after a variable delay time with a probe field polarized along the orthogonal direction. This experiment can be understood in terms of quantum mechan-

8 Conclusion

ical superpositions and projections. Due to the FSS both exciton states differ in their transition frequencies which causes quantum beats in the time-evolution of the coherent superposition state. We recorded up to three periods of such quantum beats, where the beating time of 43 ps was in good agreement with the FSS energy of $96 \mu\text{eV}$, which was determined independently by polarization-resolved PL spectra. The cleanest quantum beats were obtained using $\pi/2$ -pulses for pumping and probing the system. In this case and ideal system would yield a degree of entanglement of about 0.14. The beating decays with the Raman coherence time of about 100 ps which yields a pure dephasing time of 150 ps with a population relaxation time of 230 ps. The fully entangled Bell state would require higher populations in the exciton states. An attempt for exciting the system with the pump power that would ideally give a degree of entanglement of 0.73 resulted in rather noisy spectra. The pure dephasing time was also drastically reduced to 66 ps for this dataset. This indicates, that at higher pump powers the environment of the QD is causing additional dephasing which means that our QDs are not sufficiently isolated systems. However, quantum beats were still visible, indicating a Raman coherence in the system.

Finally, we also applied our spectroscopic technique to lateral quantum dot molecules (QDMs). DC electric fields are applied along the molecular axis in order to tune PL emission from the QDM from one dot to the other. According to calculations performed in the group of *Gabriel Bester* from the *MPI FKF Stuttgart* both dots should absorb light on their exciton transitions, even when one of the dots does not emit anymore. Our measurements, however, show the same switching behavior both in PL emission as well as in absorption. We have to note that we only investigated a single molecule and that we lack proper statistics to make general statements. The sample was also very heterogeneous and for most QDMs that were investigated the tuning-behavior was absolutely not understood. Therefore, bias-dependent absorption by lateral QDMs has to be studied in greater detail on more uniform samples with well-defined structural properties.

9 Outlook

In the light of the results presented in this thesis several next steps and new projects are within reach. One of the main goals of this work was the development of a robust method for ultrafast spectroscopy of single quantum systems. The experimental setup as described in chapter 3 was applied successfully to various projects, as described in this thesis. It delivers shot-noise limited transient data and stands ready for the spectroscopy of novel nanostructures. As indicated in chapter 7, one could further exploit the fact that one can investigate non-emitting states in a transient absorption experiment. This is normally done by photoluminescence excitation (PLE) measurements [185] and time-correlated single-photon counting (TCSPC). There, one relies, however, still on the emission of a photon from the exciton groundstate and one can only obtain time-resolved spectral information from emitting states. As an alternative, one could perform transient excited state spectroscopy on semiconductor nanostructures such as single quantum dots and quantum wires [186] in order to gain a deeper understanding of their excitation dynamics.

Instead of studying a single nanostructure in more and more detail, one could also perform coherent experiments on more complex hybrid quantum systems. In addition to time-correlated single photon counting and PL spectroscopy [22], one could envision driving Rabi-oscillations on hybridized modes in QDs coupled to plasmonic nanoantennas. By such measurements one could investigate how the transition dipole moments of the coupled system depend on the coupling strength. This project requires, of course, the precise positioning of nanoantennas with respect to single QDs. The efforts in our research group with GaAs dots near the sample surface and electron-beam lithography positioning of single antennas, however, show promising results [187]. When this technique is fully controllable, one could imagine sample series with varying dot-antenna spacing performing the transition from single isolated systems to a coupled hybrid system. Ultrafast spectroscopy of such a series of samples would give insights into the coherence times and the oscillator strength of hybrid modes from particle plasmons and confined excitons.

Quantum dots are placed into micropillar cavities with high quality factors [154, 188, 189] where strong coupling between the QD exciton and the cavity mode is reached [190]. Plasmonic cavities can not rival micropillars or photonic crystal cavities [191, 192] in Q-factors, but they have extremely small mode volumes as they concentrate optical fields on sub-wavelength scales [193]. In the weak coupling regime the cavity influences the

9 Outlook

radiative decay rate of the dot (Purcell effect), whereas in the strong coupling regime the state of the dot now influences the transmission of the coupled cavity. In plasmonic cavity quantum electrodynamics (cQED) one can envision all-optical switching at low powers and ultrafast modulation of optical pulses through interaction with the dot-cavity system.

With respect to the ultrafast switching of excitons we show, that our mechanism relies on stray fields leaking out from a model plate capacitor at the interface between the GaAs substrate and the AlGaAs barrier which is made up from electrons and holes separated by the photo-Dember effect. These leakage fields become stronger when we make the area of the capacitor plates, which is still given by the diffraction limited laser spot on the sample surface, smaller. For this reason we tried to mill out pillar structures which would effectively reduce the size of the photocarrier cloud underneath the QD [194]. As the radiation damage from the gallium ions which are used in our focused ion beam (FIB) milling machine seems to destroy the QDs in the sample, we will try to use dry etching through a lithographically defined mask [154]. Once this process is developed, one can test the limits of the system in terms of pillar diameter and obtainable Dember-field strengths. One should work in close collaboration with groups in sample growth in order to investigate further optimization of the QD switch. The use of a material with a very fast carrier recombination time, such as low-temperature GaAs as an absorbing layer under the dot, would reduce the recovery time of the switch greatly [153]. Our switching mechanism is also very interesting in the context of cavity QED, as one can tune a QD into resonance with a cavity using ultrafast optical pulses. In this way the system could only be coupled during a very brief interaction time window, enabling a whole new class of quantum optical experiments.

In the field of quantum dot molecules (QDMs) there are still a lot of open questions from the perspective of coherent spectroscopy. As already mentioned in chapter 7, we only showed one single example on a not too well understood sample. One would need better statistics and more homogeneous samples in order to characterize the bias-tuning behavior of these complex lateral double-dot structures in a satisfying way. If such structures are available, systematic transient absorption studies on QDMs can be performed. Instead of only measuring transient absorption spectra for one pump power or one bias voltage one could record a data cube where each slice has one fixed parameter. A data cube with one spectral axis, one pump power axis and one bias voltage axis would, for example, describe how the dipole moments of the various transitions in the QDM change with respect to the bias voltage.

List of acronyms

- 1D** one-dimensional
- 2D** two-dimensional
- 3D** three-dimensional
- AC** alternating current
- ACF** autocorrelation
- AFM** atomic force microscope
- APD** avalanche photo diode
- BBO** beta barium borate
- BS** beam splitter
- CCD** charge coupled device
- cw** continuous wave
- DC** direct current
- EBL** electron beam lithography
- FIB** focused ion beam
- FWHM** full width at half maximum
- FSS** fine structure splitting
- FWM** four-wave mixing
- GVD** group velocity dispersion
- LBO** lithium triborate
- MBE** molecular beam epitaxy

9 Outlook

MOVPE metal-organic vapor phase epitaxy

NA numerical aperture

OPO optical parametric oscillator

PBS polarizing beam splitter

PH pin hole

PID perturbed free induction decay

PL photoluminescence

PLE photoluminescence excitation

PMT photomultiplier tube

PPLN periodically poled lithium niobate

PS pulse shaper

QD quantum dot

QDM quantum dot molecule

QW quantum well

SEM scanning electron microscope

SHG second harmonic generation

SNR signal-to-noise ratio

TCSPC time-correlated single-photon counting

TEM transmission electron microscope

UHV ultra high vacuum

UV ultraviolet

WL wetting layer

List of Figures

2.1	Electronic density of states at low-dimensions.	18
2.2	Epitaxial growth of semiconductor nanostructures.	20
2.3	Growth of GaAs/AlGaAs QDs.	21
2.4	Polarization-resolved PL-spectra from a single GaAs QD.	23
2.5	Power-dependent PL-spectra from a single GaAs QD.	24
2.6	Coupling to nanoantennas with surface-near GaAs QDs.	27
2.7	Positioning of single Au-nanoantennas relative to QDs.	28
2.8	Realization of a <i>CROT</i> -gate in a single QD.	29
3.1	Techniques of coherent QD spectroscopy.	33
3.2	Experimental setup.	35
3.3	Laser system.	36
3.4	Preparation of the pulse sequence.	38
3.5	Chirp in optical pulses.	39
3.6	Optical grating pulse shaper.	40
3.7	Home-built pulse shaper.	41
3.8	Pulse spectrum and duration.	42
3.9	Microscope and detection of light.	44
3.10	Laser-scanning confocal microscope involving a telecentric lens system.	45
3.11	Calibration of the microscope.	46
3.12	Spectral interferometry.	47
3.13	Double modulation scheme.	49
3.14	Differential reflection signals.	50
3.15	Differential spectra of dots near the surface.	51
3.16	Perturbed free-induction decay of a localized exciton.	53
4.1	Rotating frame and lab frame.	63
4.2	Relaxation in a two-level system.	65
4.3	Rabi oscillations in a single GaAs QD.	68
4.4	Background signal from hot carriers in the capping layer.	69
4.5	Additional data on Rabi-oscillations.	70
5.1	Photo-Dember field and quantum-confined Stark-effect.	76
5.2	Vertical polarizability from atomistic pseudopotential calculations.	78
5.3	Broadening due to spectral diffusion.	79
5.4	Refractive index and differential reflectivity for excited GaAs.	81

List of Figures

5.5	Background signal from delocalized carriers in GaAs.	82
5.6	Two-color pump-probe configurations for pumping the substrate.	83
5.7	Representative differential spectra for excited substrate.	84
5.8	Power series at 1.70 eV.	87
5.9	Delay series at 1.70 eV.	89
5.10	Power series at 1.59 eV.	91
5.11	Delay series at 1.59 eV.	92
5.12	SEM image of pillar structures.	93
6.1	Fine-structure splitting in a single GaAs QD.	98
6.2	Differential reflectivity for different polarization angles.	99
6.3	Quantum beats in a single GaAs QD.	100
6.4	Further results on quantum beats.	101
7.1	Growth of lateral InGaAs QDMs.	107
7.2	Lateral InGaAs QDM sample with Au-electrodes.	108
7.3	PL spectrum of QDMs.	109
7.4	Bias-dependent switching of PL emission in QDMs.	110
7.5	Power-dependent PL-spectra of QDMs for different bias regimes.	111
7.6	Kinetic model for PL-switching in QDMs.	113
7.7	Rabi flopping in QDMs.	114
7.8	Bias-dependent switching of the absorption from a single QDM.	116
7.9	Further data on PL-switching in QDMs.	117
7.10	Further examples of PL-switching in QDMs.	119

List of Tables

2.1	Basic parameters of GaAs bandstructure.	17
4.1	Numerical results from Rabi oscillations.	70
5.1	Parameters for Dember-field model.	86
6.1	Numerical results for quantum beats.	102

Bibliography

- [1] A. Gruber, A. Dräbenstedt, C. Tietz, L. Fleury, J. Wrachtrup, and C. von Borczyskowski. Scanning confocal optical microscopy and magnetic resonance on single defect centers. *Science*, 276(5321):2012–2014, 1997.
- [2] C. B. Murray, C. R. Kagan, and M. G. Bawendi. Synthesis and characterization of monodisperse nanocrystals and close-packed nanocrystal assemblies. *Annual Review of Materials Science*, 30(1):545–610, 2000.
- [3] N. F. Johnson. Quantum dots: few-body, low-dimensional systems. *Journal of Physics: Condensed Matter*, 7(6):965, 1995.
- [4] X. Michalet, F. F. Pinaud, L. A. Bentolila, J. M. Tsay, S. Doose, J. J. Li, G. Sundaresan, A. M. Wu, S. S. Gambhir, and S. Weiss. Quantum dots for live cells, in vivo imaging, and diagnostics. *Science*, 307(5709):538–544, 2005.
- [5] Burns, A. and Ow, H. and Wiesner, U. Fluorescent core-shell silica nanoparticles: towards "Lab on a Particle" architectures for nanobiotechnology. *Chem. Soc. Rev.*, 35:1028–1042, 2006.
- [6] D. Loss and D. P. DiVincenzo. Quantum computation with quantum dots. *Phys. Rev. A*, 57:120–126, 1998.
- [7] R. Nötzel. Self-organized growth of quantum-dot structures. *Semiconductor Science and Technology*, 11(10):1365, 1996.
- [8] Y. Nabetani, T. Ishikawa, S. Noda, and A. Sasaki. Initial growth stage and optical properties of a three-dimensional InAs structure on GaAs. *J. Appl. Phys.*, 76(1):347–351, 1994.
- [9] D. Richter and R. Hafenbrak and K. D. Jöns and W.-M. Schulz and M. Eichfelder and M. Heldmaier and R. Roßbach and M. Jetter and P. Michler. Low density MOVPE grown InGaAs QDs exhibiting ultra-narrow single exciton linewidths. *Nanotechnology*, 21(12):125606, 2010.
- [10] P.M. Petroff and S.P. DenBaars. MBE and MOCVD growth and properties of self-

Bibliography

assembling quantum dot arrays in III-V semiconductor structures. *Superlattices and Microstructures*, 15(1):15–21, 1994. .

- [11] D. Birkedal, K. Leosson, and J. M. Hvam. Long lived coherence in self-assembled quantum dots. *Phys. Rev. Lett.*, 87:227401, 2001.
- [12] A. N. Vamivakas, Y. Zhao, S. Fält, A. Badolato, J. M. Taylor, and M. Atatüre. Nanoscale optical electrometer. *Phys. Rev. Lett.*, 107:166802, 2011.
- [13] H. Htoon, D. Kulik, O. Baklenov, A. L. Holmes, T. Takagahara, and C. K. Shih. Carrier relaxation and quantum decoherence of excited states in self-assembled quantum dots. *Phys. Rev. B*, 63:241303, Jun 2001.
- [14] S. A. Empedocles, D. J. Norris, and M. G. Bawendi. Photoluminescence Spectroscopy of Single CdSe Nanocrystallite Quantum Dots. *Phys. Rev. Lett.*, 77:3873–3876, Oct 1996.
- [15] Edward B. Flagg, Andreas Muller, Sergey V. Polyakov, Alex Ling, Alan Migdall, and Glenn S. Solomon. Interference of Single Photons from Two Separate Semiconductor Quantum Dots. *Phys. Rev. Lett.*, 104(13), 2010.
- [16] B. Patton, W. Langbein, U. Woggon, L. Maingault, and H. Mariette. Time- and spectrally-resolved four-wave mixing in single CdTe/ZnTe quantum dots. *Phys. Rev. B*, 73(23):235354, 2006.
- [17] A. N. Vamivakas, C. Y. Lu, C. Matthiesen, Y. Zhao, S. Falt, A. Badolato, and M. Atatuere. Observation of spin-dependent quantum jumps via quantum dot resonance fluorescence. *Nature*, 467(7313):297–300, 2010.
- [18] Antonio Badolato, Kevin Hennessy, Mete Atatüre, Jan Dreiser, Evelyn Hu, Pierre M. Petroff, and Atac Imamoglu. Deterministic Coupling of Single Quantum Dots to Single Nanocavity Modes. *Science*, 308(5725):1158–1161, 2005.
- [19] A. Kiraz, P. Michler, C. Becher, B. Gayral, A. Imamoglu, Lidong Zhang, E. Hu, W. V. Schoenfeld, and P. M. Petroff. Cavity-quantum electrodynamics using a single InAs quantum dot in a microdisk structure. *Appl. Phys. Lett.*, 78(25):3932–3934, 2001.
- [20] A. V. Akimov, A. Mukherjee, C. L. Yu, D. E. Chang, A. S. Zibrov, P. R. Hemmer, H. Park, and M. D. Lukin. Generation of single optical plasmons in metallic nanowires coupled to quantum dots. *Nature*, 450(7168):402–406, 2007.
- [21] Y. Fedutik, V. V. Temnov, O. Schoeps, U. Woggon, and M. V. Artemyev. Exciton-

- plasmon-photon conversion in plasmonic nanostructures. *Phys. Rev. Lett.*, 99(13), 2007.
- [22] Markus Pfeiffer, Klas Lindfors, Christian Wolpert, Paola Atkinson, Mohamed Benyoucef, Armando Rastelli, Oliver G. Schmidt, Harald Giessen, and Markus Lippitz. Enhancing the Optical Excitation Efficiency of a Single Self-Assembled Quantum Dot with a Plasmonic Nanoantenna. *Nano Lett.*, 10(11):4555–4558, 2010.
- [23] Alberto G. Curto, Giorgio Volpe, Tim H. Taminiau, Mark P. Kreuzer, Romain Quidant, and Niek F. van Hulst. Unidirectional Emission of a Quantum Dot Coupled to a Nanoantenna. *Science*, 329(5994):930–933, 2010.
- [24] A Gonzalez-Tudela, D Martin-Cano, E Moreno, L. Martin-Moreno, C. Tejedor, and F. J. Garcia-Vidal. Entanglement of two qubits mediated by one-dimensional plasmonic waveguides. *Phys. Rev. Lett.*, 106:020501, 2011.
- [25] D. Chang and A. Sorensen and E. Demler and M. Lukin. A single-photon transistor using nanoscale surface plasmons. *Nat. Physics*, 03(11):807–812, 2007.
- [26] H. Haken and H. C. Wolf. *Atom- und Quantenphysik*. Springer, 2004.
- [27] H. Haken and H. C. Wolf. *Molekülphysik und Quantenchemie*. Springer, 1998.
- [28] B.H. Brandsden and C. J. Joachain. *Physics of Atoms and Molecules*. Longman, 1996.
- [29] H. Ibach and H. Lüth. *Solid-State Physics, 4th edition*. Springer, 2009.
- [30] C. Kittel. *Introduction to Solid State Physics, 8th edition*.
- [31] U. Woggon. *Optical Properties of Semiconductor Quantum Dots*. Springer, 1997.
- [32] S. Hunklinger. *Festkörperphysik, 2nd edition*. Oldenbourg, 2009.
- [33] M. Bayer. *Exciton Complexes in Self-Assembled In(Ga)As/GaAs Quantum dots, in: Single Quantum Dots - Fundamentals, applications and New Concepts (Ed.: P. Michler), Nanoscience and Technology, Vol. 90, Chap. 3*. Springer, 2003.
- [34] W. G. Bryant and G. S. Solomon. *Optics of Quantum Dots and Wires*. Artech House, Inc., 2005.
- [35] Y. Yin and A.P. Alivisatos. Colloidal nanocrystal synthesis and the organic-inorganic interface. *Nature*, 437(7059):664–670, 2005.

Bibliography

- [36] M. Kuno, D.P. Fromm, H.F. Hamann, A. Gallagher, and D.J. Nesbitt. “On”/”off” fluorescence intermittency of single semiconductor quantum dots. *J. Chem. Phys.*, 115(2):1028–1040, 2001.
- [37] Benoit Mahler, Piernicola Spinicelli, Stephanie Buil, Xavier Quelin, Jean-Pierre Hermier, and Benoit Dubertret. Towards non-blinking colloidal quantum dots. *Nature Mat.*, 7(8):659–664, 2008.
- [38] W. J. Parak, T. Pellegrino, and C. Plank. Labelling of cells with quantum dots. *Nanotechnology*, 16(2):R9, 2005.
- [39] X. Gao, W. C. W. Chan, and S. Nie. Quantum-dot nanocrystals for ultrasensitive biological labeling and multicolor optical encoding. *Journal of Biomedical Optics*, 7(4):532–537, 2002.
- [40] D. Richter, R. Roßbach, W.-M. Schulz, E. Koroknay, C. Kessler, M. Jetter, and P. Michler. Low-density InP quantum dots embedded in Ga_{0.51}In_{0.49}P with high optical quality realized by a strain inducing layer. *Applied Physics Letters*, 97(6):063107, 2010.
- [41] A. Rastelli et al. *Growth and Control of Optically Active Quantum Dots*, in: *Single Semiconductor Quantum Dots* (Ed.: P. Michler), Chap. 2. Springer, 2009.
- [42] H. Schweizer et al. *Quantum-Dot Lasers*, in: *Single Quantum Dots - Fundamentals, applications and New Concepts* (Ed.: P. Michler), *Nanoscience and Technology, Vol. 90, Chap. 5*. Springer, 2003.
- [43] A. Rastelli, S. Stuffer, A. Schliwa, R. Songmuang, C. Manzano, G. Costantini, K. Kern, A. Zrenner, D. Bimberg, and O. G. Schmidt. Hierarchical Self-Assembly of GaAs/AlGaAs Quantum Dots. *Phys. Rev. Lett.*, 92(16):166104, 2004.
- [44] L. Wang. Growth and spectroscopic characterization of self-assembled lateral quantum dot molecules. *PhD thesis*, 2009.
- [45] P. Harrison. *Quantum Wells, Wires and Dots*. Wiley, 2009.
- [46] H. Giessen. Ultrafast carrier and gain dynamics in strongly confined semiconductor quantum dots. *PhD thesis*, 1995.
- [47] P. Michler. *Quantum Dot Single-Photon Sources*, in: *Single Semiconductor Quantum Dots* (Ed.: P. Michler), Chap. 6. Springer, 2009.
- [48] M. Bayer, G. Ortner, O. Stern, A. Kuther, A. A. Gorbunov, A. Forchel, P. Hawrylak, S. Fafard, K. Hinzer, T. L. Reinecke, S. N. Walck, J. P. Reithmaier, F. Klopff,

- and F. Schäfer. Fine structure of neutral and charged excitons in self-assembled In(Ga)As/(Al)GaAs quantum dots. *Phys. Rev. B*, 65:195315, 2002.
- [49] J. D. Plumhof, V. Křápek, L. Wang, A. Schliwa, D. Bimberg, A. Rastelli, and O. G. Schmidt. Experimental investigation and modeling of the fine structure splitting of neutral excitons in strain-free $GaAs/Al_xGa_{1-x}As$ quantum dots. *Phys. Rev. B*, 81(12):121309, 2010.
- [50] Lijuan Wang, Vlastimil Křápek, Fei Ding, Felicity Horton, Andrei Schliwa, Dieter Bimberg, Armando Rastelli, and Oliver G. Schmidt. Self-assembled quantum dots with tunable thickness of the wetting layer: Role of vertical confinement on interlevel spacing. *Phys. Rev. B*, 80(8):085309, 2009.
- [51] Qiang Wu, Robert D. Grober, D. Gammon, and D. S. Katzer. Excitons, biexcitons, and electron-hole plasma in a narrow 2.8-nm GaAs/ $Al_xGa_{1-x}As$ quantum well. *Phys. Rev. B*, 62:13022–13027, 2000.
- [52] P. Borri, W. Langbein, S. Schneider, U. Woggon, R. L. Sellin, D. Ouyang, and D. Bimberg. Ultralong dephasing time in ingaas quantum dots. *Phys. Rev. Lett.*, 87:157401, 2001.
- [53] J. Guest, T. Stievater, X. Li, J. Cheng, D. Steel, D. Gammon, D. Katzer, D. Park, C. Ell, A. Thranhardt, and H. Khitrova, G. and Gibbs. Measurement of optical absorption by a single quantum dot exciton. *Phys. Rev. B*, 65(24), 2002.
- [54] D. Bimberg. Quantum dot based nanophotonics and nanoelectronics. *Electron. Lett.*, 44(3):168–170, 2008.
- [55] Hideaki Saito, Kenichi Nishi, Ichiro Ogura, Shigeo Sugou, and Yoshimasa Sugimoto. Room-temperature lasing operation of a quantum-dot vertical-cavity surface-emitting laser. *Appl. Phys. Lett.*, 69(21):3140–3142, 1996.
- [56] Y. Arakawa and H. Sakaki. Multidimensional quantum well laser and temperature dependence of its threshold current. *Applied Physics Letters*, 40(11):939–941, 1982.
- [57] E. U. Rafailov, M. A. Cataluna, and W. Sibbett. Mode-locked quantum-dot lasers. *Nat. Photonics*, 1(7):395–401, 2007.
- [58] P. Borri, W. Langbein, J.M. Hvam, F. Heinrichsdorff, M.-H. Mao, and D. Bimberg. Ultrafast gain dynamics in inas-ingaas quantum-dot amplifiers. *Photonics Technology Letters, IEEE*, 12(6):594–596, 2000.
- [59] W.J. Parak, D. Gerion, T. Pellegrino, D. Zanchet, C. Micheel, S. C. Williams,

Bibliography

- R. Boudreau, M. A. Le Gros, C. A. Larabell, and P. Alivisatos. Biological applications of colloidal nanocrystals. *Nanotechnology*, 14(7):R15, 2003.
- [60] P. Michler, A. Kiraz, C. Becher, W. Schoenfeld, P. Petroff, L. Zhang, E. Hu, and A. Imamoglu. A quantum dot single-photon turnstile device. *Science*, 290(5500):2282, 2000.
- [61] Z. Yuan, B. E. Kardynal, R. M. Stevenson, A. J. Shields, C. J. Lobo, K. Cooper, Neil S. B., D. A. Ritchie, and M. Pepper. Electrically driven single-photon source. *Science*, 295(5552):pp. 102–105, 2002.
- [62] R. Stevenson, R. Young, P. Atkinson, K. Cooper, D. Ritchie, and A. Shields. A semiconductor source of triggered entangled photon pairs. *Nature*, 439(7073):179–182, 2006.
- [63] P. Michler, A. Imamoglu, M.D. Mason, P.J. Carson, G.F. Strouse, and S.K. Buratto. Quantum correlation among photons from a single quantum dot at room temperature. *Nature*, 406(6799):968–970, 2000.
- [64] L. Novotny and B. Hecht. *Principles of Nano-Optics*. Cambridge University Press, 2006.
- [65] K.J. Vahala. Optical microcavities. *Nature*, 424(6950):839–846, 2003.
- [66] S. Schietinger, M. Barth, T. Aichele, and O. Benson. Plasmon-enhanced single photon emission from a nanoassembled metal-diamond hybrid structure at room temperature. *Nano Letters*, 9(4):1694–1698, 2009. PMID: 19301860.
- [67] A. Bek, R. Jansen, M. Ringler, S. Mayilo, T. A. Klar, and J. Feldmann. Fluorescence enhancement in hot spots of afm-designed gold nanoparticle sandwiches. *Nano Letters*, 8(2):485–490, 2008. PMID: 18173294.
- [68] M. Ringler, A. Schwemer, M. Wunderlich, A. Nichtl, K. Kürzinger, T. A. Klar, and J. Feldmann. Shaping emission spectra of fluorescent molecules with single plasmonic nanoresonators. *Phys. Rev. Lett.*, 100:203002, 2008.
- [69] F. Tam, G. P. Goodrich, B. R. Johnson, and N. J. Halas. Plasmonic enhancement of molecular fluorescence. *Nano Lett.*, 7(2):496–501, 2007.
- [70] H. Mertens and A. Polman. Plasmon-enhanced erbium luminescence. *Applied Physics Letters*, 89(21):211107, 2006.
- [71] K. T. Shimizu, W. K. Woo, B. R. Fisher, H. J. Eisler, and M. G. Bawendi.

- Surface-enhanced emission from single semiconductor nanocrystals. *Phys. Rev. Lett.*, 89:117401, 2002.
- [72] Z. Kinkhabwala, A. and Yu, S. Fan, Y. Avlasevich, K. Muellen, and W. E. Moerner. Large single-molecule fluorescence enhancements produced by a bowtie nanoantenna. *Nat. Photonics*, 3(11):654–657, 2009.
- [73] E.M. Purcell. Spontaneous emission probabilities at radio frequencies. *Phys. Rev.*, 69(11-1):681, 1946.
- [74] K.H. Drexage, H. Kuhn, and F.P. Schafer. Variation of fluorescence decay time of a molecule in front of a mirror. *Berichte Der Bunsen-Gesellschaft für physikalische Chemie*, 72(2):329–&, 1968.
- [75] N. Liu, L. Langguth, T. Weiss, J. Kaestel, M. Fleischhauer, T. Pfau, and H. Giessen. Plasmonic analogue of electromagnetically induced transparency at the Drude damping limit. *Nature Mat.*, 8(9):758–762, 2009.
- [76] P. Anger, P. Bharadwaj, and L. Novotny. Enhancement and quenching of single-molecule fluorescence. *Phys. Rev. Lett.*, 96:113002, 2006.
- [77] E. Zallo and P. Atkinson and A. Rastelli and O. G. Schmidt. Controlling the formation of quantum dot pairs using nanohole templates. *Journal of Crystal Growth*, 338(1):232 – 238, 2012.
- [78] C. H. Bennett and D. P. DiVincenzo. Quantum information and computation. *Nature*, 404(6775):247–255, 2000.
- [79] Y. Nakamura, Y.A. Pashkin, and J.S. Tsai. Coherent control of macroscopic quantum states in a single-Cooper-pair box. *Nature*, 398(6730):786–788, 1999.
- [80] Chiorescu, I. and Nakamura, Y. and Harmans, C. and Mooij, J.E. Coherent quantum dynamics of a superconducting flux qubit. *Science*, 299(5614):1869–1871, 2003.
- [81] J. Ahn, T.C. Weinacht, and P.H. Bucksbaum. Information storage and retrieval through quantum phase. *Science*, 287(5452):463–465, 2000.
- [82] A. Imamoglu, D.D. Awschalom, G. Burkard, D.P. DiVincenzo, D. Loss, M. Sherwin, and A. Small. Quantum information processing using quantum dot spins and cavity QED. *Phys. Rev. Lett.*, 83(20):4204–4207, 1999.
- [83] T. Hayashi, T. Fujisawa, H. D. Cheong, Y. H. Jeong, and Y. Hirayama. Coherent

Bibliography

- manipulation of electronic states in a double quantum dot. *Phys. Rev. Lett.*, 91:226804, 2003.
- [84] H. J. Krenner, S. Stuffer, M. Sabathil, E. C. Clark, P. Ester, M. Bichler, G. Abstreiter, J. J. Finley, and A. Zrenner. Recent advances in exciton-based quantum information processing in quantum dot nanostructures. *New J. Phys.*, 7:184, 2005.
- [85] H. J. Krenner, E. C. Clark, T. Nakaoka, M. Bichler, C. Scheurer, G. Abstreiter, and J. J. Finley. Optically probing spin and charge interactions in a tunable artificial molecule. *Phys. Rev. Lett.*, 97(7), 2006.
- [86] X. Q. Li, Y. W. Wu, D. Steel, D. Gammon, T. H. Stievater, D. S. Katzer, D. Park, C. Piermarocchi, and L. J. Sham. An all-optical quantum gate in a semiconductor quantum dot. *Science*, 301(5634):809–811, 2003.
- [87] Y. W. Wu, X. Q. Li, L. M. Duan, D. G. Steel, and D. Gammon. Density matrix tomography through sequential coherent optical rotations of an exciton qubit in a single quantum dot. *Phys. Rev. Lett.*, 96(8):087402, 2006.
- [88] J.C. Diels and W. Rudolph. *Ultrashort laser pulse phenomena: fundamentals, techniques, and applications on a femtosecond time scale*. Optics and photonics. Academic Press, 2006.
- [89] Q. Q. Wang, A. Muller, P. Bianucci, C. K. Shih, M. T. Cheng, H. J. Zhou, and J. B. Han. Internal and external polarization memory loss in single semiconductor quantum dots. *Appl. Phys. Lett.*, 89(14), 2006.
- [90] A. Zrenner, E. Beham, S. Stuffer, F. Findeis, M. Bichler, and G. Abstreiter. Coherent properties of a two-level system based on a quantum-dot photodiode. *Nature*, 418(6898):612–614, 2002.
- [91] S Stuffer, P Ester, A Zrenner, and M Bichler. Quantum optical properties of a single InxGa1-xAs-GaAs quantum dot two-level system. *Phys. Rev. B*, 72(12), 2005.
- [92] T. Guenther, C. Lienau, T. Elsaesser, M. Glanemann, V. Axt, T. Kuhn, S. Eshlaghi, and A. Wieck. Coherent nonlinear optical response of single quantum dots studied by ultrafast near-field spectroscopy. *Phys. Rev. Lett.*, 89(5), 2002.
- [93] T. Unold, K. Mueller, C. Lienau, T. Elsaesser, and A. D. Wieck. Optical stark effect in a quantum dot: Ultrafast control of single exciton polarizations. *Phys. Rev. Lett.*, 92(15):157401, 2004.
- [94] Thomas Unold, Kerstin Mueller, Christoph Lienau, and Thomas Elsaesser. Space

- and time resolved coherent optical spectroscopy of single quantum dots. *Semiconductor Science and Technology*, 19(4):S260, 2004.
- [95] T. Unold, K. Mueller, C. Lienau, T. Elsaesser, and A. D. Wieck. Optical control of excitons in a pair of quantum dots coupled by the dipole-dipole interaction. *Phys. Rev. Lett.*, 94(13):137404, 2005.
- [96] Florian Sotier, Tim Thomay, Tobias Hanke, Jan Korger, Suddhasatta Mahapatra, Alexander Frey, Karl Brunner, Rudolf Bratschitsch, and Alfred Leitenstorfer. Femtosecond few-fermion dynamics and deterministic single-photon gain in a quantum dot. *Nat. Physics*, 5(5):352–356, 2009.
- [97] M Zecherle, C Ruppert, E Clark, G Abstreiter, J Finley, and M Betz. Ultrafast few-fermion optoelectronics in a single self-assembled ingaas/gaas quantum dot. *Phys. Rev. B*, 82(12):125314, 2010.
- [98] M. Wesseli, C. Ruppert, S. Trumm, H. J. Krenner, J. J. Finley, and M. Betz. Nonlinear optical response of a single self-assembled InGaAs quantum dot: A femtojoule pump-probe experiment. *Appl. Phys. Lett.*, 88(20):203110, 2006.
- [99] C. Hermannstädter, M. Witzany, G. J. Beirne, W.-M. Schulz, M. Eichfelder, R. Rossbach, M. Jetter, P. Michler, L. Wang, A. Rastelli, and O. G. Schmidt. Polarization fine structure and enhanced single-photon emission of self-assembled lateral InGaAs quantum dot molecules embedded in a planar microcavity. *J. Appl. Phys.*, 105(12):122408, 2009.
- [100] G. J. Beirne, C. Hermannstädter, L. Wang, A. Rastelli, O. G. Schmidt, and P. Michler. Quantum light emission of two lateral tunnel-coupled (In,Ga)As/GaAs quantum dots controlled by a tunable static electric field. *Phys. Rev. Lett.*, 96(13):137401, 2006.
- [101] I. Jovanovic, J. Schmidt, and C. Ebbers. Optical parametric chirped-pulse amplification in periodically poled KTiOPO4 at 1053 nm. *Appl. Phys. Lett.*, 83(20):4125–4127, 2003.
- [102] G. Cerullo and S. De Silvestri. Ultrafast optical parametric amplifiers. *Rev. Sc. Instrum.*, 74(1, Part 1):1–18, 2003.
- [103] T. Brixner and G. Gerber. Femtosecond polarization pulse shaping. *Opt. Lett.*, 26(8):557–559, 2001.
- [104] Mateusz Plewicki, Fabian Weise, Stefan M. Weber, and Albrecht Lindinger. Phase, amplitude, and polarization shaping with a pulse shaper in a mach-zehnder interferometer. *Appl. Opt.*, 45(32):8354–8359, 2006.

Bibliography

- [105] K. C. Chu, J. P. Heritage, R. S. Grant, and W. E. White. Temporal interferometric measurement of femtosecond spectral phase. *Opt. Lett.*, 21(22):1842–1844, 1996.
- [106] F. Träger. *Springer handbook of lasers and optics*. Springer, 2007.
- [107] M. Bohmer, F. Pampaloni, M. Wahl, H.-J. Rahn, R. Erdmann, and J. Enderlein. Time-resolved confocal scanning device for ultrasensitive fluorescence detection. *Review of Scientific Instruments*, 72(11):4145–4152, 2001.
- [108] J. D. Jackson. *Classical Electrodynamics*. Wiley, 2nd edition, 1975.
- [109] Karrai, K. and Warburton, R. J. Optical transmission and reflection spectroscopy of single quantum dots. *Superlattices Microstruct.*, 33(5-6):311–337, 2003.
- [110] T. Plakhotnik and V. Palm. Interferometric signatures of single molecules. *Phys. Rev. Lett.*, 87(18), 2001.
- [111] B. Alén, F. Bickel, K. Karrai, R.J. Warburton, and P.M. Petroff. Stark-shift modulation absorption spectroscopy of single quantum dots. *Appl. Phys. Lett.*, 83(11):2235–2237, 2003.
- [112] J. Oudar, D. Hulin, A. Migus, A. Antonetti, and F. Alexandre. Subpicosecond spectral hole burning due to non-thermalized photoexcited carriers in GaAs. *Phys. Rev. Lett.*, 55(19):2074–2077, 1985.
- [113] Shin Kim, Eunsoon Oh, J. U. Lee, and D. S. Kim. Time-resolved differential reflection measurements on $\text{Ga}_{1-x}\text{Mn}_x\text{As}$. *J. of the Korean Phys. Soc.*, 49(4):1611–1614, 2006.
- [114] B. Fluegel, N. Peyghambarian, G. Olbright, M. Lindberg, S. W. Koch, M. Joffre, D. Hulin, A. Migus, and A. Antonetti. Femtosecond Studies Of Coherent Transients In Semiconductors. *Phys. Rev. Lett.*, 59(22):2588–2591, 1987.
- [115] M. Joffre, D. Hulin, A. Migus, A. Antonetti, C. B. A. Laguillaume, N. Peyghambarian, M. Lindberg, and S. W. Koch. Coherent Effects In Pump Probe Spectroscopy Of Excitons. *Opt. Lett.*, 13(4):276–278, 1988.
- [116] X. Hu, D. Du, G. Cheng, J. Zou, and X. Li. Switching from positive to negative dispersion in a three-level V system driven by a single coherent field. *J. Phys. B-At. Mol. Opt. Phys.*, 38(7):827–838, 2005.
- [117] Z. Ficek and S. Swain. Simulating quantum interference in a three-level system with perpendicular transition dipole moments. *Phys. Rev. A*, 69(2):023401, 2004.

- [118] P. Michler. *Single Semiconductor Quantum Dots*. Nanoscience and Technology. Springer, 2009.
- [119] AJ Ramsay. A review of the coherent optical control of the exciton and spin states of semiconductor quantum dots. *Semiconductor Science and Technology*, 25:103001, 2010.
- [120] H. Htoon, T. Takagahara, D. Kulik, O. Baklenov, A. L. Holmes, and C. K. Shih. Interplay of rabi oscillations and quantum interference in semiconductor quantum dots. *Phys. Rev. Lett.*, 88:087401, 2002.
- [121] B. Patton, U. Woggon, and W. Langbein. Coherent control and polarization readout of individual excitonic states. *Phys. Rev. Lett.*, 95(26):266401, 2005.
- [122] L. Allen and J.H. Eberly. *Optical resonance and two-level atoms*. Dover books on physics and chemistry. Dover, 1987.
- [123] P.W. Milonni and J.H. Eberly. *Lasers*. Wiley Series in Pure and Applied Optics. Wiley, 1988.
- [124] H. Kuzmany. *Solid-state spectroscopy: an introduction*. Springer Verlag, 1998.
- [125] T. Unold, K. Mueller, C. Lienau, T. Elsaesser, and A. Wieck. Optical control of excitons in a pair of quantum dots coupled by the dipole-dipole interaction. *Phys. Rev. Lett.*, 94(13), 2005.
- [126] Hany S. Loka and Seldon D. Benjamin and Peter W. E. Smith. Refractive index and absorption changes in low-temperature-grown GaAs. *Opt. Comm.*, 155(1-3):206 – 212, 1998. .
- [127] R. Warburton, C. Durr, K. Karrai, J. Kotthaus, G. Medeiros-Ribeiro, and P. Petroff. Charged excitons in self-assembled semiconductor quantum dots. *Phys. Rev. Lett.*, 79(26):5282–5285, 1997.
- [128] Alfred Leitenstorfer, Cornelius Fürst, Alfred Laubereau, Wolfgang Kaiser, Günther Tränkle, and Günter Weimann. Femtosecond Carrier Dynamics in GaAs Far from Equilibrium. *Phys. Rev. Lett.*, 76:1545–1548, 1996.
- [129] K. Henneberger, W. Schäfer, and F. Jahnke. Optical and transport nonlinearities in laser excited semiconductors. *Phys. Scr.*, 1991(T35):129, 1991.
- [130] J. L. Oudar, I. Abram, A. Migus, D. Hulin, and J. Etchepare. Transient anisotropy effects in the absorption saturation of GaAs. *J. of Luminescence*, 30(1-4):340 – 354, 1985.

Bibliography

- [131] S. Hunsche, H. Heesel, A. Ewertz, H. Kurz, and J. H. Collet. Spectral-hole burning and carrier thermalization in GaAs at room temperature. *Phys. Rev. B*, 48:17818–17826, 1993.
- [132] J. H. Collet, S. Hunsche, H. Heesel, and H. Kurz. Influence of electron-hole correlations on the absorption of gaas in the presence of nonthermalized carriers. *Phys. Rev. B*, 50:10649–10655, 1994.
- [133] H. Dember. Über eine photoelektronische Kraft in Kupferoxydul-Kristallen. *Physikalische Zeitschrift*, 32:554, 1931.
- [134] H. Dember. Über die Vorwärtsbewegung von Elektronen durch Licht. *Physikalische Zeitschrift*, 33:207, 1931.
- [135] T. Dekorsy, H. Auer, H. Bakker, H. Roskos, and H. Kurz. THz electromagnetic emission by coherent infrared-active phonons. *Phys. Rev. B*, 53(7):4005–4014, 1996.
- [136] T. Dekorsy, H. Kurz, X. Zhou, and K. Ploog. Investigation of Field, Carrier, and Coherent Phonon Dynamics in Low-Temperature-Grown GaAs. *Appl. Phys. Lett.*, 63(21):2899–2901, 1993.
- [137] J.N. Heyman, N. Coates, A. Reinhardt, and G. Strasser. Diffusion and drift in terahertz emission at GaAs surfaces. *Appl. Phys. Lett.*, 83(26):5476–5478, 2003.
- [138] W. Kütt, G.C. Cho, M. Strahnen, and H. Kurz. Electro-optic sampling of surface space-charge fields on III–V compounds. *Appl. Surf. Sci.*, 50(1–4):325 – 329, 1991.
- [139] R. Kersting, K. Unterrainer, G. Strasser, H. F. Kauffmann, and E. Gornik. Few-Cycle THz Emission from Cold Plasma Oscillations. *Phys. Rev. Lett.*, 79:3038–3041, Oct 1997.
- [140] S. Sanguinetti, M. Gurioli, E. Grilli, M. Guzzi, and M. Henini. Piezoelectric-induced quantum-confined Stark effect in self-assembled InAs quantum dots grown on (N11) GaAs substrates. *Applied Physics Letters*, 77(13):1982–1984, 2000.
- [141] M. Gurioli, S. Sanguinetti, and M. Henini. Dynamic quantum-confined Stark effect in self-assembled InAs quantum dots. *Applied Physics Letters*, 78(7):931–933, 2001.
- [142] T. Dekorsy, T. Pfeifer, W. Kutt, and H. Kurz. Subpicosecond Carrier Transport in GaAs Surface-Space-Charge Fields. *Phys. Rev. B*, 47(7):3842–3849, 1993.
- [143] D. A. B. Miller, D. S. Chemla, T. C. Damen, A. C. Gossard, W. Wiegmann, T. H.

- Wood, and C. A. Burrus. Band-edge electroabsorption in quantum well structures: The quantum-confined stark effect. *Phys. Rev. Lett.*, 53:2173–2176, 1984.
- [144] S. A. Empedocles and M. G. Bawendi. Quantum-Confined Stark Effect in Single CdSe Nanocrystallite Quantum Dots. *Science*, 278(5346):pp. 2114–2117, 1997.
- [145] R. J. Warburton, C. Schulhauser, D. Haft, C. Schäfflein, K. Karrai, J. M. Garcia, W. Schoenfeld, and P. M. Petroff. Giant permanent dipole moments of excitons in semiconductor nanostructures. *Phys. Rev. B*, 65:113303, Feb 2002.
- [146] J. Houel, A. V. Kuhlmann, L. Greuter, F. Xue, M. Poggio, B. D. Gerardot, P. A. Dalgarno, A. Badolato, P. M. Petroff, A. Ludwig, D. Reuter, A. D. Wieck, and R. J. Warburton. Probing Single-Charge Fluctuations at a GaAs/AlAs Interface Using Laser Spectroscopy on a Nearby InGaAs Quantum Dot. *Phys. Rev. Lett.*, 108:107401, 2012.
- [147] Gabriel Bester. Electronic excitations in nanostructures: an empirical pseudopotential based approach. *Journal of Physics: Condensed Matter*, 21(2):023202, 2009.
- [148] M. Abbarchi, F. Troiani, C. Mastrandrea, G. Goldoni, T. Kuroda, T. Mano, K. Sakoda, N. Koguchi, S. Sanguinetti, A. Vinattieri, and M. Gurioli. Spectral diffusion and line broadening in single self-assembled GaAs/AlGaAs quantum dot photoluminescence. *Applied Physics Letters*, 93(16):162101, 2008.
- [149] A. Leitenstorfer, R. Huber, F. Tauser, and A. Brodschelm. How fast do charged particles get dressed? *phys. stat. sol. (b)*, 238(3):455–461, 2003.
- [150] R. Huber, F. Tauser, A. Brodschelm, and A. Leitenstorfer. Femtosecond Buildup of a Many-Body Resonance Observed via Two-Dimensional THz Time-Domain Spectroscopy. *phys. stat. sol. (b)*, 234(1):207–214, 2002.
- [151] M. D. Sturge. Optical absorption of gallium arsenide between 0.6 and 2.75 ev. *Phys. Rev.*, 127:768–773, 1962.
- [152] M. Born and E. Wolf. *Principles of optics, 6th edition*. Cambridge University Press, 1997.
- [153] Gupta, S. and Frankel, M. and Valdmanis, J. and Whittaker, J. and Mourou, G. and Smith, F. and Calawa, A. Subpicosecond carrier lifetime in GaAs grown by molecular-beam epitaxy at low temperatures. *Appl. Phys. Lett.*, 59(25):3276–3278, 1991.
- [154] M. Benyoucef, S. M. Ulrich, P. Michler, J. Wiersig, F. Jahnke, and A. Forchel.

Bibliography

- Enhanced correlated photon pair emission from a pillar microcavity. *New Journal of Physics*, 6(1):91, 2004.
- [155] A.S. Lenihan, M.V. Gurudev Dutt, D.G. Steel, S. Ghosh, and P.K. Bhattacharya. Raman coherence beats from entangled polarization eigenstates in InAs quantum dots. *Phys. Rev. Lett.*, 88(22), 2002.
- [156] C Wolpert, C Dicken, L Wang, P Atkinson, A Rastelli, O. G. Schmidt, H Giessen, and M Lippitz. Ultrafast coherent spectroscopy of a single self-assembled quantum dot. *phys. stat. sol. (b)*, 249(4):721–730, 2012.
- [157] K.B. Ferrio and D.G. Steel. Raman quantum beats of interacting excitons. *Phys. Rev. Lett.*, 80(4):786–789, 1998.
- [158] I. Ya. Gerlovin, I. V. Ignatiev, I. A. Yugova, and Y. Masumoto. Quantum beats of fine-structure states in InP quantum dots. *Opt. Spectrosc.*, 104(4):577–587, 2008.
- [159] T. Flissikowski, A. Hundt, M. Lowisch, M. Rabe, and F. Henneberger. Photon beats from a single semiconductor quantum dot. *Phys. Rev. Lett.*, 86(14):3172–3175, 2001.
- [160] X. Li, Y. Wu, D. Steel, D. Gammon, and L. Sham. Raman coherence beats from the entangled state involving polarized excitons in single quantum dots. *Phys. Rev. B*, 70(19), 2004.
- [161] I.A. Yugova, I.Y. Gerlovin, V.G. Davydov, I.V. Ignatiev, I.E. Kozin, H.W. Ren, M. Sugisaki, S. Sugou, and Y. Masumoto. Fine structure and spin quantum beats in InP quantum dots in a magnetic field. *Phys. Rev. B*, 66(23), 2002.
- [162] I.E. Kozin, V.G. Davydov, I.V. Ignatiev, A.V. Kavokin, K.V. Kavokin, G. Malpuech, H.W. Ren, M. Sugisaki, S. Sugou, and Y. Masumoto. Zero-field spin quantum beats in charged quantum dots. *Phys. Rev. B*, 65(24), 2002.
- [163] J. Stolze and D. Suter. *Quantum Computing: A Short Course from Theory to Experiment*. Wiley-VCH, 2004.
- [164] C. Bennett, D. DiVincenzo, J. Smolin, and WK Wootters. Mixed-state entanglement and quantum error correction. *Phys. Rev. A*, 54(5):3824–3851, 1996.
- [165] R. Hafenbrak, S. M. Ulrich, P. Michler, L. Wang, A. Rastelli, and O. G. Schmidt. Triggered polarization-entangled photon pairs from a single quantum dot up to 30K. *New J. Phys.*, 9(315), 2007.
- [166] M. Bayer, P. Hawrylak, K. Hinzer, S. Fafard, M. Korkusinski, Z. R. Wasilewski,

- O. Stern, and A. Forchel. Coupling and entangling of quantum states in quantum dot molecules. *Science*, 291(5503):451–453, 2001.
- [167] H. J. Krenner, M. Sabathil, E. C. Clark, A. Kress, D. Schuh, M. Bichler, G. Abstreiter, and J. J. Finley. Direct observation of controlled coupling in an individual quantum dot molecule. *Phys. Rev. Lett.*, 94:057402, 2005.
- [168] M. Scheibner, I. V. Ponomarev, E. A. Stinaff, M. F. Doty, A. S. Bracker, C. S. Hellberg, T. L. Reinecke, and D. Gammon. Photoluminescence Spectroscopy of the Molecular Biexciton in Vertically Stacked InAs-GaAs Quantum Dot Pairs. *Phys. Rev. Lett.*, 99:197402, 2007.
- [169] M. Scheibner, M. Yakes, A. S. Bracker, I. V. Ponomarev, M. F. Doty, C. S. Hellberg, L. J. Whitman, T. L. Reinecke, and D. Gammon. Optically mapping the electronic structure of coupled quantum dots. *Nat. Phys.*, 4(4):291–295, 2008.
- [170] L. Wang, A. Rastelli, S. Kiravittaya, P. Atkinson, F. Ding, C. C. Bof. Bufon, C. Hermannstädter, M. Witzany, G. J. Beirne, P. Michler, and O. G. Schmidt. Towards deterministically controlled InGaAs/GaAs lateral quantum dot molecules. *New J. of Physics*, 10(4):045010, 2008.
- [171] C. Hermannstaedter, G. J. Beirne, M. Witzany, M. Heldmaier, J. Peng, G. Bester, L. Wang, A. Rastelli, O. G. Schmidt, and P. Michler. Influence of the charge carrier tunneling processes on the recombination dynamics in single lateral quantum dot molecules. *Phys. Rev. B*, 82(8), 2010.
- [172] Abram L. Falk, Frank H. L. Koppens, Chun L. Yu, Kibum Kang, Nathalie de Leon Snapp, Alexey V. Akimov, Moon-Ho Jo, Mikhail D. Lukin, and Hongkun Park. Near-field electrical detection of optical plasmons and single-plasmon sources. *Nat. Physics*, 5(7):475–479, 2009.
- [173] P. Borri, W. Langbein, U. Woggon, M. Schwab, M. Bayer, S. Fafard, Z. Wasilewski, and P. Hawrylak. Exciton dephasing in quantum dot molecules. *Phys. Rev. Lett.*, 91:267401, 2003.
- [174] C Wolpert, C Dicken, L Wang, P Atkinson, A Rastelli, O. G. Schmidt, H Giessen, and M Lippitz. Transient reflection: A versatile technique for ultrafast spectroscopy of a single quantum dot in complex environments. *Nano Lett.*, 12(1):453–457, 2012.
- [175] C Wolpert, L Wang, A Rastelli, O. G. Schmidt, H Giessen, and M Lippitz. Transient absorption spectroscopy of a single lateral InGaAs quantum dot molecule. *phys. stat. sol. (b)*, 249(4):731–736, 2012.

Bibliography

- [176] R. Songmuang, S. Kiravittaya, and O.G. Schmidt. Formation of lateral quantum dot molecules around self-assembled nanoholes. *Appl. Phys. Lett.*, 82(17):2892–2894, 2003.
- [177] Fei Ding, Lijuan Wang, Suwit Kiravittaya, Elisabeth Mueller, Armando Rastelli, and Oliver G. Schmidt. Unveiling the morphology of buried In(Ga)As nanostructures by selective wet chemical etching: From quantum dots to quantum rings. *Appl. Phys. Lett.*, 90(17), 2007.
- [178] C Hermannstaedter. Optical properties of single charge-tunable and laterally coupled (In, Ga)As/GaAs quantum dots. *PhD thesis*, 2010.
- [179] R. Strobel, R. Eccleston, J. Kuhl, and K. Köhler. Measurement of the exciton-formation time and the electron- and hole-tunneling times in a double-quantum-well structure. *Phys. Rev. B*, 43:12564–12570, 1991.
- [180] T. C. Damen, Jagdeep Shah, D. Y. Oberli, D. S. Chemla, J. E. Cunningham, and J. M. Kuo. Dynamics of exciton formation and relaxation in GaAs quantum wells. *Phys. Rev. B*, 42:7434–7438, 1990.
- [181] J. Peng, C. Hermannstaedter, M. Witzany, M. Heldmaier, L. Wang, S. Kiravittaya, A. Rastelli, O. G. Schmidt, P. Michler, and G. Bester. Heterogeneous confinement in laterally coupled InGaAs/GaAs quantum dot molecules under lateral electric fields. *Phys. Rev. B*, 81(20), 2010.
- [182] T. H. Stievater, X. Q. Li, D. G. Steel, D. Gammon, D. S. Katzer, D. Park, C. Piermarocchi, and L. J. Sham. Rabi oscillations of excitons in single quantum dots. *Phys. Rev. Lett.*, 8713(13):133603, 2001.
- [183] H. Kamada, H. Gotoh, J. Temmyo, T. Takagahara, and H. Ando. Exciton rabi oscillation in a single quantum dot. *Phys. Rev. Lett.*, 8724(24):246401, 2001.
- [184] Jie Peng and Gabriel Bester. Charged excitons and biexcitons in laterally coupled (In,Ga)As quantum dots. *Phys. Rev. B*, 82(23), 2010.
- [185] M. Heldmaier, M. Seible, C. Hermannstädter, M. Witzany, R. Roßbach, M. Jetter, P. Michler, L. Wang, A. Rastelli, and O. G. Schmidt. Excited-state spectroscopy of single lateral self-assembled ingaas quantum dot molecules. *Phys. Rev. B*, 85:115304, 2012.
- [186] T. Lutz, T. Kabakchiev, A. and Dufaux, C. Wolpert, Z. Wang, K. Burghard, M. and Kuhnke, and K. Kern. Scanning Tunneling Luminescence of Individual CdSe Nanowires. *Small*, 7(16):2396–2400, 2011.

- [187] M. Pfeiffer, K. Lindfors, P. Atkinson, A. Rastelli, O. G. Schmidt, Harald G., and Markus L. Positioning plasmonic nanostructures on single quantum emitters. *phys. stat. sol. (b)*, 249(4):678–686, 2012.
- [188] Pelton, M. and Santori, C. and Vuckovic, J. and Zhang, B. and Solomon, G. S. and Plant, J. and Yamamoto, Y. Efficient source of single photons: A single quantum dot in a micropost microcavity. *Phys. Rev. Lett.*, 89:233602, 2002.
- [189] A. Dousse, L. Lanco, J. Suffczynski, E. Semenova, A. Miard, A. Lemaitre, I. Sagnes, C. Roblin, J. Bloch, and P. Senellart. Controlled Light-Matter Coupling for a Single Quantum Dot Embedded in a Pillar Microcavity Using Far-Field Optical Lithography. *Phys. Rev. Lett.*, 101(26), 2008.
- [190] J.P. Reithmaier, G. Sek, A. Löffler, C. Hofmann, S. Kuhn, S. Reitzenstein, L.V. Keldysh, T.L. Kulakovskii, V.D. and Reinecke, and A. Forchel. Strong coupling in a single quantum dot-semiconductor microcavity system. *Nature*, 432(7014):197–200, 2004.
- [191] D. Englund, A. Faraon, I. Fushman, N. Stoltz, P. Petroff, and J. Vuckovic. Controlling cavity reflectivity with a single quantum dot. *Nature*, 450(7171):857–861, 2007.
- [192] Englund, D. and Majumdar, A. and Bajcsy, M. and Faraon, A. and Petroff, P. and Vuckovic, J. Ultrafast photon-photon interaction in a strongly coupled quantum dot-cavity system. *Phys. Rev. Lett.*, 108:093604, 2012.
- [193] D. E. Chang, A. S. Sørensen, P. R. Hemmer, and M. D. Lukin. Strong coupling of single emitters to surface plasmons. *Phys. Rev. B*, 76:035420, 2007.
- [194] R. Bratschitsch and A. Leitenstorfer. Ultrafast semiconductor quantum optics. 2010.

Lebenslauf

Persönliche Daten:

Nachname	Wolpert
Vorname	Christian
Geburtsdatum/-ort	05.10.1981 / Würzburg
Familienstand	ledig
Adresse	Heisenbergstr. 9, 70569 Stuttgart
Telefon	0176-61269044
E-Mail	c.wolpert@fkf.mpg.de, DWolpertC@gmx.de

Schulbildung:

09/1988 - 07/1992	Volksschule Oberdürrbach und Eisingen (bei Würzburg)
09/1992 - 05/2001	Deutschhaus Gymnasium Würzburg
05/2001	Abschluss: Abitur (Durchschnittsnote:1,6)

Wehrdienst:

09/2001 - 05/2002	St. Kp. Panzer Brigade 36
-------------------	---------------------------

Studium:

10/2002 - 07/2005	Studium der Physik an der Julius Maximilians Universität Würzburg, Nebenfächer: Chemie, Astronomie
10/2004	Vordiplom in Physik, Note: sehr gut (Durchschnittsnote: 1,4)
08/2005 - 05/2007	Studium der Physik an der University of New Mexico at Albuquerque, USA
05/2007	Master of Science in Physik, G.P.A.: 3.85

Promotion:

10/2007 - heute	Promotionsstudium an der Universität Stuttgart und am Max-Planck-Institut für Festkörperforschung, Stuttgart
-----------------	--

Sonstiges:

Sprachen: Englisch, Französisch

Acknowledgments

I would like to conclude by thanking all those who contributed to this thesis and who supported me.

First, I have to thank my advisor Prof. Dr. Markus Lippitz for accepting me as his first doctoral candidate. I deeply appreciate the liberty which I enjoyed working on my project at the Max Planck Institute for Solid State Research. His continuous support with both scientific and practical problems was invaluable.

I thank Prof. Dr. Peter Michler for the interest in my work and for being my co-advisor and Prof. Dr. H. P. Büchler as dissertation committee member.

I would like to express my gratitude as well to Prof. Dr. Harald Giessen for welcoming me to his institute and for his encouragement and motivation.

For our excellent quantum dot samples and a stimulating collaboration I have to thank Lijuan Wang, Paola Atkinson and Armando Rastelli from the group of Oliver G. Schmidt at *IFW Dresden*.

For a successful collaboration and fruitful discussions I want to thank Prof. Dr. Peter Michler, Dr. Michael Jetter, Dr. Claus Hermannstädter and Matthias Heldmaier from the *Institut für Halbleiteroptik und Funktionelle Grenzflächen Stuttgart*, Prof. Dr. Heinz Schweizer from the *4th Physics Institute of the University of Stuttgart*, Ranber Sing and Gabriel Bester from the *MPI FKF Stuttgart*.

During this long time I also enjoyed the great working atmosphere and the stimulating environment here in Stuttgart. This is why I want to thank the entire Junior Research Group *Ultrafast Nanooptics* at the MPI for Solid State Research and the 4th Physics Institute at the University of Stuttgart. In this context, I want to thank especially my office mates Christian Dicken, Thorsten Schumacher, Daniela Ullrich and Matthias Brandstetter, as well as Markus Pfeiffer, Dr. Klas Lindfors, Mario Hentschel, Richard Taubert, Dr. Jessie Chin and Dr. Tobias Utikal for being great colleagues and friends.

Last but not least I want to thank also my friends and my family for their tolerance and their support. My parents and my grandparents encouraged me a great deal during my dissertation, but in particular I owe gratitude to my godmother Eugenie and my brother Daniel.

